This manuscript has been submitted for publication to JOURNAL OF CLIMATE (AMS). Note that this manuscript has undergone three rounds of peer review but has yet to be formally accepted for publication. Subsequent versions may differ slightly in content.


# Efficient Estimation of Climate State and Its Uncertainty Using Kalman Filtering with Application to Policy Thresholds and Volcanism

J. Matthew Nicklas,[a] Baylor Fox-Kemper,[a] Charles Lawrence[a]

[a] *Brown University, Providence, Rhode Island.*

*Corresponding author*: J. Matthew Nicklas, john_nicklas@brown.edu

ABSTRACT: We present the Energy Balance Model – Kalman Filter (EBM-KF), a hybrid model projecting and assimilating the global mean surface temperature (GMST) and ocean heat content anomaly (OHCA). It combines an annual energy balance model (difference equations) with 17 parameters drawn from the literature and a statistical Extended Kalman Filter assimilating GMST and OHCA, either observed timeseries or simulated by earth system models. Our motivation is to create an efficient and natural estimator of the climate state and its uncertainty, which we believe to be Gaussian at a global scale. We illustrate four applications: 1) EBM-KF generates a similar estimate to the 30-year time-averaged climate state 15 years sooner, or a model-simulated hindcasts' annual ensemble average, depending on the preparation of volcanic forcing. 2) EBM-KF conveniently assesses annually likelihoods of crossing a policy threshold. For example, based on temperature records up to the end of 2023, p=0.0017 that the climate state was 1.5°C over preindustrial, but there is a 16% likelihood that the GMST in 2023 itself could have been over that threshold. 3) A variant of the EBM-KF also approximates the spread of an entire climate model large ensemble using only one or a few ensemble members. 4) All variants of the EBM-KF are sufficiently fast to allow thorough sampling from non-Gaussian probabilistic futures, e.g., the impact of rare but significant volcanic eruptions. This sampling with the EBM-KF better determines how future volcanism may affect when policy thresholds will be crossed and what an ensemble with thousands of members exploring future intermittent volcanism reveals.

SIGNIFICANCE STATEMENT: The global average of the Earth's historical climate over the past 150 years can be explained by a thermal/radiation physics equation involving a small number of constants (17), atmospheric $CO_2$ concentration, anthropogenic clouds, and volcanic emissions. Global mean surface temperature measurements vary around this climate state within a consistent normal distribution. This physics equation and statistical depiction allowed us to construct a simple model that can rapidly estimate the uncertainty in Earth's current climate, aid in policy discussions, and provide an alternative for some applications to expensive ensemble modeling.

## 1. Introduction

What is the uncertainty in Earth's climate? From a measurement standpoint, this issue was resolved many decades ago. The instantaneous measurement of global mean surface temperature (GMST) is currently performed with average accuracy of 0.05°C (max 0.10°C) via arrays of infrared-sensing satellites and ground stations (Susskind et al. 2019). Both satellite and ground datasets extend back to 1981 (Merchant et al. 2019), and the yearly seasonal fluctuation is easy to smooth with a running annual average. However, this GMST still has significant dynamical and random stochasticity, from processes like the 2-7 year quasi-periodic El Nino events (Hu and Fedorov 2017) and volcanic eruptions that intermittently affect climate for 1-2 years (Soden et al. 2002). Measurement errors also arise from sparse or inconsistently calibrated historical data and paleoproxies (Carré et al. 2012; Emile-Geay et al. 2017; Kaufman et al. 2020; McClelland et al. 2021). Internal variability dominates over climate-forced variability in most short-term signals, both in climate simulations and reality (Gulev et al. 2021; Kirtman et al. 2013; Lee et al. 2021; Marotzke and Forster 2015). By "simulations", we refer to computationally expensive global coupled models (and occasionally to numerical weather model predictions). Other climate variables reveal warming that is steadier than GMST (less "noisy" annual variability). One such steady climate variable is the Ocean Heat Content Anomaly (OHCA), where >90% of the anthropogenic energy anomaly is found (Cheng et al. 2017, 2022; Fox-Kemper et al. 2021; Gulev et al. 2021). Even radical reductions in global $CO_2$ emissions may not show an identifiable impact on GMST over a time scale of a few years (Szopa et al. 2021), posing a challenge for policy and assessment.

In 1935 the World Meteorological Association began reporting the "standard climate normal" as surface temperature averages over an interval of 30 years ($\overline{_{30}Y_t}$ in this paper's notation). A 30-year window was chosen to minimize most internal fluctuations (such as El Nino) and short-term forcings such as single volcanoes (Guttman 1989); the effect is similar to examining less noisy metrics of the climate system such as the OHCA. Fig. 1 shows this metric and emphasizes the 30-year span over which the average is taken. To generate continuous estimates of the climate, this 30-year average can be updated annually, forming a running mean (Supp. Fig. 4b). While standard climate normals and running means are straightforward and widely accepted definitions of climate, they involve lag: the most current 30-year unweighted average describes the average climate state of Earth over a window centered on 15 years ago. Weighted moving averaging can shift the center of this window closer toward the current year but some lag always remains. A trailing average is a similar concept that will be discussed below. Moreover, anthropogenic climate change distorts standard statistical metrics: most of the variance in recent 30-year periods derives from the trend rather than internal variability (Fig. 1). Averaging filters (such as a running mean) remove high-frequency signals that reflect year-to-year variations in global weather, as do other statistical approaches better-suited to removing frequencies above a particular cutoff (Smith 2003). The anthropogenic change in Fig. 1 is gradual enough to be mostly preserved by moving averages (running mean) or any lowpass filter / smoother. But this is not true in general: in a hypothetical (or extraterrestrial) climate where forcings undergo an impulse change, such as a quadrupling of $CO_2$ within 1 year as used to evaluate models in the Coupled Model Intercomparison Project (CMIP), the 30-year running mean is an inadequate climate state indicator (see Suppl. Section B, Supp. Fig. 3). Other example applications to Earth's recent GMST of statistical, as opposed to physical, filters used in climate analysis are shown in supplemental Section B (Supp. Figs. 4c,d & 5).

To directly fit the physical effect relating forcings to the climate (incorporating relaxation time), the multi-pattern fingerprint method was developed (Hasselmann 1997), leading to "attributable anthropogenic warming" (Otto et al. 2015) and a "real-time Global Warming Index" (Haustein et al. 2017). This methodology is statistically conservative, generating a wide 5-95% confidence interval spanning ±0.1°C from 1980-2010, and a less certain 5-95% CI of ±0.15°C by 2017.

Policy goals often are framed via climate change staying below a particular policy threshold (e.g., 1.5°C or 2°C above pre-industrial conditions as in the Paris Agreement). Using a 30-year mean

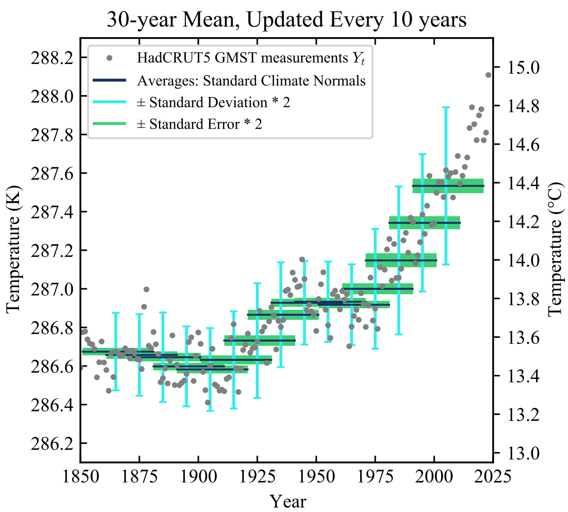


FIG. 1. Illustration of Standard Climate Normals $\overline{_{30}Y_t}$ (blue horizontal lines in 10-year overlapping bins) as applied to the HadCRUT5 GMST dataset (grey dots) (Morice et al. 2021). Twice the population standard deviation (cyan error bars), and two standard errors (green rectangles) are plotted. Note standard deviations widen due to the anthropogenic trend, and the last standard climate normal is cooler than recent GMST measurements.

brings difficulty in determining exactly when or if a policy threshold is crossed (Lee et al. 2021). Policy thresholds are not system thresholds — temperature "tipping" points when the dynamics of the climate system are reorganized, often occurring abruptly or irreversibly — and so they are subject to definitional uncertainty. Relatedly, magnitudes and uncertainty ranges are meaningful only under specific averaging windows, e.g., "GMST increased by 0.85 (0.69 – 0.95) °C between 1850–1900 and 1995–2014 and by 1.09 (0.95 – 1.20)°C between 1850–1900 and 2011–2020." (Gulev et al. 2021). Tools for assessing when a policy threshold has been crossed will be useful as future policy targets approach.

We use both $\mu \pm 2\sigma$ and $\mu(a-b)$ notation to refer to 95% confidence intervals (95% CI), in contrast to $[a-b]$ notation with which we refer to finite or closed ranges. In this notation, $\mu$ is a point estimate, $\sigma$ is a standard deviation, $a$ is the minimum of the interval or range, and $b$ is the maximum. Throughout, a $2\sigma$ or approximately 95% confidence interval is used, indicating the *extremely likely* range in Intergovernmental Panel on Climate Change (IPCC) terminology.

As an alternative to the 30-year running mean and to overcome limited observations sampling the real world, many climate studies instead investigate the climate system within globally coupled climate simulations ("coupled" refers to interacting sub-models, such as atmosphere/ocean/land/ice components), also known as Earth System Models (ESMs: e.g., Meehl et al. 2014). Typically, these simulations are forced using historical records and a range of scenarios for future projections including $CO_2$ emissions, other pollutants, land use, and volcanic eruptions (Lee et al. 2021). The chaotic nature of weather and varying initial conditions produce an ensemble of identically-forced simulations that explore the span of outcomes consistent with forcing, such as for the CESM2 Large Ensemble (LENS2: Rodgers et al. 2021, Supp. Fig. 6). Unfortunately, each coupled ensemble member simulation is computationally expensive and deterministic, so one member does not accurately or transparently reflect the changing climate statistically, but only one realization of it including model errors. Combining such ensembles with real observations yields improvements, such as a more realistic possible spread (due to internal variability) of winter temperatures in North America from 1966-2015 (McKinnon et al. 2017). Betts et al. (2023) proposed avoiding the lag in climate state estimation by combining 10 years of previous observations with a subsequent 10 years forecasted by several ESMs, an approach named the "current global warming level". While useful, this technique oversimplifies some issues inherent to ESMs, such as whether some predictions should be weighted over others (Lehner et al. 2020; Sherwood et al. 2020), or how an ensemble of near-term projections should be initialized (e.g., Yeager et al. 2022).

We sought an efficient and natural estimator of the climate state and its uncertainty: the EBM-KF. We combined a nonlinear energy-balance difference equation (EBM) and a statistical observation equation (KF) that brings in the available measured GMST and OHCA data, yielding a hybrid physical model – statistical filter. This data-driven climate emulator (Forster et al. 2021) is vastly more computationally efficient than ensembles of ESMs that provide similar information about GMST and OHCA. Our emulator is interpretable as a global energy budget (and assimilates OHCA as well as GMST), benefits from the mathematical similarities between an energy balance model and a Kalman Filter, and allows access to proven methodologies for parameter estimation (Chen et al. 2018; Zhang and Atia 2020) and uncertainty quantification (Sætrom and Omre 2013). We did not empirically fit this emulator to the climate record: 12 of the 17 parameters within the energy-balance equation were directly obtained from literature estimates, whereas the remaining 5 parameters are inferred indirectly from assumed pre-industrial climate equilibrium and literature estimates of climate sensitivities. Thus, while some of these parameters were calibrated to the historical climate record independently by other researchers, they were not adjusted to suit this novel EBM combination. Our simple EBM has good skill at predicting the GMST and OHCA despite being by itself "blind" to all measurements (i.e., it's a "forward" model in numerical weather prediction terminology). The statistical component is an Extended Kalman Filter, which allows for incorporation of current measurements to "course-correct" under a well-understood mathematical framework, with time-varying "weather" and "climate state" uncertainty. Other noise covariance matrices are fixed a priori in the Kalman Filter framework to incorporate observational uncertainty. Part of this noise was due to time-varying uncertainty provided with the historical improvements in observations of GMST and OHCA. Another part of the noise covariance was chosen such that the variability in "climate state" most closely resembles the historical 30-year running mean of GMST and OHCA. While perhaps unconventional in data assimilation, this statistical climate state projection approach is directly analogous to the inference of some of our parameters: a handful of numbers were abstracted from the historical climate record using established statistical methods. Hybridizing the EBM with the Extended Kalman Filter yields statistical distributions of internal variability and a physical rationale for the filtered current climate state.

First, the EBM-KF is introduced within Section 2 in phases: the EBM in Section 2a and the structure of the Extended Kalman Filter in Section 2b. An elaboration beyond fixed assumed measurement uncertainty is detailed in Section 2c. The scope of EBM-KF is expanded to future projections including volcanic eruptions in Section 2d. In Section 3, variants of the EBM-KF are illustrated on four applications to historical and future climate. Section 3a shows that it estimates the 30-year mean climate normal every year, including the latest observations and without lag. Section 3b shows how it can be used to assess the probability that a policy threshold has been crossed in any particular year. Section 3c shows how it can be used to estimate the ensemble mean of an ESM Large Ensemble from only one ensemble member. Section 3d shows that the EBM-KF is sufficiently fast to allow high-density sampling of non-Gaussian probabilistic futures, e.g., directly sampling over highly intermittent distributions of future volcanic eruptions. Section 4 discusses these results, some cautionary remarks, opportunities for extension, and application to policymaking. Section 5 concludes. The detailed EBM-KF code is available and the equations as coded are provided in Appendix A, and a glossary of mathematical symbols is provided in Appendix C. Extensive appendices and supplementary material convey additional detail.

## 2. Methods

### *a. Energy-Balance Model*

We constructed the energy-balance model (Fig. 2) by envisioning a uniform planet and capturing the principal atmospheric and surface energy fluxes (Budyko 1969; Sellers 1969). This model is "blind" with respect to observations and is inspired by other energy-budget models illustrating quantitative skill (Hu and Fedorov 2017; Kravitz et al. 2018) at approximating both GMST and the 30-year running mean. The model includes two idealized layers, with each layer having homogenous temperature: a surface layer including thermally active soil and 86m average ocean water depth (with temperature approximating GMST), and a deep ocean layer reaching (1141+86)m depth that exchanges energy (part of OHCA) with the surface layer (Geoffroy et al. 2013b; Gregory 2000; Held et al. 2010). These depths are chosen to select a two-state system that best represents the heat capacities of spatially complex heat uptake patterns in total into the global oceans (Newsom et al. 2023), rather than representing the heat uptake relative to depths associated with observational oceanographic traditions (e.g. 700m, 2000m). As this EBM does not directly incorporate any spatial dimensions, it should be considered 0-dimensional in the context of other ESMs with spatial gradients. Closely related variables to GMST, such as Global Surface Air Temperature (GSAT), differ only from GMST by measurement and slightly in uncertainty (by less than our confidence intervals) but not systematically (Gulev et al. 2021).

The energy budgets for the EBM layers and the energy fluxes are (Fig. 2):

$$C_{\mathrm{surf}}\frac{dT}{dt} = \mathcal{F}_{\mathrm{SW}}(T,t) - \phi_{\mathrm{LW}}(T,t) - \gamma \cdot (T - \theta - \zeta_0) \tag{1}$$

$$C_{\mathrm{deepO}}\frac{d\theta}{dt} = \gamma \cdot (T - \theta - \zeta_0) \tag{2}$$

$$H = (T - T_{1850}) \cdot C_{\mathrm{upperO}} + (\theta - \theta_{1850}) \cdot C_{\mathrm{deepO}} \tag{3}$$

$$\mathcal{F}_{\mathrm{SW}}(T,t) = \left(\frac{1}{4}G_{\mathrm{SC}}\right)_t \cdot \tilde{d}(t) \cdot f_{\alpha A}(T,t) \cdot f_{\alpha S}(T) \tag{4}$$

$$\phi_{\mathrm{LW}}(T,t) = \sigma_{sf}T^4 \cdot \tilde{g}(t) \cdot f_{H_2O}(T) \tag{5}$$

$T$ is GMST, whereas $\theta$ is the Conservative Temperature of the deep ocean in that same year, and $H$ is OHCA including both that deep ocean layer and the surface ocean (McDougall et al. 2021). The time variable $t$ is the calendar year index, and often used as a subscript (e.g. $T_{2000}$ is the modeled GMST in the year 2000, or $(\frac{1}{4}G_{SC})_t$ is a direct forcing record at index $t$). On the right side of the equation, both the shortwave radiative flux ($\mathcal{F}_{SW}(T,t)$) and longwave radiative flux ($\phi_{\mathrm{LW}}(T,t)$) take the same form: (source $\frac{1}{4}G_{SC}$ or $\sigma_{sf}T^4$) $\times$ (prescribed attenuation from forcing: $\tilde{d}(t)$ or $\tilde{g}(t)$ ) $\times$ (attenuation functions with feedback: $f(T)$ with various subscripts). The attenuation function of clouds on shortwave radiation $f_{\alpha A}(T,t)$, contains both prescribed forcing and feedback. The overall surface heat capacity, $C_{\mathrm{surf}}$, is 17 ± 7 W (year) m$^{-2}$ K$^{-1}$, obtained from modeling / timeseries analysis (Schwartz 2007), including 11.7 W (year) m$^{-2}$ K$^{-1}$ or 86m of upper surface ocean $C_{\mathrm{upperO}}$, while there is a separate deep ocean heat sink with capacity 155.7 W (year) m$^{-2}$ K$^{-1}$ or 1141m $C_{\mathrm{deepO}}$ (Geoffroy et al. 2013b). $\frac{1}{4}G_{SC}$ is the total solar irradiance (TSI) normalized to the Earth's surface area at $\frac{1}{4}\overline{G_{SC}} \approx 340.2$ W/m$^2$. We elected to incorporate the record $(\frac{1}{4}G_{SC})_t$ of [340.06 – 340.48] from Coddington et al. (2017) but these variations are insignificant. $\tilde{d}(t)$ is the prescribed record of shortwave radiation attenuation due to $AOD_t$ (from Sato et al. (1993), Vernier et al. (2011), and NASA/LARC/SD/ASDC (2018)), $f_{\alpha A}(T,t)$ is the additional atmospheric shortwave attenuation due to cloud albedo incorporating both feedback and anthropogenic cloud-nucleating aerosols $AC_t$, while $f_{\alpha S}(T)$ is the surface shortwave attenuation due to ground albedo. Infrared radiation emitted from the surface is $\sigma_{sf}T^4$, the ideal Planck blackbody radiation. $\tilde{g}(t)$ is the prescribed record of longwave attenuation due to $CO_2$ and other greenhouse gasses combined as effective carbon dioxide concentration $[eCO_2]_t$, and $f_{H_2O}(T)$ is the additional atmospheric longwave attenuation due to water vapor parameterized as a function of GMST. For reference, Appendix C tabulates all mathematical symbols used in this paper.

In the discussion section (4a) we will discuss variants of the EBM-KF, constructed by pre-filtering the input forcings. If we pre-filter inputs (indicated by EBM-KF-ta, abbreviating "trailing average"), then the output estimated climate state more closely approximates the 30-year running mean of GMST and OHCA. Without pre-filtering (indicated by EBM-KF-uf, abbreviating "unfiltered"), the estimate climate state more closely resembles the ensemble mean of GMST and OHCA across members of a coupled ESM ensemble such as LENS2. Pre-filtering is inconsequential for greenhouse gasses which evolve slowly but is consequential for aerosol optical depth over

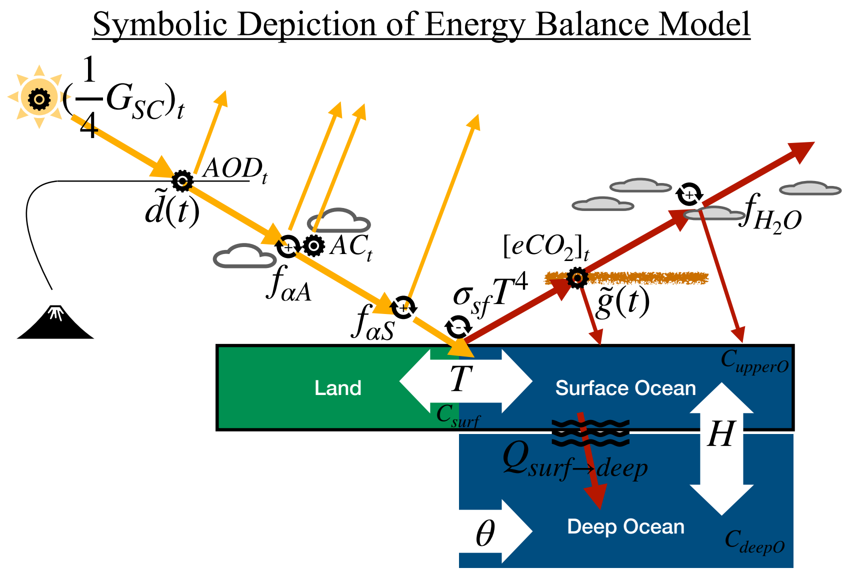


FIG. 2. Diagram of the Energy Balance Model, with all major forcing functions, corresponding climate driver datasets, and feedback functions represented. All feedback functions are dependent on surface temperature $T$, but this is not written on the diagram. Shortwave incoming solar radiation is successively fractionated by various forcing and feedback functions (indicated by circling arrows), as is outgoing longwave radiation. These in net warm the surface layer, which in turn warms the deep ocean. Anthropogenic forcing effects are indicated by a small gear (or cog). See equations 1-5.

the impulse changes during volcanic eruptions. All equations within the Energy Balance Model (section 2a) and the Kalman Filter (section 2b) are used regardless of pre-filtering. Thus we will refer to EBM-KF when a statement is relevant all variants, and in sections 3 and 4 specify which variant in each application.

Both $AC_t$ and $\tilde{g}(t)$ are taken from Forster et al. (2023). Several of the coefficients within the feedback functions $f$ are defined to satisfy the constraints of the climate feedbacks presented in the IPCC AR6 (Forster et al. (2021); particularly Table 7.10), and all coefficients are based on observational and modeling literature values, typically with energy fluxes measured from satellites and temperature feedback coefficients determined from model results (full derivation in Appendix A and Supplement A). Because the Planck radiation requires absolute temperatures, we use degrees Kelvin in model calculations and convert to °C. OHCA is also approximately convertible to thermosteric sea level rise, via the 0.0121 cm/ZJ factor from analysis of 1995 to 2014 (Fox-Kemper et al. 2021). With this factor, the estimated thermosteric sea level rises we find are consistent with observations and projections. The two negative albedo attenuations $f_{\alpha A}(T,t) \cdot f_{\alpha S}(T)$ are expressed relative to $Y_{2002}$ =287.55K (14.40°C), the inferred (see below) GMST measurement in 2002 (Jones and Harpham 2013; Morice et al. 2021).

$\zeta_0$ = 10°C is an equilibrium temperature difference between the surface layer (including the upper ocean) and the deep ocean, arising because the global ocean is thermally stratified. This realistic choice of $\zeta_0$, explained below, does not affect either $T$ or $H$, provided that  and $T$ are in equilibrium at the model's preindustrial initialization (and thus $\zeta_0$ is often abstracted away in similar 2-layer energy-balance models) (Geoffroy et al. 2013b; Gregory 2000; Held et al. 2010). $\gamma$ is the thermal conductivity or "efficiency" between layers of the ocean, taken from Geoffroy et al. (2013a) to be 0.67 W/m$^2$/K, the average from the CMIP5 models. The form of this parameterization of deep ocean temperature exchange follows recent work in emulating ocean heat uptake, but ignoring "efficacy factor" heat loss (Emile-Geay et al. 2017; Geoffroy et al. 2013b; Gregory 2000; Palmer et al. 2018a; Winton et al. 2010).

We first obtained the baseline $\zeta_1$=287.01K of the HadCRUT5 GMST anomaly (Morice et al. 2021) to place the 1960-1989 "standard climate normal" of absolute GMST HadCRUT5 measurements to fall at 13.85°C, the center of the range (13.7 - 14°C) given by Jones and Harpham (2013). We symbolize the HadCRUT5 GMST anomaly record as $HCa_t$. Measurements of surface temperature will later be assimilated as absolute temperatures: $Y_t = \zeta_1 + HCa_t$. Our model assumes energy fluxes were balanced before industrial forcings, which requires an equilibrium temperature. We set this preindustrial equilibrium temperature to the 1850-1879 "standard climate normal" of 286.67K (13.52°C) = $T_{1850}$, and initialized the 1850 climate state to this temperature. This choice is important regarding the determination of many nonlinear feedback functions and coefficients affecting the surface layer (Eq. 7 below), particularly with respect to the Planck feedback. Inconsequentially to the EBM dynamics, the deep ocean Conservative Temperature $\theta$ was initialized to be 276.67K (3.52°C) = $\theta_{1850}$, such that current deep ocean Conservative Temperatures are ≈ 3.8°C, choices consistent with both recent and historical measurements of the globally averaged values (Abraham et al. 2013; Robinson and Stommel 1959). So $\zeta_0$= $T_{1850} - \theta_{1850}$ = 13.52°C - 3.52°C = 10°C. Initializing the deep ocean Conservative Temperature $\theta$ to another value would change $\zeta_0$ correspondingly, such that the modeled heat flow into the deep ocean would be unchanged.

TABLE 1. Constants and climate driver datasets referenced in (6-8), in addition to temperature baselines. Equations referenced in "Source" column are found in Appendix A and Supplement SA1& SA2.

| Symbol | Value [Range] | Derivation or Def. | Source |
|---|---|---|---|
| $\zeta_1$ | 287.01 K (13.86°C) | $13.85\ °C = \zeta_1 + \frac{1}{30}\sum_{t=1960}^{1989} HCa_t$ | Jones and Harpham (2013) |
| $Y_{2002}$ | 287.55 K (14.40°C) | $\zeta_1 + HCa_{2002}$ | Morice et al. (2021) |
| $T_{1850}$ | 286.67K (13.52°C) | $\zeta_1 + \frac{1}{30}\sum_{t=1850}^{1879} HCa_t$ | Morice et al. (2021) |
| $\theta_{1850}$ | 276.67K (3.52°C) | approx. deep ocean temp. | Abraham et al. (2013) |
| $\zeta_0$ | 10 K (10°C) | $T_{1850} - \theta_{1850}$ | Abraham et al. (2013) |
| $\gamma$ | $0.67 \frac{W}{K\ m^2}$ | Ocean heat conductivity/year | Geoffroy et al. (2013a) |
| $C_{\text{surf}}$ | $17 \frac{W}{K\ m^2}$ | Heat capacity/year, Earth surface | Schwartz (2007) |
| $C_{\text{upperO}}$ | $11.7 \frac{W}{K\ m^2} (86m\ H_2O)$ | Heat capacity/year, upper ocean | Geoffroy et al. (2013a) |
| $C_{\text{deepO}}$ | $155.7 \frac{W}{K\ m^2} (1141m\ H_2O)$ | Heat capacity/year, deep ocean | Geoffroy et al. (2013a) |
| $\eta$ | 1.615 | Degree (exponent) of $H_2O$ feedback | (A26), (A27) |
| $\beta_0$ | 0.04660 | Infrared reflection per $\log_{10}$ ppm $CO_2$ | (A20), (A21), (A35) |
| $c_1$ | $2.198910^{-5} K^{-3+\eta}$ | $\sigma_{sf}\beta_1 / C_{\text{surf}}$ | (A22), (A35) |
| $\beta_2$ | $0.00136 K^{-1}$ | Atm. albedo temp. feedback | (A13), (A28) |
| $\beta_3$ | $0.00163 K^{-1}$ | Ground albedo temp. feedback | (A14), (A29) |
| $c_2$ | $0.4044 \frac{K\ m^2}{W}$ | $0.834 \cdot 0.909 \cdot 9.068 / C_{\text{surf}}$ | (A11), (A23), (A24) |
| $c_3$ | $264.377 \frac{W}{m^2}$ | $\frac{1}{4}\overline{G_{SC}}\tilde{d}_{2002} 0.834$ | (A23) |
| $c_4$ | 9.73 (unitless) | $2q'/(1-g)$ | (A11), eq9 of Harshvardhan and King (1993) |
| $AC_{2002}$ | $-0.988 \frac{W}{m^2}$ | Anthro. cloud rad. forcing, 2002 | (A23) |
| $(\frac{1}{4}G_{SC})_t$ | $[340.06 — 340.48] \frac{W}{m^2}$ | Top of atm. total solar irradiance | Coddington et al. (2017) |
| $AOD_t$ | [0.2 — 142.9] | Aerosol optical depth | Miller et al. (2014); NASA/LARC/SD/ASDC (2018) |
| $AC_t$ | $[-1.09 — -0.06] \frac{W}{m^2}$ | Anthro. cloud radiative forcing | Forster et al. (2023) |
| $[eCO_2]_t$ | [287.9 — 563.4] | Effective CO2 concentration, ppm | Forster et al. (2023) |

With the considerations above, equations (1-5) become:

$$\theta_t = \left(H_t - (T_t - T_{1850}) \cdot C_{\text{upperO}}\right) / C_{\text{deepO}} + \theta_{1850} \tag{6}$$

$$\begin{aligned} T_{t+1} = T_t + \frac{(\frac{1}{4}G_{SC})_t \cdot c_2}{(AOD_t + c_4)} &\left(1 + \beta_2 (T_t - Y_{2002}) + \frac{AC_t - AC_{2002}}{c_3}\right)\left(1 + \beta_3 (T_t - Y_{2002})\right) \\ &- c_1 \cdot (T_t)^{4-\eta}\left(1 - \beta_0 \log_{10}([eCO_2]_t)\right) - \frac{\gamma}{C_{\text{surf}}}(T_t - \theta_t - \zeta_0) \end{aligned} \tag{7}$$

$$H_{t+1} = H_t + (T_{t+1} - T_t) \cdot C_{\text{upperO}} + \gamma \cdot (T_t - \theta_t - \zeta_0) \tag{8}$$

Future projections along the shared socioeconomic pathways (SSPs) for the EBM-KF also require the concentrations of greenhouse gasses including carbon dioxide $[eCO_2]_t$, aerosol optical depth due to volcanic and human emissions ($AOD_t$), and the computed effect from anthropogenic clouds ($AC_t$). ESMs simulate the carbon cycle and thus find an equivalent of $[eCO_2]_t$ from specified $CO_2$ and greenhouse gas emissions, but our EBM-KF does not have this capability. Future greenhouse gas concentrations and anthropogenic cloud forcings are instead taken from a conversion of anthropogenic fluxes by the MAGICC7.0 carbon cycle emulator (Meinshausen et al. 2020), as reported by Smith et al. (2021). For instance, SSP1-2.6 and SSP3-7.0 are shown in Figs. 9 & 10, which flank the most likely result of current environmental policies (Pielke Jr et al. 2022). Projection of anthropogenic forcings from Nazarenko et al. (2022) using the NASA GISS ESM yield very similar future curves (not shown).

Overall, the blind (forward) energy-balance model (orange dashed line in Fig. 2) has 4 yearly forcing inputs $[eCO_2]_t$, $AOD_t$, $AC_t$, $(\frac{1}{4}G_{SC})_t$ and 17 irreducible parameters (including 1 inferred exponent $\eta$, 4 inferred $\beta$ coefficients, 3 heat capacities, and 3 reference temperatures). The time step of this iterative difference equation model is 1 year chosen arbitrarily to coincide with the calendar year. The deep ocean Conservative Temperature $\theta_t$ is recalculated at each time step from the GMST $T_t$ and the OHCA $H_t$ by (6), and then these two terms are updated with (7, 8). The measured temperature in the year 2002 ($Y_{2002}$) appears prominently in this model because that was the midpoint of the measurement window of the CERES satellite (Loeb et al. 2009; Wielicki et al. 1996), and all albedo-related feedbacks are expressed relative to these measurements. For this model, the OHCA ($H_t$) is calculated in units of W year m$^{-2}$ on an average of the Earth's surface, and then converted to ZJ within the ocean by multiplying by a factor of

$$11.42\frac{\text{m}^2\ \text{ZJ}}{\text{year W}} = \frac{3.154\cdot 10^7\text{s}}{1\text{year}}\ \frac{5.101\cdot 10^{14}\text{m}^2}{\text{Earth surface area}}\ \frac{\text{ZJ}}{10^{21}\text{J}}\ \frac{0.71\text{m}^2\ \text{(ocean)}}{\text{m}^2\ \text{(total area)}}.$$

This time-step function (6-8) and its partial derivative (see Appendix A4) will become critical parts of our Kalman Filter (9, 10) below.

This blind EBM model has good skill at predicting the GMST with $r^2$=0.908 when compared to the HadCRUT5 GMST timeseries (Morice et al. 2021), and OHCA with $r^2$=0.910 when compared with the inferred history (Zanna et al. 2019), as is demonstrated by the dashed orange lines in Fig. 3. The blind EBM has a comparably high correlation ($r^2$=0.923) with the 30-year running mean (i.e., the climate normal) of the HadCRUT5 GMST, indicating that this forward energy balance model also has skill in reproducing the climate state as determined by standard approaches, with departures due to volcanic eruptions. Thus, most observed climate change can be explained by the literature-based blind, forward EBM with records of emissions (greenhouse gasses, anthropogenic clouds) and measurements at the top of the atmosphere of aerosol optical depth. The distribution of residuals in the GMST record from either the 30-year running mean or the EBM has small bias and skewness (see Supp. Fig. 9). These residuals' kurtosis is slightly less than Gaussian to accommodate measurement uncertainty, as discussed in Section 3a in relation to Figs. 4 & 5. So, the 30-year running mean's "weather" or "noise" empirical probability density function combining residuals and measurement uncertainty is very nearly Gaussian, and thus amenable to treatment by a Kalman filter framework (see section 2b). The Fig. 3 forward model comparisons were made without any assimilated data, illustrating that the EBM physics alone has skill in reproducing aspects of the GMST and OHCA records. Tuning the EBM parameters may further improve skill, but the EBM is only the forward projection component of the data assimilating Kalman Filter hybrid model described in the next section. The combined system is the focus of this paper.

### *b. EBM-Kalman Filter: A Weighted Average of Energy Balance and Measurements*

While similar algorithms were developed in the 1880s by Thorvald Nicolai Thiele (Lauritzen and Thiele 2002; Lauritzen 1981), Kalman filtering rose to prominence due to its use in the Apollo navigation computer as proposed by Stratonovich (1959, 1960), Swerling (1959), Kàlmàn (1960), Bucy (Kàlmàn and Bucy 1961), and implemented by Schmidt (1981). Versions of this statistical filter are universally used in aerospace guidance systems (Grewal and Andrews 2001), aspects of numerical weather prediction (Houtekamer and Mitchell 1998; Kalnay 2002), and recently popularly in climate science as Ensemble Kalman filters (which use a Monte Carlo approximation via simulations in high-dimensional space, see below).[1] Despite the success of Ensemble Kalman filters, Extended Kalman filters are inapplicable as the sole data assimilation tool for regional weather patterns (Bouttier 1996), because local weather processes do not sample from a Gaussian distribution, the core assumption of Extended Kalman filters. The multidimensional Extended

[1] Ensemble Kalman filters (not to be confused with Extended Kalman filters, the local linearization extension method of this paper) have been instrumental to 20$^{\text{th}}$ century reanalysis (Compo et al. 2011) and last millennium reanalysis projects (Hakim et al. 2016) of global atmospheric circulation. In the Ensemble Kalman Filter, assimilated observations sample the full gridded weather patterns (a space with hundreds to millions of dimensions) within an ensemble of ESMs.

Kalman filter assumes:

$$\mathbf{x}_t = \mathbf{F}(\mathbf{x}_{t-1}; u_t) + \mathbf{w}_t \qquad \text{climate state update: } \mathbf{x}_t,\ \text{uncertainty: } \mathbf{w}_t \sim \mathcal{N}(\mathbf{0}, \mathbf{Q}) \tag{9a}$$

$$\mathbf{y}_t = \mathbf{x}_t + \mathbf{v}_t \qquad \text{weather state: } \mathbf{y}_t,\ \text{uncertainty: } \mathbf{v}_t \sim \mathcal{N}(\mathbf{0}, \mathbf{R}) \tag{9b}$$

Bold type indicates state vectors. In this case of global GMST and OHCA, an Extended Kalman Filter works because both measurement and dynamical noise are approximately Gaussian (by Central Limit Theorem expectation[2] verified in Section 3 and Supp. Fig. 9), and because the energy-balance equation (Section 2a, equations (1)-(5)) have a continuous and bounded gradient of $\mathbf{F}(\mathbf{x}_{t-1}; u_t)$ (see (6)-(8) and Supplement Section D), so it can be locally linearized.[3] This approximate linearity means that more complex realizations of the Kalman filter, particularly the Unscented Kalman Filter (Julier and Uhlmann 1997; Wan and Van Der Merwe 2000), are not necessary (see Supplement Section D). This approach has already proven successful using a 1-(spatial)-dimensional (north-south) energy balance model, with time-steps of decades (or longer), and optimized for use in paleoclimate research (García-Pintado and Paul 2018). Thus, for a variety of reasons an EBM-Kalman Filter (EBM-KF) can be built from an Extended Kalman Filter combined with an (annual, 0-spatial-dimensional) Energy Balance Model.

In-depth derivations and tutorials for constructing Kalman filters have been published elsewhere (Benhamou 2018; Lacey 1998; Miller 1996; Ogorek 2019; Särkkä 2013; Kim and Bang 2018). Here we describe enough for basic intuition, and we refer readers to Kalnay (2002), page 281, for a more detailed explanation with alternative notation. We use the term “forecast” where other authors use “prior”, and we avoid use of “measurement error” in a manner that would be ambiguous and confusing in this application. Our equations for the Extended Kalman Filter (the KF part of the EBM-KF) are:

[2]The Central Limit Theorem states that taking the average of many independent samples from the same non-Gaussian distribution with bounded moments will produce a mean that approximates a Gaussian distribution (Montgomery and Runger 2013). This is the case for the de-trended annual GMST, a climate state variable composed of the average of many non-Gaussian regional and daily weather patterns (Hu and Fedorov 2017; **?**; **?**; **?**). Likewise, while annual OHCA is largely constrained by the subtropical pycnocline depth (Newsom et al. 2023), it too is comprised of numerous regional and seasonal patterns (Cheng et al. 2017; Huguenin et al. 2022; Hummels et al. 2013). Many dynamical components of the global oceans are non-Gaussian, such as velocity (**?**) and sea surface height (**??**).

[3]Careful construction of the EBM with $T^2$ in the shortwave term and $T^{2.39}$ in the counteracting longwave term in (1) & (5) ensures the derivative (A21 - A24) does not change significantly over the relevant range of temperatures [286 — 291]K, $[eCO_2]_t$ effective $CO_2$ concentrations [278 — 2000] ppm, $AOD_t$ aerosol optical depths [0 — 0.15], and $AC_t$ anthropogenic cloud forcing [-1 — 0] W/m$^2$.

$$\mathbf{\Phi}_t = \left.\frac{\partial \mathbf{F}(\mathbf{x};u_t)}{\partial \mathbf{x}}\right|_{\mathbf{x}=\hat{\mathbf{x}}_{t-1}} \qquad \text{local linearization at timepoint } t \tag{10}$$

$$\hat{\mathbf{x}}_{t|t-1} = \mathbf{F}(\hat{\mathbf{x}}_{t-1};u_t) \qquad \text{forecast ("prior") state estimate} \tag{11}$$

$$\mathbf{P}_{t|t-1} = \mathbf{\Phi}_t \mathbf{P}_{t-1} \mathbf{\Phi}_t^* + \mathbf{Q} \qquad \text{forecast ("prior") covariance} \tag{12}$$

$$\mathbf{z}_t = \mathbf{y}_t - \hat{\mathbf{x}}_{t|t-1} \qquad \text{innovation residual} \tag{13}$$

$$\mathbf{S}_t = \mathbf{P}_{t|t-1} + \mathbf{R}_t \qquad \text{innovation covariance} \tag{14}$$

$$\mathbf{K}_t = \mathbf{P}_{t|t-1}(\mathbf{S}_t)^{-1} \qquad \text{Kalman gain} \tag{15}$$

$$\hat{\mathbf{x}}_t = \hat{\mathbf{x}}_{t|t-1} + \mathbf{K}_t \mathbf{z}_t \qquad \text{posterior state estimate} \tag{16}$$

$$\mathbf{P}_t = (\mathbf{I} - \mathbf{K}_t)\mathbf{P}_{t|t-1} \qquad \text{posterior state covariance} \tag{17}$$

We proceed through this mathematical algorithm (10)-(17) as follows. Initially, there is some *estimated state vector* (GMST and OHCA within this paper) $\hat{\mathbf{x}}_{t-1}$ and a Gaussian uncertainty envelope around this vector defined by a *state covariance matrix* $\mathbf{P}_{t-1}$. In the basic setup of a Kalman fitler, the state vector is transformed (or projected) one year into the future using a *dynamic model Jacobian matrix* $\mathbf{\Phi}_t$ into a *forecast state* $\hat{\mathbf{x}}_{t|t-1} = \mathbf{\Phi}_t \hat{\mathbf{x}}_{t-1}$, a transformation that may depend on time-varying control parameters $u_t$. For our climate system this linear projection is extended to the nonlinear function $\hat{\mathbf{x}}_{t|t-1} = \mathbf{F}(\hat{\mathbf{x}}_{t-1};u_t)$ in (11), which is just the forward energy balance model equations (6)-(8), where $u_t$ represents the collection of climate forcings: $[eCO_2]_t$, $AOD_t$, $AC_t$, $(\frac{1}{4}G_{SC})_t$.This simple extension to nonlinearity is the meaning of "Extended" Kalman Filter. The *state covariance* $\mathbf{P}_{t-1}$ is projected to the next year using the local linear approximation of the *dynamic model Jacobian matrix* $\mathbf{\Phi}_t$ (10) and enlarges by an additional *assumed model error covariance* $\mathbf{Q}$, yielding $\mathbf{P}_{t|t-1}$ the *forecast covariance* (12). To arrive at a posterior, information from a *measurement vector* $\mathbf{y}_t$ is considered (13).[4] The probabilistic range of anticipated discrepancies between $\hat{\mathbf{x}}_{t|t-1}$ and $\mathbf{y}_t$ is given by the *innovation covariance matrix* $\mathbf{S}_t$, which is the sum of $\mathbf{P}_{t|t-1}$ and an *assumed measurement covariance* $\mathbf{R}_t$ (14). The *posterior estimate of the state* $\hat{\mathbf{x}}_t$ is found by taking a weighted average of $\hat{\mathbf{x}}_{t|t-1}$ and $\mathbf{y}_t$ (16), with the weight on $\mathbf{y}_t$ given by $\mathbf{P}_{t|t-1}(\mathbf{S}_t)^{-1}$, a product known as the *Kalman gain* $\mathbf{K}_t$ (15). To reflect the greater certainty in the state vector

[4]If $\mathbf{y}_t$ is an indirect measurement of the hidden state vector $\mathbf{y}_t$, an observation (or emission) matrix $\mathbf{H}$ further complicates the procedure (details in the references above). Here we consider only direct "observations" of GMST and OHCA making mapping and interpolation errors implicit and the observation matrix $\mathbf{H} = \mathbf{I}$, the identity matrix.

because of this correction, $\mathbf{P}_t$, the *posterior covariance matrix*, is $\mathbf{P}_{t|t-1}$ shrunk by the *Kalman gain*, $\mathbf{I}-\mathbf{K}_t$ per (17). Within the context of climate modeling, this "*posterior state estimate*" $\hat{\mathbf{x}}_t$ is somewhat analogous to a climate reanalysis product, as both combine observations and models. Within the context of Bayesian probability, the prior (forecast) distribution is given by projecting $\mathcal{N}(\hat{\mathbf{x}}_{t-1}, \mathbf{P}_{t-1})$ into the future using the Jacobian matrix $\mathbf{\Phi}_t$, which is multiplied by the marginalized likelihood of $\mathbf{y}_t$ to give a posterior distribution $\mathcal{N}(\hat{\mathbf{x}}_t, \mathbf{P}_t)$. Note that $\mathbf{\Phi}_t^*$ in (12) above indicates matrix transposition.

The true climate state $\mathbf{x}_t$ is the 2-entry vector underlying GMST and OHCA, filtering out weather and internal variability: $\mathbf{x}_t = [T_t\ ,\ H_t]$ . Throughout this paper, $[a\ ,\ b]$ indicates a 2-dimensional vector with components $a$ and $b$. The noisy measurements $\mathbf{y}_t = [Y_t, \psi_t]$ are the yearly time series of GMST and OHCA, and $\hat{\mathbf{x}}_t = [\hat{T}_t\ ,\ \hat{H}_t]$ is the estimate of the unknown 2-dimensional climate state, expressed in degrees Kelvin and $\frac{W\ year}{m^2}$ (convertible to ZJ by the factor 11.42 $m^2$ ZJ $W^{-1}$ $year^{-1}$). The energy-balance model's $\mathbf{F}(\hat{\mathbf{x}}_{t-1}; u_t)$ in (10) governing $T$ and $H$ is nonlinear (as described above with $T^2$ and $T^{2.385}$ terms due to albedo, Planck, and water vapor feedbacks) (Friedrich et al. 2016), which necessitates linearization. In our Extended Kalman Filter, the forecast state $\hat{\mathbf{x}}_{t|t-1}$ (11) is given by (6)-(8) above and $\mathbf{\Phi}_t$ and the forecast covariance projection $\mathbf{P}_{t|t-1}$ (12) is a time-varying linearization (A21)-(A25). This energy-conserving difference equation thus resembles a first-order Taylor series approximation of a differential energy-balance model (if discretization errors are considered part of the tendency), or the integral form of a conservative discretization in time (if shortwave and longwave fluxes are taken as a model for their time-integrated value), and the Kalman Filter re-approximates a GMST and OHCA climate state every year. The initial estimated state uncertainty is intentionally overestimated at $\mathbf{P}_{1850} = \begin{bmatrix} 1K^2 & 1\ K\frac{W\ year}{m^2} \\ 1\ K\frac{W\ year}{m^2} & 20\ \left(\frac{W\ year}{m^2}\right)^2 \end{bmatrix}$ and then $\mathbf{P}_t$ rapidly converges in the EBM-KF-uf (and EBM-KF-ta) to $\mathbf{P}_{1865} = \begin{bmatrix} 0.0017\ K^2 & 0.035\ K\frac{W\ year}{m^2} \\ 0.035\ K\frac{W\ year}{m^2} & 4.0\ \left(\frac{W\ year}{m^2}\right)^2 \end{bmatrix}$, and then continues to slowly shrink with time as more accurate measurements are made. For convenience we form confidence intervals for the GMST climate state (19) and OHCA climate state by taking twice the square root of the respective diagonal elements of $\mathbf{P}_t$ (18a).

$$[\hat{p}_t^T, \hat{p}_t^H] = \mathrm{diag}(\mathbf{P}_t) \tag{18a}$$

$$[\hat{s}_t^T, \hat{s}_t^H] = \mathrm{diag}(\mathbf{S}_t) \tag{18b}$$

For example,

$$\text{95\% CI of estimated GMST state, 1865:} \qquad \hat{T}_{1865} \pm 2\sqrt{\hat{p}^T_{1865}} = 286.66\,\mathrm{K} \pm 2\sqrt{0.0017\,\mathrm{K}^2}$$
$$= 286.66\,\mathrm{K} \pm 0.07\,\mathrm{K} \tag{19}$$

We give both diagonal elements their own symbols, and similarly for $\mathbf{S}_t$ (18b) noting that here superscripts $T$ and $H$ are labels not exponentiation. Similarly to (19), we use the diagonal elements of $\mathbf{S}_t$ to form confidence intervals of next-year measurements about $\hat{\mathbf{x}}_{t|t-1}$. These confidence intervals are functions of time, as indicated by the subscript.

The Extended Kalman Filter implicitly assumes that Gaussian "model" noise is added to this climate state at each time step (9a), and additionally the climate state emits annual "weather variability" from a yet wider Gaussian noise distribution (9b) quantified by measurement uncertainty $\mathbf{R}_t$ combined with the forecast covariance and so $\mathbf{S}_t$ (14). Whereas we interpret global annual weather to be the noisy measurements $\mathbf{y}_t = [Y_t, \psi_t]$, "weather variability" is observed via *innovation residuals* $\mathbf{z}_t$.

$$z_t^T = Y_t - \hat{T}_{t|t-1} \tag{20a}$$

$$z_t^H = \psi_t - \hat{H}_{t|t-1} \tag{20b}$$

These *innovation residuals* have components $\mathbf{z}_t = [z_t^T, z_t^H]$, and the Kalman Filter expects them to come from an unbiased Gaussian noise distribution with covariance $\mathbf{S}_t$ (not $\mathbf{R}_t$ because the Kalman Filter does not have knowledge of the true climate state $\mathbf{x}_t$).

The EBM-KF climate state $\hat{\mathbf{x}}_t$ and state covariance $\mathbf{P}_t$ are causal in time at each year $t$, so they only access information from the measurements taken prior to and at year $t$: $\{\mathbf{y}_{1850}, \mathbf{y}_{1851}, \ldots, \mathbf{y}_t\}$. This past-to-present Kalman Filter incorporated into the EBM-KF (10)-(17) could be further extended into a RTS smoother (Rauch et al. 1965) by additional steps (see Supplement SA3), which meld information from all measurements in the time window: $\{\mathbf{y}_{1850}, \mathbf{y}_{1851}, \ldots, \mathbf{y}_{2023}\}$ into each re-estimated posterior state $\hat{\hat{\mathbf{x}}}_t$ and posterior state covariance $\hat{\hat{\mathbf{P}}}_t$ by running backward from the latest EBM-KF state estimates $\hat{\mathbf{x}}_{2023}$ and $\mathbf{P}_{2023}$. However, in the 1850 to present application, this extension has little effect on $\hat{\mathbf{x}}_t$ (Supplemental Fig. 2), with the only impacts being greater certainty in the smoothed state at the cost of violation of causality. Defining as in (18a) $[\hat{\hat{p}}_t^T, \hat{\hat{p}}_t^H] = \mathrm{diag}(\hat{\hat{\mathbf{P}}}_t)$, for the GMST uncertainty $\hat{p}_t^T \approx 2.25 \cdot \hat{\hat{p}}_t^T$, and for the OHCA uncertainty $\hat{p}_t^H \approx 2.84 \cdot \hat{\hat{p}}_t^H$ (within the EMB-KF-uf). Overall, we deemed this extension not worth the added complications and retained the past-to-present, causal approach.

In summary, the Extended Kalman Filter projects forward one year into the future based on the unbalanced fluxes of the energy balance model equation, and then takes a weighted average of this projection with the annual GMST measurement (the data assimilation increment). Thus, even though the EBM conserves energy (by construction), the combined EBM-KF does not, unlike other alternative data assimilation approaches (Wunsch and Heimbach 2007). The state estimates from this EBM-KF (in navy blue in Fig. 3) often lie between the blind EBM (in dashed orange in Fig. 3) and the annual temperature measurements (scattered gray dots in Fig. 3). These data assimilation corrections can be seen most clearly within the GMST measurements in Fig. 3a from 1900 to 1945 and within the OHCA measurements in Fig. 3b from 1940 to 1970. It is possible for the EBM-KF state estimates to escape these bounds for a short time, for instance from 1945 to 1950 in Fig. 3a or after 2007 in Fig 3b. These "escape periods" may reflect bias in the measurements, such as warm-biased WWII-era measurements of (sea) surface temperature (Chan and Huybers 2021) or bias in the Zanna et al. (2019) OHCA product (which may be indicated by this product having less heat uptake since 2005 than all but 1 of 19 other OHCA estimates: Gulev et al. 2021). Both the "blind" EBM predictions $[\tilde{T}_{t+1}, \tilde{H}_{t+1}] = \mathbf{F}(\tilde{T}_t, \tilde{H}_t;\ u_t)$, and EBM-KF-uf state estimates $\hat{\mathbf{x}}_t = [\hat{T}_t\ ,\ \hat{H}_t]$ dip down with each major volcanic eruption within the AOD record (see Fig. 11 in the Discussion, Section 4). These volcanic dips are far more pronounced for the GMST component than for OHCA (Fig. 3) and are present only as flat spots in the deep ocean Conservative Temperature curve (Supp. Fig. 11).

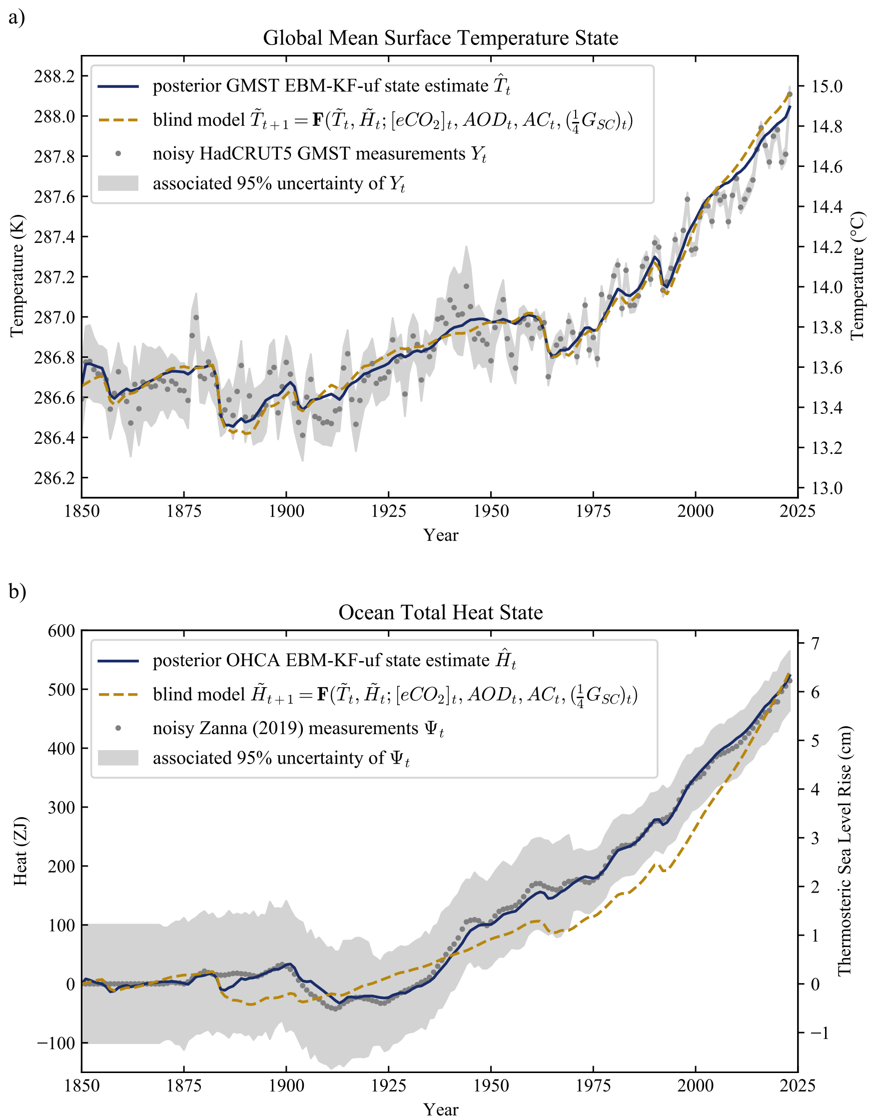


FIG. 3. Behavior of the EBM-KF-uf state in relation to blind EBM projections and the stochastic measurements of GMST and OHCA. Panel a) shows GMST prediction and b) the OHCA prediction. The blind model (dashed orange) and Kalman Filter state estimate (navy blue) use EBM dynamics to project from the previous state to the current state, but the state estimate also assimilates observations with uncertainty weighting (grey dots; GMST from HadCRUT5 (Morice et al. 2021) and OHCA from Zanna et al. (2019)). Incorporation of these observations makes only small modifications to the EBM-KF's GMST state in a), whereas in b) there is an impressive difference between the blind EBM's OHCA projections and the EBM-KF's OHCA state - the latter sticks close to observations.

### *c. Selection of Model Uncertainty and Time-Varying Measurement Uncertainty*

Fig. 3 also demonstrates the accuracy associated with each of the temperature measurements. The uncertainty in the climate state $\mathbf{P}_t$ automatically responds to unexpected values of the measured temperature (Wunsch 2020). The HadCRUT5 GMST decreases in reported measurement standard deviation from 0.079K in the 1850-1879 window to 0.017K in the 1990-2019 window (Morice et al. 2021), a 78% reduction primarily reflecting a lack of observations in the Southern hemisphere before the satellite age. The inferred deep ocean heat content taken primarily from a hybrid model-observation reconstruction (Zanna et al. 2019) has a very wide confidence interval before the introduction of modern sampling methods in the 1970s. We use the Zanna et al. (2019) hybrid product due to its long record of OHCA estimates (based on surface forcing in early years) rather than the shorter direct measurement products (Ishii et al. 2017), although both could be assimilated simultaneously within EBM-KF if desired (as discussed in Section 4c). The additional increase in OHCA after 2018 was provided from a separate NCEI dataset (Levitus et al. 2017). Our EBM-KF incorporates these known physical measurement uncertainties in the HadCRUT5 measurements of GMST and the OHCA reconstruction as $\mathbf{R}_t^{var}$. The total assumed measurement covariance $\mathbf{R}_t$ (14) is composed of two components: the time-varying physical measurement uncertainty $\mathbf{R}_t^{var}$, and the constant uncertainty $\mathbf{R}^{const}$ reflecting internal variability due to dynamical chaos: primarily ENSO and other climate oscillations with limited predictability. Both forms of measurement noise are added onto the underlying climate signal via the random vector $v_t$ to generate annual observations (9b). We assume that $\mathbf{R}_t^{var}$ is diagonal and simply sum the two variance matrices to obtain a time-varying value:

$$\mathbf{R}_t = \mathbf{R}_t^{var} + \mathbf{R}^{const} \tag{21}$$

Both realizations of our EBM-KF also have a measurement uncertainty $\mathbf{R}^{const}$ that is constant in time and based on the [HadCRUT5's GMST, Zanna et al. (2019) OHCA] residual co-variance with respect to their 30-year running means. In other words, we computed:

$$\mathbf{R}^{const} = \mathrm{Cov}(\ \mathbf{y}_t - \overline{{}_{30}\mathbf{y}_t}\ ) = \begin{bmatrix} 0.01099\ K^2 & 0.04523\ K\ \frac{W\ year}{m^2} \\ 0.04523 K \frac{W\ year}{m^2} & 1.12991\ \left(\frac{W\ year}{m^2}\right)^2 \end{bmatrix} = 30 \cdot \mathbf{Q} \tag{22}$$

The assumed model covariance, $\mathbf{Q}$ used in (12), is set to $\mathbf{R}^{const}/30$ to emulate the 30-year running average definition of climate state (Guttman 1989). That is, we assume that the random noise contained within the climate model has a variance that is 1/30$^{\text{th}}$ as large as the variance in the "weather" measurements and assume yearly anomalies are uncorrelated. By this simple method, the data-assimilating EBM-KF is tuned to match the "standard climate normal", as any 30-member uncorrelated sample average has a variance 1/30$^{\text{th}}$ as large as the annual measurements' variance. Variance in these annual measurements arises both from chaos within the climate system and measurement uncertainty, this $\mathbf{R}^{const}$ contribution to the model and measurement uncertainty quantifies the chaotic internal variability and would exist even if all measurements could be made with arbitrary accuracy.

### *d. Non-Gaussian Future Projection and Sampling of Volcanic Activity*

The EBM-KF can project one year into the future, given greenhouse gas and aerosol concentrations, without any new measurements using only the forward model to obtain *forecast* estimates (11)-(12). To project farther into the future, the *posterior* state and *posterior* covariance are set equal to the *forecast* state and *forecast* covariance, i.e., a *posterior* unaffected by any new observations: $\hat{\mathbf{x}}_t = \mathbf{F}(\hat{\mathbf{x}}_{t-1})$ and $\mathbf{P}_t = \mathbf{\Phi}_t \mathbf{P}_{t-1} \mathbf{\Phi}_t^* + \mathbf{Q}$. While these far-future state estimates behave equivalently to a blind model, the covariance grows over time, either sub-linearly or exponentially (see Section 3d).

While the SSPs are used for most forcing variables, future volcanic eruptions require modeling as well. Volcanic eruptions determining $AOD_t$ are inherently stochastic, but the time intervals between eruptions can be approximated using exponential distributions (Papale 2018). In standard ESM SSP forcing, future volcanism is usually included by a steady "background" volcanism, neglecting volcanism's intermittency and the associated exponential distributions. Even though the EBM-KF assumes Gaussian error and thus cannot include exponential distributions in the same way as measurement and internal chaotic variability, it is so computationally inexpensive that it can be rerun to sample repeatedly over non-Gaussian distributions. This ability to include future volcanoes illustrates a major advantage of this system: thousands of future scenario inputs can be generated and utilized within minutes on a laptop, while each ESM of the LENS2 ensemble took over a week to run on a supercomputer (roughly a billion times more effort in core-hours per ensemble member) which limits the ensemble size and thus motivates using only a background constant level of volcanism. No single exponential distribution fits well to the observed series of volcano eruption intervals, so an exponential mixture with two components was found to be the best fit to the data using the decomposed normalized maximum likelihood (Okada et al. 2020). See Appendix B for further details.

## 3. Results

### *a. Examination of the EBM-KF Climate State (1850-Present)*

A primary product of this paper is the EBM-KF-uf climate state, spanning from 1850 to present. Recall that the forward EBM uses published literature values: this is not an empirical fit to GMST and OHCA data, but rather the EBM-KF (in all variants) assimilates these data. We first examine the GMST component $\hat{T}_t$ of the Kalman-Filtered climate state $\hat{\mathbf{x}}_t$. There are two distinct Gaussian distributions relevant to understanding our method: the uncertainty in the current GMST *climate state* $T_t \pm 2\sqrt{\hat{p}_t^T}$, as graphed in narrow green envelope in Fig. 4a, and the uncertainty window of possible next-year (*forecast*) GMST measurements $T_{t|t-1} \pm 2\sqrt{\hat{s}_t^T}$, as graphed in the light blue wider envelope in Fig. 4a.

Further examination of the "*update*" difference (16) between the posterior estimated states and forecast states $\hat{T}_t - \hat{T}_{t|t-1}$ reveals that in any individual year after 1855, assimilation of the GMST measurement only shifts the forecast GMST state projection $\hat{T}_{t|t-1}$ by -0.001±0.009 K year$^{-1}$ (± standard deviation), range [-0.020 — 0.022] K year$^{-1}$. This *update* value is miniscule compared with the GMST adjustment in $\tilde{T}_t$ from the blind, forward EBM contribution of forced climate state change of +0.025±0.027 K year$^{-1}$ since 1975, and +0.002±0.027 K year$^{-1}$ from 1850 to 1975, while the forecast change can be as large as [-0.191 — 0.053] K in a single year. However, as shown in Fig. 3, repeated small *updates* in the same direction (due to repeatedly lower or higher than expected GMST measurements) can drift $\hat{T}_t$ away from the blind model estimate $\tilde{T}_t$. This "*accumulated correction*" ($\hat{T}_t - \tilde{T}_t$) is +0.004K on average, and as much as [-0.086 — 0.096]K (after 1885: +0.02K range [-0.086 — 0.062] K). Accumulated corrections are 3-4 times larger in extreme than the most extreme updates, indicating that these updates had accumulated over >4 years prior to 1886 and 2022 (5 and 8 years respectively, see Fig. 3a). Note the mean accumulated

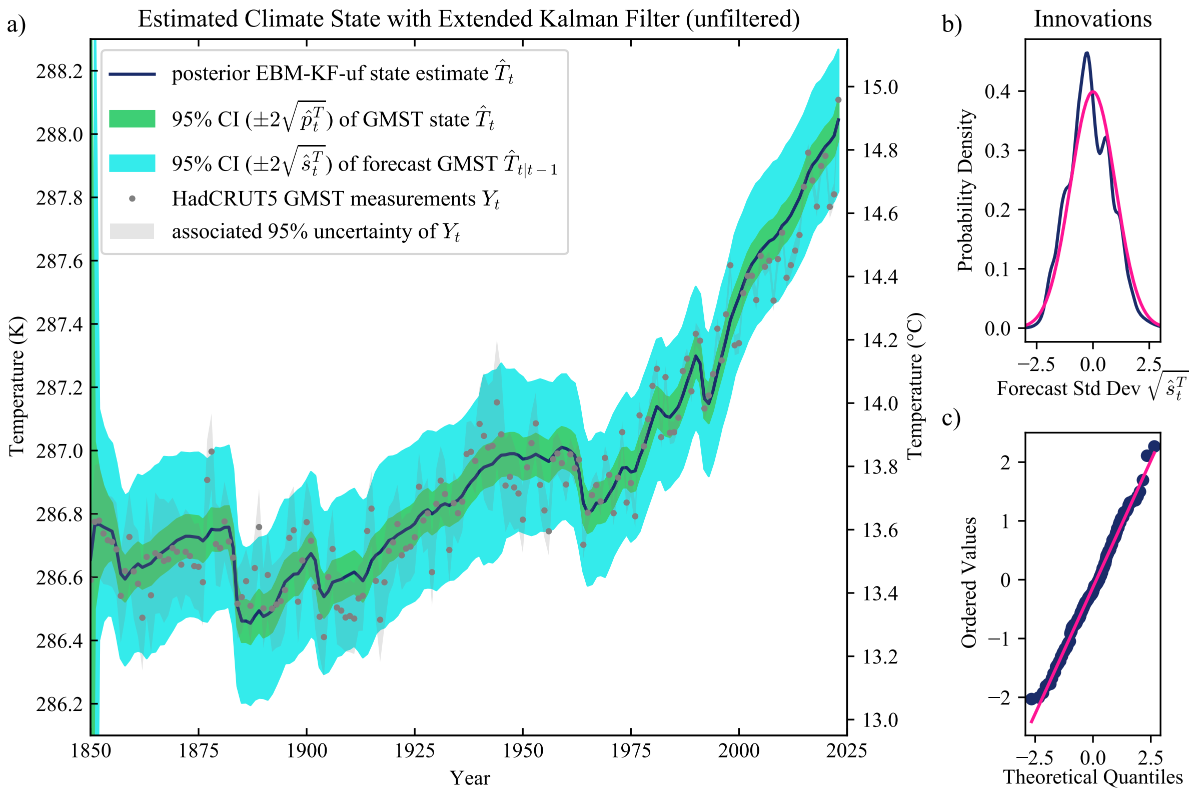


FIG. 4. EBM-KF-uf and associated uncertainties. a) The EBM-KF-uf climate state estimate (navy blue line $\hat{T}_t$) is drawn with a 95% or *extremely likely* confidence interval (light green area) of its posterior uncertainty $\pm 2\sqrt{\hat{p}_t^T}$. Annual-mean HadCRUT5 GMST measurements are assimilated (gray dots and gray area mostly within the light blue). A 95% confidence interval (CI) in light blue indicates the forecast uncertainty $\pm 2\sqrt{\hat{s}_t^T}$. b) The Gaussian mixture of innovations $z_t^T$ (deviations between measurements minus $Y_t$ the projected climate state $\hat{T}_{t|t-1}$) with each year's associated measurement uncertainty (navy blue), normalized onto a horizontal axis labeled with standard deviations $\sqrt{\hat{s}_t^T}$ of the ideal forecast covariance (pink). c) Quantile-quantile plot of these normalized innovations ($z_t^T$ / $\sqrt{\hat{s}_t^T}$). All panels demonstrate that the gray HadCRUT5 GMST observations appropriately fill out the 95% CI of the forecast uncertainty (light blue) around the EBM-KF-uf state estimate (navy blue, $\hat{T}_t$).

correction is slightly positive while the mean update is slightly negative because of the influence of OHCA corrections (see below and Fig. 3b).

The EBM-KF-uf state $\hat{T}_t$ is still very highly correlated with the blind, forward EBM $\tilde{T}_t$ ($r^2$=0.992). Measurements $Y_t$ have nearly equal warming and cooling contributions to the underlying $\hat{T}_t$ climate state, forming the expected Gaussian distribution of normalized innovations ($z_t^T$ / $\sqrt{\hat{s}_t^T}$) as demonstrated over the entire timeseries in Fig 4b and in every full 50-year period in Supp. Fig. 12. The GMST observations since 2000 slightly cool the EBM (Supp. Fig. 12d,h) indicating that the EBM may have oversized positive climate feedbacks, an issue which could be rectified with parameter adjustment (Section 4c).

After an initial convergence period of about a decade, the green 95% CI of the GMST state uncertainty $\pm 2\sqrt{\hat{p}_t^T}$ slightly shrinks from ±0.067K in the 1870s to ±0.062 K since 1980. The 95% CI of forecast uncertainty, $\pm 2\sqrt{\hat{s}_t^T}$, is drawn in light blue around the forecast estimated GMST state projection $\hat{T}_{t|t-1}$, showing where the Kalman Filter expects the subsequent year's temperature measurement to be. This forecast uncertainty converges from roughly ±0.26K in the 1870s to ±0.223K since 1980. Both reductions reflect the improvement in the GMST component of the time-varying measurement uncertainty, $\mathbf{R}_t^{var}$, with modern observations. But these reductions are modest compared to the 76% reduction in time-varying HadCRUT5 measurement uncertainty over the same period because the EBM-KF is also assuming time-invariant levels of chaotic internal climate process uncertainty ($\mathbf{Q}$ and the associated $\mathbf{R}^{const}$).

The empirical projection probability distribution (a Gaussian mixture of all measurement uncertainties relative to the EBM-KF forecast distribution) and an ideal Gaussian distribution closely match (Fig. 3b), confirming that the annual measurements of GMST can be interpreted as Gaussian noise around an underlying climate state. The quantile-quantile plot (Fig. 3c) demonstrates this same finding, just using gray points of innovations ($z_t^T$the difference between EMB-KF forecasts $\hat{T}_{t|t-1}$ and measurements $Y_t$) rather than each innovation being a distribution (with variance from $\mathbf{R}_t^{var}$) as in Fig. 3b. Each innovation point is normalized to the forecast uncertainty ($z_t^T$ / $\sqrt{\hat{s}_t^T}$), and then these are sorted from lowest to highest and plotted on the vertical axis. Along the horizontal (theoretical quantiles) axis, the percentile of each innovation is plotted where it would lie on an ideal Gaussian distribution, showing the real GMST "weather" measurements from HadCRUT5 are distributed around the EBM-KF-uf GMST climate state in precisely the expected Gaussian distribution.

As we hoped, the EBM-KF-uf GMST climate state estimate over 1850 to present is not substantively different from the 30-year running average except for the impact of major volcanoes (see Fig. 10a, $r^2$=0.923), thus $\hat{T}_t \approx \overline{{}_{30}Y_t}$ in non-volcano years. The LENS2 hindcasts depart from both in the interval from 1940 – 2000 (see Fig. 10a) causing a lower $r^2$=0.906 over all 174 years between EBM-KF-uf and LENS2. The EBM-KF-uf with unfiltered volcanic forcing can thus be interpreted as a middle ground between the 30-year running average and a LENS2 ensemble average (which are farther apart with $r^2$=0.820). The performance of the GMST and OHCA portions of EBM-KF-uf model do vary; the most noticeable biases (see Fig. 3) are that the blind OHCA is significantly corrected toward the Zanna et al. (2019) reconstruction of OHCA from 1875-2005 (assimilation of this data reconstruction continues through 2018), but these correction periods are not evident as persistent biases in the EBM-KF (Fig. 5). Forward model biases may be ameliorated by automated, optimized tuning of parameters. This is addressed in Section 4c and is well-studied in Kalman filter applications (Zhang and Atia 2020); the potential adoption of these tools to climate science is a key advantage of the EBM-KF hybrid.

Fig. 5 shows the deep OHCA component of the EBM-KF and its associated uncertainties. While the OHCA measurements from the Zanna et al. (2019) hybrid product are more autocorrelated than the HadCRUT5 GMST (relatively less year-to-year variability), the innovations for OHCA are again approximately Gaussian (panels 5b, 5c). In the context of this empirical probability distribution, each member of the Gaussian mixture has a larger gray window given by the time-varying measurement uncertainties $\mathbf{R}_t^{var}$ from the OHCA measurements. In simpler language, the light blue forecast window is large because it must encapsulate the gray measurement uncertainty window, which moves around within it. To achieve the nearly Gaussian empirical probability distribution in panel 5b, it is unsurprising that most EBM-KF estimated states are pulled very close to the autocorrelated OHCA measurements in Figs. 5a & 3b. This is a situation dominated by measurement uncertainty $\mathbf{R}_t^{var}$, which is different than observable dynamic "weather variability" (innovations $z_t^T$) filling the full forecast distribution (light blue) in Fig. 4a. As a result, the OHCA component of the EBM-KF pays much more attention to these measurements $\psi_t$ than relying mostly on the blind EBM (see Fig. 3b). This updates the OHCA state estimate ($\hat{H}_t - \hat{H}_{t|t-1}$) after 1855 by 0.05±3.72 ZJ year$^{-1}$, range [-8.16 — 9.78] ZJ year$^{-1}$; comparable with the OHCA change in $\tilde{H}_t$ from the blind, forward EBM contribution 3.07±5.30 ZJ year$^{-1}$, up to [-25.31 — 14.72] ZJ year$^{-1}$.

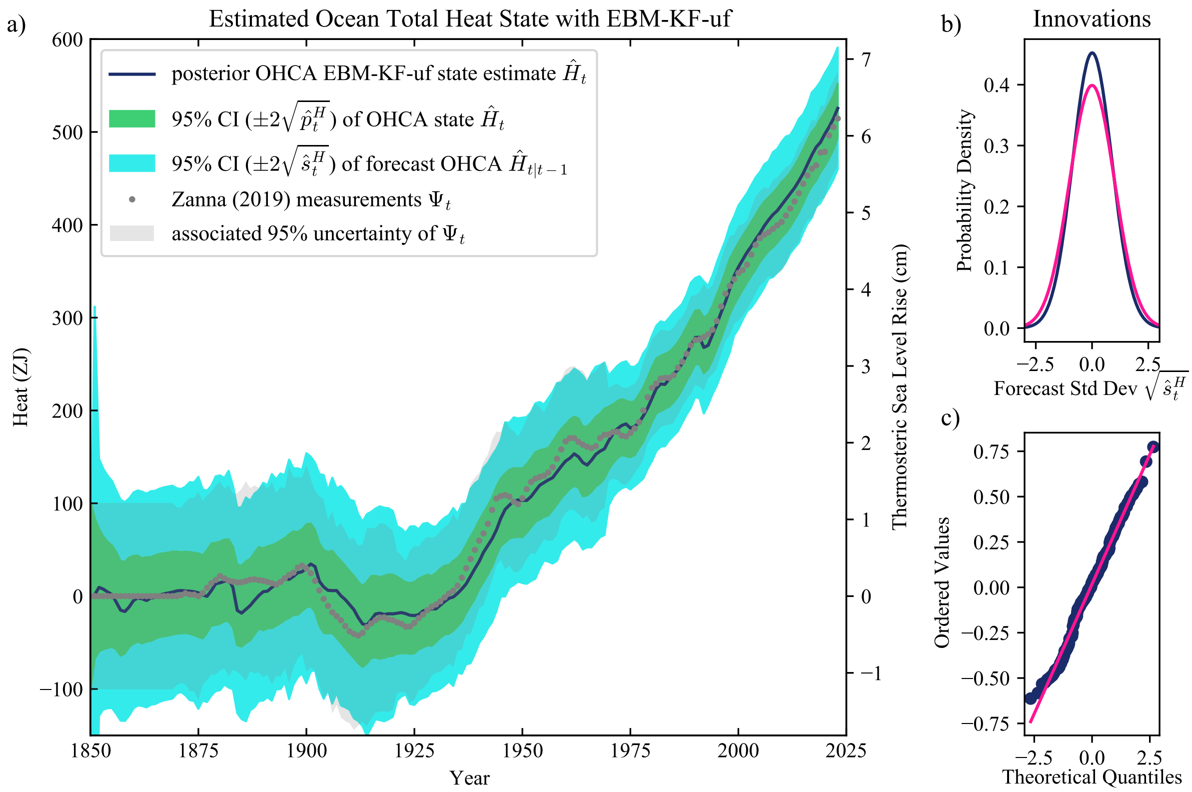


FIG. 5. EBM-KF state estimate (navy blue) for deep ocean OHCA in zettajoules and approximate thermosteric sea level from the same EBM-KF run as in Fig. 3. 95% CI of forecast estimate is drawn in light blue, and posterior 95% CI is drawn in green. Annual-mean Zanna et al. (2019) reconstructions are assimilated (gray dots and gray area almost entirely within the light blue). Other panels and colors as in Fig. 4. All panels demonstrate that the uncertainty window of the assimilated OHCA data (gray) closely corresponds to the 95% CI of the forecast uncertainty (light blue) around the EBM-KF state estimate (navy blue).

Unsurprisingly, the EBM-KF takes a substantially different track than the blind EBM, yielding an accumulated correction of up to +91.6 ZJ in 1998. Reflecting this improvement in measurement accuracy (as incorporated via $\mathbf{R}_t^{var}$), the OHCA components of both state uncertainty $2\sqrt{\hat{p}_t^H}$ and forecast uncertainty $2\sqrt{\hat{s}_t^H}$ shrink dramatically over the 174-year run. $2\sqrt{\hat{p}_t^H}$, the envelope for the OHCA climate state estimate, has a very slow initial convergence that reaches ±45.1 ZJ by 1865 and then gradually falls to ±29.4 ZJ by 2000, a 35% decrease. $\pm 2\sqrt{\hat{s}_t^H}$, the 95% forecast envelope for OHCA, drops from ±115.0 ZJ by 1865 to ±66.2 ZJ by 1970 (42% decrease) and then remains near this value through the present, range [±63.4 — ±71.2]. This reduction in forecast uncertainty directly reflects a 48% decrease in the uncertainty from the Zanna et al. (2019) hybrid product over the equivalent time period.

### *b. Using the EBM-KF to determine Policy Threshold Crossing*

A single GMST measurement is not an accurate measurement of anthropogenic climate change due to the large internal variability of the system, and so a single annual temperature above a particular policy threshold is not a guarantee of the climate state crossing that threshold. One interpretation of "crossing" is when the climate state underlying GMST (e.g. the "standard climate normal", or 30-year running mean of GMST) is determined with a given probability to have passed a policy threshold. This "climate state above" the threshold definition was used by Tebaldi and Knutti (2018) for regional thresholds and the IPCC AR6 (Lee et al. 2021) who state "the time of GSAT exceedance is determined as the first year at which 21-year running averages of GSAT exceed the given policy threshold."[5] A second interpretation would be the chance that next year's annual-mean GMST will exceed the policy threshold, or "annual temperature forecast above" the threshold. The EBM-KF generates probability distributions for both the "climate state above" and the "annual temperature forecast above" interpretations of whether a policy threshold has been crossed.

For the first interpretation, the climate state threshold as in the IPCC definition, is given in the EBM-KF by a Gaussian distribution (green in Fig. 6a) about the state $\hat{T}_t$ with a variance $\hat{p}_t^T$. The IPCC probability distribution is drawn from an ensemble of models over both the historical period and future projections (including those from LENS2 in Fig. 6b), so the fraction of the climate states (21-year means in the IPCC definition) of each ($j$) of the ensemble members $(\,_{21}\overline{Y_t}\,)_j$ found above a given policy threshold determines the overall probability that the climate policy threshold was crossed (see Fig. 6d). Within our notation, we reuse $Y_t$ to represent a GMST timeseries, but also add the $j$ subscript to indicate the $j^{\text{th}}$ LENS2 hindcast (a simulation of 90), to distinguish an ensemble member from an observed historical record. This empirical approach assumes the

[5]We use a 30-year averaging window nearly everywhere, but for consistency with IPCC practices only in Fig. 6b and Fig 12a-e we use a 21-year averaging window for raw ESM simulations. The EBM-KF climate state covariance is still chosen to reflect the uncertainty in the 30-year average of real-world GMST (see Section 2c) using $\mathbf{R}^{const}$ and $\mathbf{Q}$ matrices reflecting the 21-year means to match the IPCC definition would be a trivial modification.

ensemble spread is a good representation of the real world GMST uncertainty. However, caution with this assumption is needed as recent IPCC reports discount the 90% ensemble spread to a 66% confidence range because coarse climate models under-represent internal variability and model uncertainty (Collins et al. 2013; Lee et al. 2021). The EBM-KF (all variants) does not require a future projection to arrive at a present-day climate state, because it already provides an instantaneous and continual estimate of $\hat{T}_t$. The uncertainty $2\sqrt{\hat{p}_t^T}$ around the *posterior* climate state $\hat{T}_t$ is used to calculate the probability of threshold crossing (see Fig. 6a) as follows: The probability of the climate state exceeding the policy threshold $q$ is the integral of the probability density of the GMST climate state above $q$, equivalently 1 minus the integrated probability below $q$. The Gaussian cumulative distribution function centered at $\hat{T}_t$ with variance set to $\hat{p}_t^T$, evaluated at $q$, is this cumulative probability below the threshold:

$$\mathbb{P}\left(\hat{T}_t \geq q\right) = 1 - \text{ CDF}_{\mathcal{N}(\hat{T}_t, \hat{p}_t^T)}(q) = \frac{1}{2}\left(1 + \text{erf}\left((\hat{T}_t \ - \ q)/\sqrt{2\hat{p}_t^T}\right)\right) \tag{23}$$

For the second interpretation, temperature forecast above the policy threshold, the EBM-KF-uf predicts a relevant window (blue in Fig. 6c) of possible next-year GMST measurements. This EBM-KF window is a Gaussian distribution centered at the projected state $\hat{T}_{t|t-1}$ (dashed dark blue line) with a variance $\hat{s}_t^T$: in other words, a simulated draw from the *forecast* state. This uncertainty range reflects and encapsulates actual annual GMST measurements, not the uncertainty in the climate. For LENS2, an ensemble of ESMs, the analogous temperature forecast probability is the fraction of unfiltered individual ensemble members $(Y_t)_j$ at year $t$ that are warmer than the policy threshold (blue lines in Fig. 6d).

There is additional ambiguity regarding whether "crossing a policy threshold" should specify an instant or a brief period. Here we define (based on the $1\sigma$ confidence interval, or the *likely* range in IPCC calibrated language) the *likely* "policy threshold crossing period" to span from the earliest year when 15.9% of climate states or temperature forecasts exceed the policy threshold to the latest year when 84.1% of climate states or temperature forecasts exceed that policy threshold. A "policy threshold crossing instant" is the year when the probability of exceeding the policy threshold is nearest to 50% while continuing to increase (or *as likely as not* to have crossed the policy threshold in IPCC calibrated language).

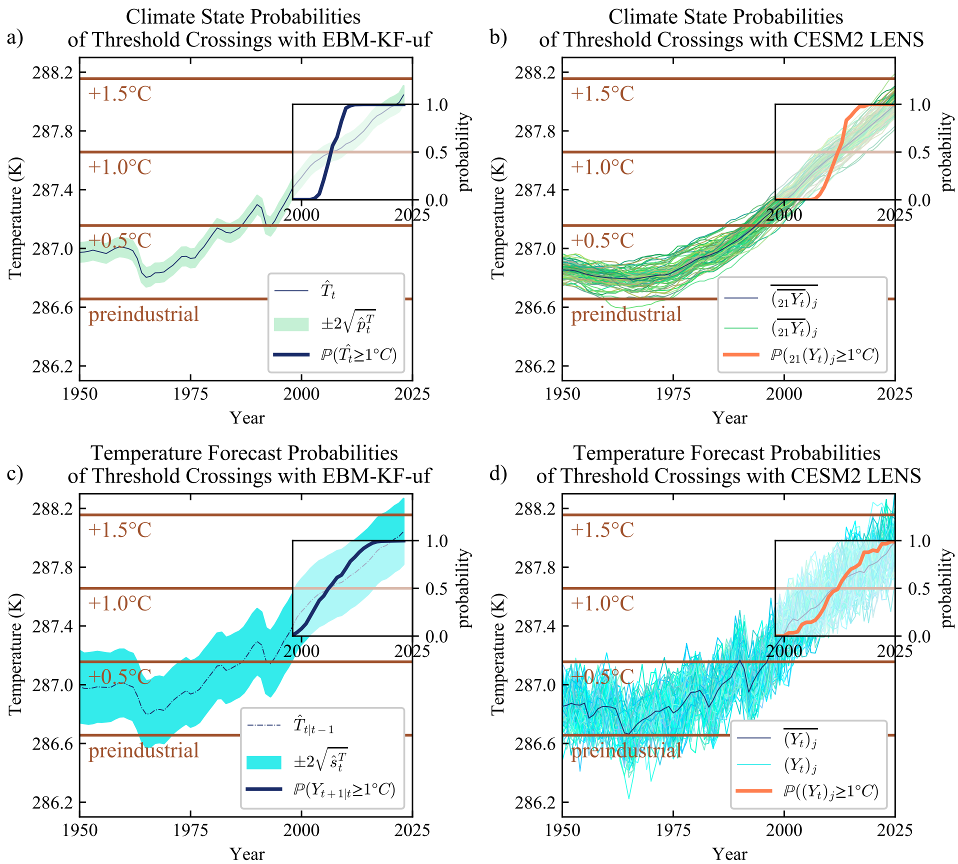


FIG. 6. a) Climate state crossing policy thresholds: As in Fig. 4, the EBM-KF-uf GMST state estimate (navy blue line) $\hat{T}_t$ and 95% CI of this estimate (light green) $\pm 2\sqrt{\hat{p}_t^T}$ is shown. Policy thresholds (brown lines) are shown at +0, +0.5, and +1.0°C relative to the preindustrial baseline. The inset axis indicates the +1°C threshold crossing probability (thick navy blue; from 0 to 1). b) 21-year running mean of each LENS2 member is plotted in green $(\overline{_{21}Y_t})_j$, along with the ensemble-average in black $\overline{(\overline{_{21}Y_t})_j}$. The inset axis shows the fraction of these running means above the +1°C policy threshold. c) Temperature forecasts: The projected GMST "weather" 95% CI: $\pm 2\sqrt{\hat{s}_t^T}$ is shown in light blue around the forecast EBM-KF-uf GMST state estimate (navy blue dashed-dotted line) $\hat{T}_{t|t-1}$. The inset axis indicates the prior likelihood that a GMST measurement will be above the +1°C) (purple; from 0 to 1). d) Each LENS2 ensemble members is plotted as a blue or green line $(Y_t)_j$ along with the ensemble-average in dark blue $\overline{(Y_t)_j}$. The inset axis shows the fraction of these members with annual GMST above the +1°C .

Regardless of whether an ESM ensemble (see Fig. 6b,d) or EBM-KF-uf (see Fig. 6a,c) is used, the temperature forecast above threshold period (Fig. 6c,d) has a longer duration than the climate state above period (Fig. 6a,b) because the uncertainty/ensemble spread in the annual forecasts is wider than the uncertainty/ensemble spread of the time-averaged states. Both the ESM ensemble (LENS2) and EBM-KF-uf methods report similar policy threshold crossing instants (Fig. 11). Interestingly, the Mt. Pinatubo eruption in 1991 resets the +0.5K threshold crossing repeatedly in both the EBM-KF-uf and raw ESM ensemble (LENS2) by elevated volcanic emissions. As shown below in Fig. 10, the EBM-KF-ta only crosses this threshold once, much like the 21-year running means of LENS2 (Fig. 6b).

Fig. 6 quantifies the probability of crossing policy thresholds as a function of time (dark blue or orange), inset on top of the relevant GMST timeseries and spread. The EBM-KF climate state estimate in Fig. 6a and annual temperature forecast in Fig. 6c are aligned by year, although these two quantities are in entirely different probability domains. As the EBM-KF state estimate approaches any given policy threshold, the cumulative temperature policy threshold approaches 0.5, or 50% at a "policy threshold crossing instant". The +1.0K policy threshold's crossing instant was in 2010. For the annual temperature forecast in Fig. 6c, the *likely* crossing period was 2003-2015 for +1.0K. The *likely* crossing period for the climate state in Fig. 6a is briefer: 2008-2012 for +1.0K. For comparison using LENS2 the analogous climate state thresholds are plotted in Fig. 6b,d, although these do not precisely align temporally due to the cold bias of LENS2 during this decade. All threshold crossing periods and instants including future projections under SSP3-7.0 are compared directly in Fig. 12.

### *c. The spread from one member: using EBM-KF to generate an analog for an ESM large ensemble spread*

There are many more past and future climate scenarios that researchers wish to investigate than there are computational resources to run a full large ensemble for each scenario. Fortunately, the EBM-KF can project the climate state distribution when assimilating only one or a handful of ESM simulations, reducing the need for simulating an entire ensemble just to estimate its GSAT spread (similar to approaches for emulation of ensembles of ice sheet models in Edwards et al. 2021; van Katwyk et al. 2023). Of course, there are inter-annual differences which persist between runs of the ensemble and skew some climate states persistently cooler and others warmer (Supp. Fig. 6), and an ESM ensemble provides regional information, these effects are not captured by a Kalman filter framework.

Figure 7a shows the comparison between the EBM-KF-uf GMST climate state uncertainty distribution (light green) and the LENS2 Kalman-filtered ensemble members. This Kalman-filtering was performed using the same EBM-KF, momentarily assuming that one of the ensemble members' hindcast was the actual measured temperature record. Each of the orange lines is a climate state central estimate that is comparable to the blue line of the real observed GMST climate state. Sometimes the (observation-corrected) EBM-KF-uf climate state uncertainty distribution contains the Kalman-filtered LENS2 ensemble members, such as in 1900 and 1935, but at other times it does not, such as in 1950. In corresponding panels within Supp. Fig. 14, we show the histogram (Supp. Fig. 14a) and quantile-quantile comparison (Supp. Fig. 14b) which both demonstrate a clear bias. This bias indicates that the LENS2 climate state disagrees with the observed climate state within the EBM-KF framework.

We could interpret the Kalman-filtered ensemble spread versus the climate state uncertainty distribution of one ensemble member in a similar fashion. This comparison has a different purpose, as now we are testing whether the EBM-KF can predict the spread of the Kalman-filtered LENS2 ensemble correctly, regardless of whether the LENS2 ensemble matches the observed temperatures. If so, that would indicate that from one ensemble member simulation we could effectively predict all the other ensemble members. As expected, there is a distribution of results, where some of the ensemble members are close to the center of the distribution and others are outliers.

We can statistically calculate the expected error in our predicted ensemble of Kalman-filtered LENS2 states from a single member versus the true ensemble of Kalman-filtered LENS2 states. Panel 7b shows the error in spread (standard deviation) and error in bias by repeatedly making this prediction of a distribution from single members of LENS2 and comparison to the whole Kalman-filtered LENS2 ensemble. Examining the centroid (cross symbol), this is an unbiased estimate of the distribution (as it should be). However, the ensemble of Kalman-filtered LENS2 is distributed with a standard deviation that is 1.22 times larger than the average prediction from one ensemble member. At worst, it is 1.54 times larger than any single ensemble member's estimate. Figure 7b labels two examples of where one ensemble member predicts the whole ensemble: a good fit (best quartile) is shown as a circle, and the worst fit is shown as a square. Supp. Fig. 14c,d show these two comparisons in more detail. This error in spread, as well as the distribution of biases are all better than the comparison between the LENS2 Kalman-filtered states and the observed record's EBM-KF state uncertainty (green star). From this we conclude that the error in predicted distribution from one ensemble member is negligible in comparison to the distance between the model and reality. Thus, this approach is effective in making such comparisons, with a typical bias error in single ensemble member estimate of order ±0.007K with range (-0.0265—0.0268)K.

Within panel 7c, the Kullback-Leibler divergence is utilized to evaluate the utility of using the EBM-KF state uncertainty as a prior estimate of the spread between Kalman-filtered LENS2 ensemble members. At each year, this GMST state variance $\hat{p}_t^T$ is combined in a weighted mean with the variance of a small subset of LENS2 members (shown in yellow violin plots, with a number indicating the number of members taken: $N = 1, 2, 3, \text{or } 8$). This mean adds the GMST state variance (averaged across all subset runs) to the sum of squared differences from the mean of the LENS2 subset, and then divides by the size of the subset, essentially treating $\hat{p}_t^T$ as an extra sample and taking Bessel's correction.

$$({}_{ens}\sigma_t^T)^2 = \underbrace{\frac{1}{90}\left(\sum_{j=1}^{90}\left((Y_t)_j - \overline{(Y_t)_j}\right)^2\right)}_{\text{all of LENS2}} \approx \frac{1}{N}\left(\underbrace{\frac{\sum_{j=1}^{N}(\hat{p}_t^T)_j}{N}}_{\text{from KF}} + \underbrace{\sum_{j=1}^{N}\left((Y_t)_j - \frac{1}{N}\sum_{j=1}^{N}(Y_t)_j\right)^2}_{\text{sample of LENS2}}\right) \tag{24}$$

With only one ensemble member the right hand side of (24) is equal to the Kalman Filter GMST state variance.

Taking a subset of 2 members does not improve the predicted distribution of LENS2, as there is a significant chance that two members which are close together will be selected, incorrectly shrinking the predicted ensemble spread. With 3 LENS2 members, the predicted distribution slightly improves. Without using this prior estimate (and allowing the sample variance to change over time, red violin plots), at least 8 LENS2 members are required to generate a predictive ensemble distribution that is comparable to using a single LENS2 member and the Kalman Filter $\hat{p}_t^T$ as the ensemble's variance. Panel 7c demonstrates this with 3 and 8 LENS2 members with a time-varying sample standard deviation (red: 3 or 8) again using Bessel's correction. Thus,

Fig. 7 shows the power of the parametric Gaussian statistics generated by the EBM-KF over a raw ensemble member sample estimate.

LENS2 runs are more similar to each other than to the real Earth, especially regarding outputs such as OHCA (see Supp. Fig. 13) and Arctic or Antarctic sea ice extent (Horvat 2021; Roach et al. 2020; Rosenblum and Eisenman 2017). In comparison to the observation-assimilating EBM-KF, LENS2 has a profound cold bias from 1940-2000 (max separation of LENS2 ensemble average in 1983 of 0.262°C, average absolute separation ±0.088°C, standard deviation ±0.085°C, $r^2$=0.907). Also, the current generation of ESMs tend to underestimate the appropriate full spread of climate variability. For instance, some weather models use stochastic noise to push their distribution wider than dynamic variation alone (Buizza et al. 1999), and other numerical climate models perturb parameters to achieve the same distribution-widening effect (Duffy et al. 2023; Keil et al. 2021).

In summary, Fig. 7 shows that the EBM-KF climate state based on HadCRUT5 temperatures or based any one of the LENS2 ensemble members show the expected level of consistency and (potentially biased) Gaussian differences with the rest of the LENS2 ensemble. Thus, using the EBM-KF on any one of the ensemble members does a good job of estimating the GMST climate state (i.e., averaged over internal variability) and its uncertainty as simulated by the spread of the entire LENS2 ensemble. Further comparisons between the EBM-KF, such as comparing the unfiltered ensemble spread to the forecast prior distribution, would be revealing.

### *d. Sampling Future Projections from a Non-Gaussian Volcanic Distribution*

In standard climate assessments (e.g., IPCC 2021), future volcanism has long been singled out as an unknown aspect of projected climate change in any given future year, particularly regarding tropical eruptions' contribution to planetary albedo (Marshall et al. 2022). The forcing of historical-period climate models includes the effects of known past volcanoes, while the forcing of future climate models includes only "background forcing from volcanoes", i.e., an expected average forcing value in future years. Applying an average forcing misses the potential impact of individual volcanic events on the global climate state (compare blue line to black lines in Fig. 8) and underestimates nonlinearities in the climate system. Individual volcanoes can shift crossing thresholds (as Section 3b and Fig. 12 show), and so they affect near-term decades (see Fig. 11a,b). However, running an ESM ensemble of sufficient size to explore the low probability of a volcanic

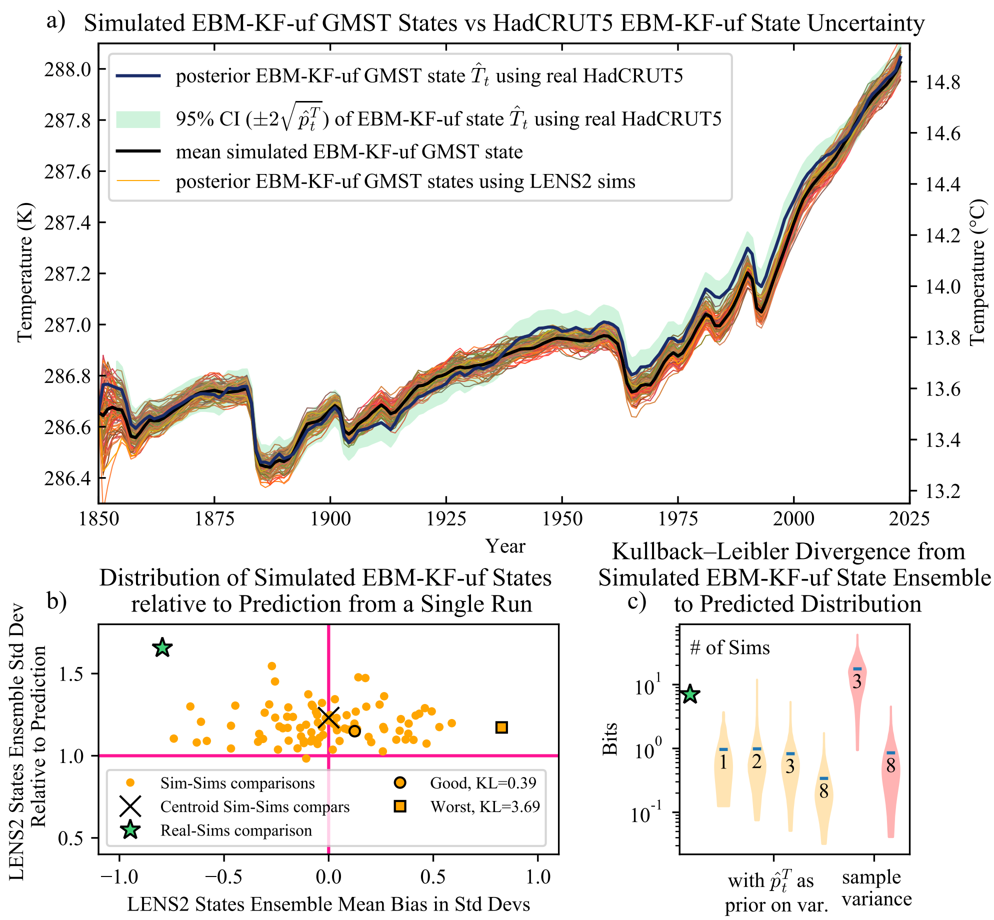


FIG. 7. Comparison of the GMST Kalman Filter states across the LENS2 ensemble. a) The EBM-KF-uf $\hat{T}_t$ from HadCRUT5 (thick blue) and its 95% CI (light green) $\pm 2\sqrt{\hat{p}_t^T}$, along with EBM-KF state estimates for each individual CESM2 ensemble member (orange lines) and their mean (thick black line). b) Climate states and associated uncertainties arising from each of 90 LENS2 simulations and HadCRUT5 are compared to all other LENS2 climate states, and the relative bias and standard deviation of the resulting empirical distributions with respect to a particular ensemble member's $\sqrt{\hat{p}_t^T}$. c) Violin plots compare the Kullback-Leibler divergence (on a log scale, smaller indicates a better match) for a variety of methods of predicting the LENS2-time-Filtered ensemble spread. In yellow, the $\hat{p}_t^T$ from 1, 2, 3, or 8 EBM-KF-uf LENS2 runs is averaged, and used in combination with the time-varying sample variance. In red, 3 or 8 of these time-Filtered ensemble members are used to predict an ensemble distribution from time-varying sample variance alone. Taking a single EBM-KF-uf LENS2 run with $\hat{p}_t^T$ approximates the time-Filtered LENS2 ensemble with similar accuracy as taking the time-varying sample variance of 8 time-Filtered ensemble members.

eruption in any potential year is computationally challenging using traditional ESMs, and has motivated specialized model intercomparison projects (Timmreck et al. 2018; Zanchettin et al. 2016). By contrast, robust sampling of rare events is easily accomplished with the inexpensive EBM-KF. For simplicity, only the volcanic AOD effect is included; the added volcanic contribution of $CO_2$ and other greenhouse gases is not, as their annual greenhouse gas contribution is miniscule compared to anthropogenic emissions: 20 times smaller in 1900, 130 times smaller in 2010 (Gerlach 2011). Slightly different climate responses have been modeled to occur when volcanic events occur at different phases of climate oscillation patterns, such as the Pacific Decadal Oscillation (PDO) and North Atlantic Oscillation (NAO) (Illing et al. 2018). Due to its low-dimensional state space and limited representation of variations about the climate state, the EBM-KF neglects such complexities.

Figs. 8 & 9 show the future projections of GMST and OHCA using EBM-KF-uf, including sampling for future volcanoes for two emission scenarios. SSP1-2.6 shown in Figs. 8a & 9a has anthropogenic $CO_2$ emissions that sharply decline after 2020 to keep GMST rise below 2K (van Vuuren et al. 2007, 2017). SSP3-7.0 shown in Figs. 8b & 9b is a higher anthropogenic emission scenario in which $CO_2$ emissions double by 2100 (Fujimori et al. 2017).

Figs. 8 & 9 show that the volcanic ensemble probability density is not symmetrical for GMST - there is a much longer tail on the cooler side because of intermittent cooling by volcanic aerosols. In Fig. 8 the cooler side of the distribution takes a few years (2024–2026) to fully expand out because large eruptions generally did not produce their maximal effect on $AOD_t$ (and thus the GMST climate state) until 1-2 years after the eruption (and no major eruptions are ongoing at present). In any single future sampled scenario of volcanic eruptions, there is usually a significant gap between major volcanic eruptions (as our model indicates by the thin black lines in Fig. 8 & 9), representing an autocorrelation (see Appendix B). These gaps are not reflected in the 95% CI (pink) which sample thousands of independent futures. Indeed, the volcanic eruptions dominate the future uncertainty over the slowly growing GMST climate state uncertainty and rival or exceed the scenario uncertainty up until about 2050 (assuming known model parameters, Fig. 11a). By contrast, the LENS2 using "constant background" future volcanism has a symmetrical distribution about the mean for future projections of the same SSPs (Supp Fig. 6, right of dashed line). The

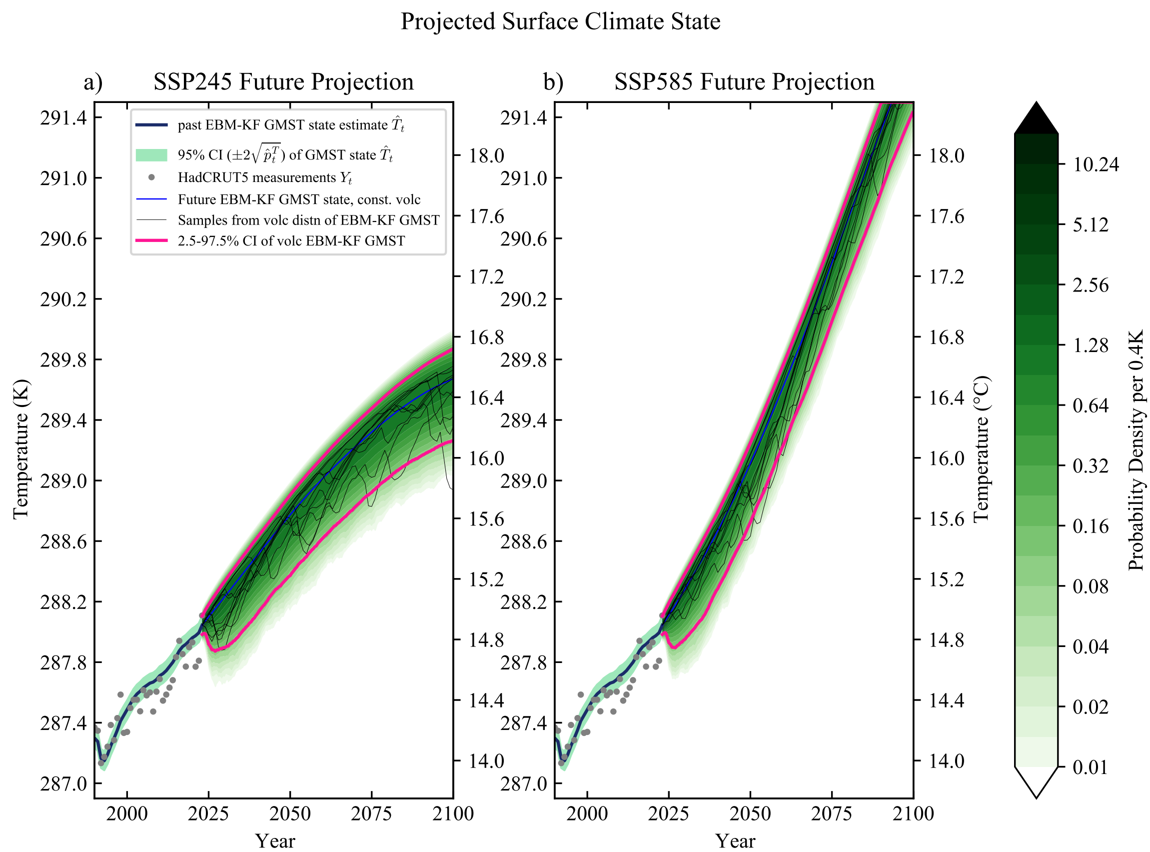


FIG. 8. Future GMST projections of SSP1-2.6 (a) and SSP3-7.0 (b) scenarios using sampled measures of volcanic activity and greenhouse gas concentrations calculated according to MAGICC7.0 (Meinshausen et al. 2020). The historical Mt. Pinatubo eruption in 1991 is shown in the lower left corner of both graphs for scale. 10 of the sampled 6000 potential future climate states from the volcanic probability distribution are graphed (thin black), along with a future climate state projection that uses constant volcanism with average $AOD_t = \overline{AOD_{1850-2024}} = 0.0123$ (blue). The probability density function formed by taking the summation of all sampled Gaussian kernels at each time point is shaded in green on a logarithmic scale (note these probability densities are not probabilities so they can exceed 1). Pink lines show the 2.5-97.5% confidence interval of these probability density functions, which are very asymmetrical (negatively skewed) due to the sampled volcanic eruptions' impact on GMST.

effects of volcanism on OHCA (Fig. 9) are much smaller than on GMST (Fig. 8), but there is still a longer tail toward the cooler, low OHCA side.

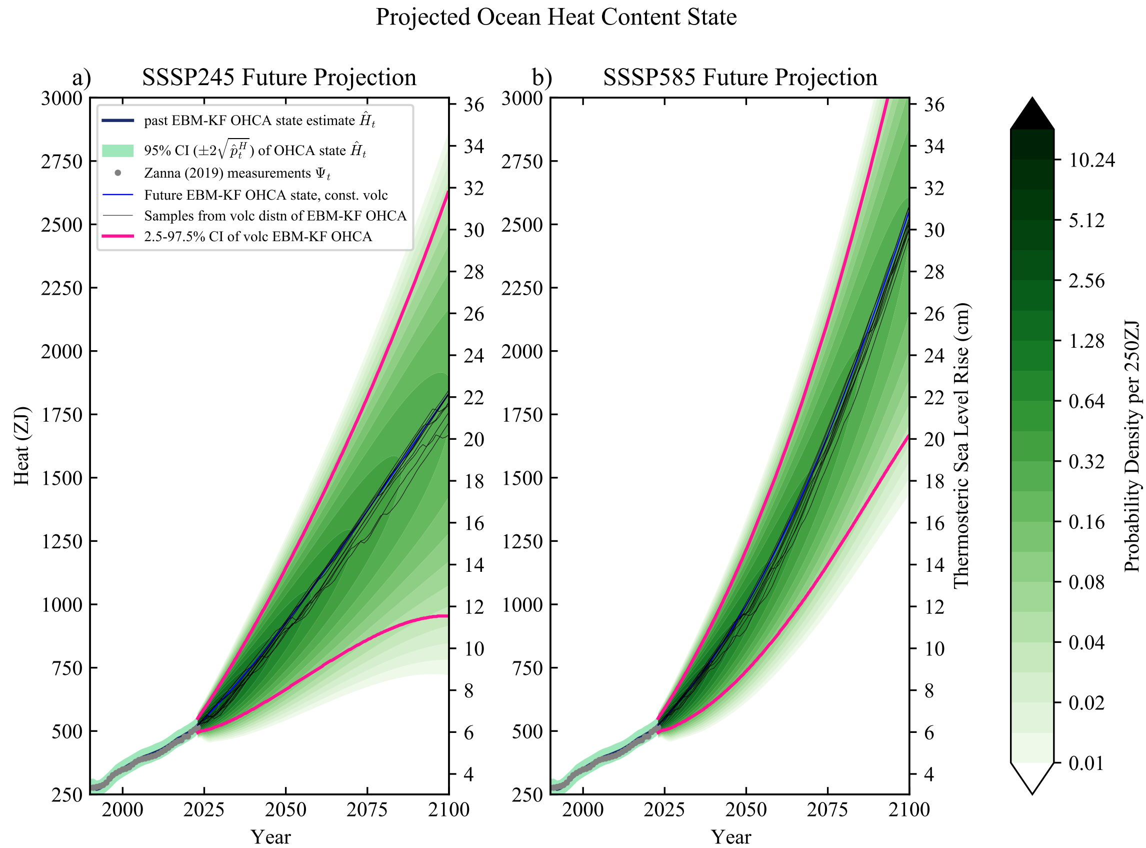


FIG. 9. Future OHCA projections of SSP1-2.6 (a) and SSP3-7.0 (b) scenarios using sampled measures of volcanic activity and greenhouse gas concentrations calculated according to MAGICC7.0 (Meinshausen et al. 2020). 10 of the sampled 6000 potential future climate states from the volcanic probability distribution are graphed (thin black), along with a future climate state projection that uses constant volcanism with average $AOD_t = \overline{AOD_{1850-2024}} = 0.0123$ (blue). The probability density function formed by taking the summation of all sampled Gaussian kernels at each time point is shaded in green on a logarithmic scale (note these probability densities are not probabilities so they can exceed 1). Pink lines show the 2.5-97.5% confidence interval of these probability density functions, which are only slightly asymmetrical because the sampled volcanic eruptions have a much smaller impact on OHCA.

Regarding future GMST policy threshold crossings, the volcanic eruptions widen the likely threshold crossing periods and lessen the difference between the “climate state above” and the “annual temperature forecast above” interpretation periods. Occasionally, major volcanic eruptions can cause a policy threshold to be "uncrossed". For example, if we were to examine one arbitrary policy threshold, 0.27°C above preindustrial, the 30-year running average GMST uncrosses this global warming policy threshold (crossing first in 1944, then dipping back under the threshold to uncross in 1956, and crossing again 1965) because the eruption of Mt. Agung reduced GMST for about a decade after its eruption in 1963. Because the 30-year running average incorporates future information, it anticipated the future eruption and started cooling in the late 1950s. The EMB-KF-uf, EBM-KF-ta, and LENS2 ensemble average similarly warm, cool, and then warm again in this period, although the cooling periods follow the causative Mt. Agung eruption (Fig. 10). In contrast, following the Mt. Pinatubo eruption in 1991, the EBM-KF-ta and the 30-year running average do not uncross the 0.5°C above preindustrial threshold, whereas the EBM-KF-uf and LENS2 ensemble average do. These distinctions are lost when using "background volcanic activity" to estimate policy threshold crossings.

Across many future simulations the dynamic model Jacobian matrix $\mathbf{\Phi}_t$ happens to remain nearly constant at values of: $\mathbf{\Phi}_t \approx \begin{bmatrix} 0.893 & 0.000253\ K/\frac{W\ yr}{m^2} \\ 11.1\ \frac{W\ yr}{m^2}/K & 0.999 \end{bmatrix}$, nearly unit triangular. Due to this Jacobian matrix shape and the 0.893 factor, $\hat{p}_t^T$ grows sub-linearly, with yearly growth less than the upper-left (GMST-exclusive) component of $\mathbf{Q}$ : $0.01099/30\ K^2 = 0.00037\ K^2$ (see Eq. 22). Over a 78-year future projection (2023-2100) the GMST state 95% confidence interval $2\sqrt{\hat{p}_t^T}$ only grows from 0.0625K to between 0.1757K and 0.1792K. This 2.8-fold increase is small over the 21st century compared to the GMST dips that occur under volcanic eruptions (see Figs. 8 & 10). The effect of volcanoes on historical state (Figs. 3 & 4) and future projections (Fig. 8) is therefore worthy of specialized treatment in addition to measurement uncertainty and internal chaotic variability (see Fig. 11 in the discussion below). In contrast, the OHCA component of the state uncertainty 95% confidence interval $2\sqrt{\hat{p}_t^H}$ grows exponentially due to the 11.1 value in the lower-left entry of $\mathbf{\Phi}_t$, and volcanoes have a negligible effect on of projected OHCA trajectories (see Fig. 9). The ocean state uncertainty 95% CI = $2\sqrt{\hat{p}_t^H}$ , initially at $2.57\frac{W\ yr}{m^2}$ (29.4 ZJ) in 2023, balloons to $76.1$—$77.1\frac{W\ yr}{m^2}$ (870—880 ZJ) by 2100.

# 4. Discussion

The EBM-KF climate state estimate resembles other standard estimates of climate state, but it has advantages they do not share. The EBM-KF algorithm, because of its relationship to a forward or "blind" EBM, can be projected forward in time without temperature observations and thus can be used in many situations. Unlike an ESM, the EBM-KF benefits from data assimilation due to its Kalman filter nature and thus remains close to observations or synthetic data (e.g., the examples in Section 4 of reproducing the LENS2 from few ensemble members). The OHCA component is particularly sensitive to assimilated observations (see Fig. 3b), largely because of reduced understanding of the ocean dynamics that drive deep ocean heat uptake compared to atmospheric radiative feedbacks. The EBM has a correspondingly simpler model of ocean physics. Unlike an Ensemble Kalman filter approach that can reweight a full-physics ESM ensemble toward observations, the EBM-KF has negligible computational cost and can thus examine rare, long-tailed events such as volcanoes. Additionally, tuning of the EBM parameters and uncertainty quantification of these results can benefit from the Kalman filter literature and algorithms to optimize our Kalman Filter parameters.

## *a. Comparison to Previous Estimation Methods of the Climate State*

Although they are different types of average, a direct comparison (Fig. 10) of the state estimated from the EBM-KF (Fig. 4) and that estimated by the 30-year running mean (Fig. 1) and the LENS2 ensemble mean (Supp. Fig. 6), the EBM-KF has slightly more year-to-year variation than the 30-year mean and less than the LENS2 ensemble mean. Departures from the main Gaussian cloud in all methods represent volcanoes. The 5 largest eruptions which caused the largest dip in EBM-KF state are labeled in Fig. 10, corresponding to the 5 peaks in $AOD_t \geq 0.06$ plotted in Fig. B1a in the appendix. The climate effects of these major tropical volcanic eruptions have been studied extensively (Jones and Kelly 1996; McCormick et al. 1995). Note for the eruptions listed, plus many others, the dips in the EBM-KF mean state correspond with dips in the sample mean of the LENS2 simulations.[6]

[6]However, the earliest AOD values provided by Sato et al. (1993) also demonstrate a major spike at 1856, which is not reflected in the LENS2 simulations. This may correspond to either the 1856 eruptions of Komaga-take, Japan or Mt. Awu, Indonesia, and we labeled this with the latter eruption and a question mark because tropical volcanic eruptions typically have a much larger climate impact (Marshall et al. 2022).

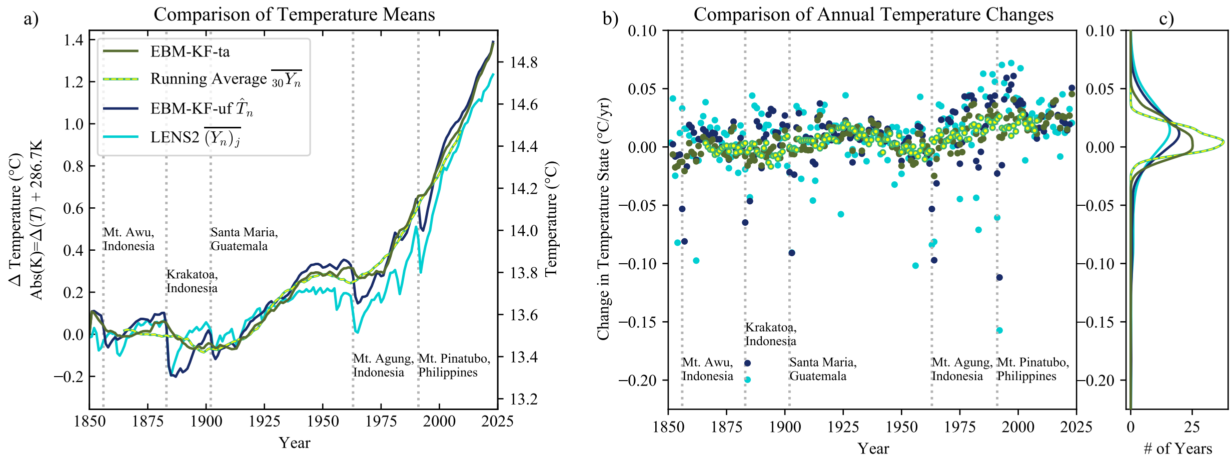


FIG. 10. GMST "climate state" comparisons. Major volcanic eruptions are labeled in both panels a and b with dotted vertical light gray lines. In all panels, the 30-year averaged GMST (yellow-green dashed) is close to the EBM-KF-ta state (dark green), whereas the EBM-KF-uf state (navy blue) resembles the ensemble mean of GSAT in the LENS2 simulations (sky blue) in responses to volcanic eruptions. a) Direct GMST temperatures of the 4 "climate states". b) The innovations (derivatives) are plotted against time. Colors are the same as in panel a. c) A smoothed empirical density with respect to yearly change in temperature is linked to panel b. (This empirical density is simply an approximation of a histogram, and the kernel densities are not provided by elements of the Kalman Filter as in Fig 4b and 5b).

Based on this interpretation of Fig. 10, we now see that the LENS2 ensemble average (light blue) is closer to the (EBM-KF-uf, navy blue, with uf abbreviating "un-filtered" AOD forcing) regarding sensitivity to volcanoes than the 30-year running mean (yellow-green). In response to this, we will distinguish two variants of $AOD_t$ forcing: one that directly uses the annual measured values of $AOD_t$ (EBM-KF-uf, navy blue, as above), and one that takes a 15-year trailing average combined in equal weight with the overall timeseries $AOD_t$ mean (EBM-KF-ta in dark green, ta abbreviating "trailing average"). This trailing average is the best point estimate for the 15-years of future $AOD_t$ and displayed as a green line in Fig. B1a. Fig. 10 shows that this trailing average preparation of the $AOD_t$ forcing brings the EBM-KF-ta (dark green) close to the 30-year running mean (yellow-green) regarding sensitivity to volcanoes. Their maximum separation was in 1962 with the 30-year running average -0.073°C cooler, otherwise their average absolute separation ±0.025°C, standard deviation ±0.030°C, $r^2$=0.986. We experimented with a centered average rather than a trailing average, and the results did not improve (not shown).

It is beyond the scope of this paper to detail the characteristics of the large and growing variety of "mean state" definitions, but a summary is useful. For all methods we have examined regarding the GMST (30-year mean – Fig. 1, 10; EBM-KF-uf – Fig. 4, 10; LENS2 model ensemble mean – Fig. 10, Supp. Fig. 6; purely statistical methods – Supp. Fig. 4c, 4d, 5; EBM-KF-ta – Fig. 10), the differences in the estimated climate state are relatively small in available years (on the order of 0.1K – see Supp. Fig. 7, column 1). The largest differences seen between these methods lie in the spread of the changes from year to year (see Supp. Fig. 7, column 2) which can be addressed by preparations filtering the forcing and persistent mean anomalies relative to observations, particularly concerning volcanism and by addressing biases in the forward, blind LENS2 ensemble (see Supp. Fig. 7, column 4).

The different variants of the EBM-KF forcing preparations apply to different intended applications. When we are trying to directly match the behavior of ensembles such as LENS2 (light blue), the EBM-KF-uf (navy blue) is the correct choice. As noted in Section 3a, LENS2 versus EBM-KF-uf is useful for examining biases in LENS2, and in Fig. 10b we see their responses to volcanic events are very similar. When we are trying to emulate 30-year climate normal (up to the present), then the EBM-KF-ta is the best estimator based only on information available before present. When we are trying to project both the weather and climate state without bias, for next-year predictions and beyond (so $AOD_t$ will be unavailable), then the optimal method is to run many predictions using EBM-KF-uf and a volcanic probability distribution, as in section 4d.

For policy thresholds, it is important to actually sample across volcanic probability distributions rather than use a background volcanism, as all climate state estimates are capable of 'uncrossing' a threshold directly because of a volcanic eruption. The EBM-KF-uf and LENS2 are just more sensitive to such eruptions than the EBM-KF-ta and 30-year running mean. Section 4d notes that Mt. Agung caused all four climate state estimates to uncross the 0.27°C threshold, while Mt. Pinatubo caused only the EBM-KF-uf and LENS2 climate state estimates to uncross the 0.5°C threshold. Similarly, future eruptions may cause a policy threshold to be uncrossed, and only sampling the volcanic probabiliites anticipates the odds of such uncrossings.

The primary distinction of our EBM-KF method and all existing alternative definitions is the integrated quantification of uncertainty. While many methods exhibit a relationship between the "mean state" and "sample" that varies in time, the EBM-KF quickly converges to a stable GMST state uncertainty of 0.034°C. The RTS filter (Supp. Fig. 2) has a narrower 0.023°C uncertainty, but involves past and future information in a given year as does the 30-year climate normal. Our choice of method was motivated by the mathematical compatibility between the governing equation for a Kalman filter and that of an EBM, which is not true of many alternatives, e.g., a Butterworth filter or Bayesian changepoint analysis or a more complex dynamical model such as an ESM. We also emphasize again that our EBM-KF infers the climate state directly via yearly signal processing, which is faster and less complex than simulating future weather over the next 15 years calculating many 30-year means. In the next section we discuss how the EBM-KF uncertainties compare to those of ESM ensembles.

### *b. Comparison to Earth System Models (CESM2 Large Ensemble and CMIP5)*

The chief advantages of EBM-KF over an ensemble of ESMs is that it replicates many statistical features while being trivial to compute. Fig. 7 suggested that any of the ensemble members or the observed temperature record could be used together with EBM-KF to recreate the climate state, but now we examine if we can anticipate or improve on the ensemble statistics *without a single ensemble member*.

First, we examine the basic statistical character of LENS2. The distribution of annual differences of all ESM trajectories from the ensemble mean are remarkably close to Gaussian (see Supp. Fig. 10a). Therefore, again due to the Central Limit Theorem, this fundamental assumption of the EBM-KF is also met by GSAT as simulated by the CESM2. The standard deviation rises insignificantly with time in LENS2 over the entire simulation duration (p=0.168). Before 2065 this rise is significant ($p=1.2\cdot10^{-6}$, see Supp. Fig. 10b) while relatively small (linear trend $r^2$=0.105 and only 8.9% rise in ${}_{ens}\sigma_t^T$ from 1850–2065). The time-averaged standard deviation 0.127K was close to both chosen total GMST-exclusive (top-left) measurement noise from $\mathbf{R}_t$ (range 0.107—0.136K, see section 2c, Eq. 21) and half the converged values in the EBM-KF of $\sqrt{\hat{s}_t^T}$: 0.13K in 1865, later 0.112K in 2000. Examining skewness and kurtosis, the uncertainty in climate as indicated by the distribution of simulations about the LENS2 GSAT ensemble mean is not meaningfully altered as the climate warms (see Supp. Fig. 10c,d).

Next, we evaluate how well the LENS2 captures the overall shape of the observed HadCRUT5 temperatures, given that it is not constrained directly by these observations. The absolute temperature of the LENS2 runs had to be revised down by a full 1.75K to match its ensemble 1850-1949 100-year average GMST to HadCRUT5. Other authors have also noted this high absolute temperature as well as the high climate sensitivity of CESM2, the model used in LENS2 (Feng et al. 2020; Gettelman et al. 2019; Zhu et al. 2022). Recall HadCRUT5 was recalibrated to a 1960-1989 30-year climate normal (Jones and Harpham 2013) of 13.85°C (287.00K), and the LENS2 average has a slightly lower temperature during this 30-year climate normal of 13.71°C (286.86K).

Comparing the EBM-KF projections (Fig. 8) with LENS2 projections (Supp. Fig. 6) both Fig. 8b and Supp. Fig. 6 trace out roughly the same shape, as both are forced by warming SSP projections. The largely symmetric uncertainty in the LENS2 about the ensemble mean is driven by dynamical instability. This is fundamentally different from the EBM-KF, which in addition to scaled, data-driven weather dynamical uncertainty also samples a noisy distribution of volcanic eruptions, yielding an asymmetrical distribution. LENS2 projections based on SSP3-7.0 achieve a slightly higher mean temperature in 2100 (291.3K, +4.6K warming) than the equivalent EBM-KF projection (290.9K, +4.2K warming, see Fig. 8b), despite the LENS2 simulations being cooler throughout most of the 20$^{th}$ century and early 21$^{st}$ century (see Fig. 10a). Across all CMIP6 models (Lee et al. 2021; Tebaldi et al. 2021) the projected warming under this scenario is 3.9K with 5-95% range (+2.8K, +5.5K), closer to the EBM-KF projection.

Continuing beyond LENS2 to compare against the multi-model CMIP6 ensemble, a projected uncertainty decomposition is created following Hawkins and Sutton (2009) and Lehner et al. (2020) in Fig. 11. In their adopted uncertainty decomposition method, ESMs are smoothed with 4$^{th}$-degree polynomials, but here we show 95% CI and annual (rather than decadal) internal variability. By our methods in Section 4c, the EBM-KF adds the new entry of volcanic emissions uncertainty into this picture (Fig. 11a&c, pink). A second advantage is that the climate state uncertainty (due to the cumulative reliability of measurements with respect to a model, green) and the model uncertainty (due to the confidence in the model structure and parameters, blue) can be distinguished whereas in CMIP6 they are combined because they are calculated together from

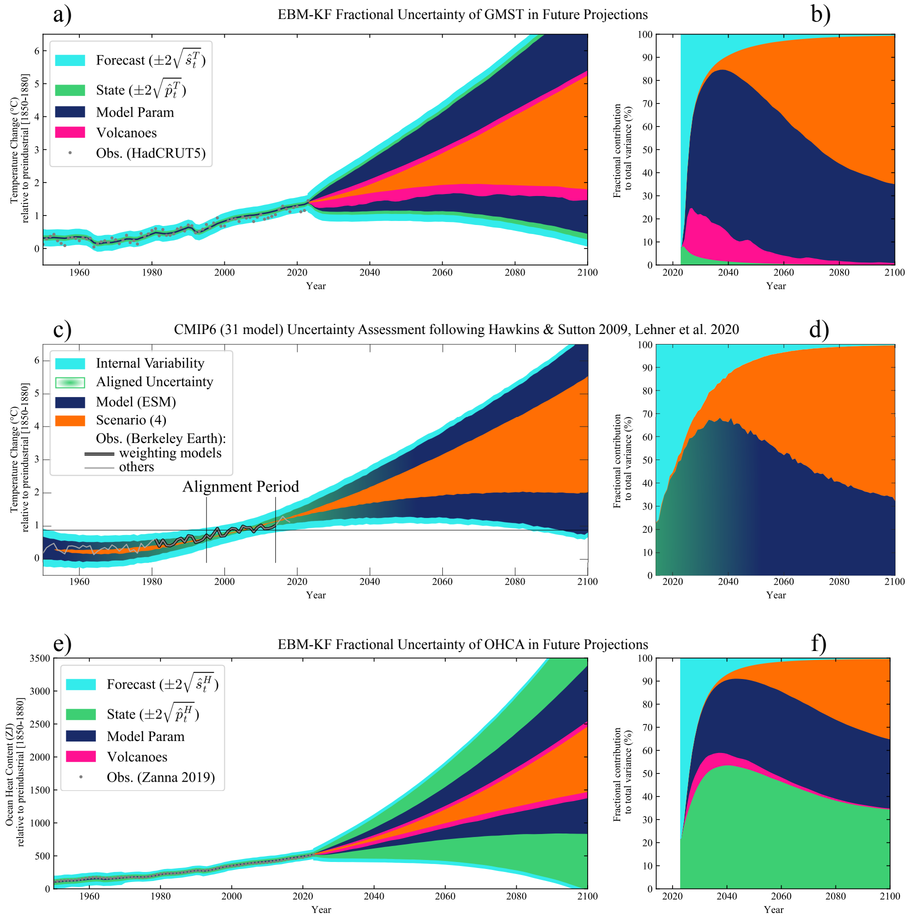


FIG. 11. "Hawkins Plots" (Hawkins and Sutton 2009) of the sources of uncertainty (95% CI on left, fractional variance on the right) in future projections, with the top row (a, b) showing the GMST state projections from the EBM-KF, the middle row (c,d) showing global mean surface air temperature GSAT from CMIP6 (following Lehner et al. (2020)), and the bottom figure (e,f) showing the OHCA projections from the EBM-KF. Internal dynamical or forecast variability is colored light blue in all figures, and while initially dominant (≥ 80%), it quickly falls off within the first decade, to eventually be replaced with emissions scenario uncertainty in orange. The smoothed CMIP6 ESMs have been both calibrated to the same baseline over an alignment period (1995-2014) and weighted according to their correlation with a longer trend (1981-2014). The spread of smoothed ESMs after both alignment and weighting is colored in light green in the alignment window, as it is roughly analogous to the climate state covariance within the EBM-KF. This aligned uncertainty melds into model uncertainty (navy blue) as the ESM models diverge in panels c & d. Future uncertainty related to volcanoes (in magenta) is negatively skewed and very important in the first 3-25 years of the EBM-KF's projections of GMST.

the multi-model ensemble spread (green-blue striped pattern). For simplicity, we estimated the model and parameter uncertainty of the EBM-KF by just varying the cloud feedback parameter (samples from $\mathcal{N}\left(0.42,\ 0.36^2\right)$, based on Figure 7.10 and Table 7.10 of AR6 (Forster et al. 2021)) and the ocean heat conductivity (samples from $\mathcal{N}\left(0.67,\ 0.15^2\right)$, based on Geoffroy et al. (2013a)). Incomplete understanding of cloud feedback is a primary source of uncertainty within ESMs, leading to diverging predictions within CMIP6 (Ceppi and Nowack 2021; Zelinka et al. 2017). Even though the cloud and OHCA dynamics of EBM-KF are oversimplified (Cheng et al. 2022; Newsom et al. 2023) and sparse long-term records yield disparate OHCA reconstructions before 2005 (Gulev et al. 2021, Figure 2.26), the GMST and OHCA uncertainty ranges from the EBM-KF can help quantify beyond what is known how to estimate in CMIP6. Were we to go further and assimilate the CMIP6 temperature and OHCA records into the EBM-KF (as done for the LENS2 in Section 3c), these additional quantifications of uncertainty could be brought to bear on the CMIP6 ensemble.

Regarding the various types of climate policy thresholds, the LENS2 can be used to generate very similar results to the EBM-KF (Figs. 6 & 12). Differences in absolute probability and policy threshold crossing instants reflect differences in the modeled climate states: particularly that the LENS2 ensemble was slightly cooler than the EBM-KF model after correcting to the same preindustrial temperature, so policy thresholds were crossed 3-5 years later (Fig. 12). The eruption of Mt. Pinatubo caused the policy threshold of +0.5K to be crossed in three instants within the EBM-KF model, because this eruption temporarily cooled the climate state back below the threshold temperature. The first of these EBM-KF crossings coincides very closely with the (single) policy threshold crossing instant of the 30-year running mean (indicated by orange asterisks). The 21-year running averages of the LENS2 simulations only crossed the 0.5K threshold once. Future threshold crossings (1.5K, 2.0K, 2.5K) under the SSP3-7.0 projection scenario show close temporal alignment in the threshold instants between LENS2 and the EBM-KF estimates that sample for volcanic uncertainty. Although shifted, the overall shapes of these cumulative distribution functions and spans of the threshold crossing windows are more similar between LENS2 and a single EBM-KF future estimate that like LENS2 keeps AOD constant (see Fig. 12). In contrast, the EBM-KF-uf sampling over potential volcanic futures has a long tail (pink lines, lower row) regarding temperature forecast thresholds, extending the later bound of the crossing period by about 5 years, because there remains a modest chance that a large volcano will erupt and tip the temperature forecast below that threshold.

### *c. Potential Issues with the EBM-KF and Future Extensions*

This first climate Kalman filter does not generate regional temperatures nor other essential climate variables, such as precipitation. These variables are often highly non-Gaussian and may require an understanding of regional "dynamical tipping points" or other important nonlinear process aspects of climate change. Additionally, this 2-component EBM-KF lacks a "memory ENSO state" to allow for prediction of 2-7 year quasi-periodic El Nino events (Hu and Fedorov 2017), and without such a state our EBM-KF wrongly assumes that weather innovations $z_t^T$ have no autocorrelation. Therefore, this first EBM-KF is far from generating the information required to replace many aspects of large ensembles. An expanded global climate state vector, including precipitation, seasonal temperature, or eigenvalues of spatially decomposed principal components (e.g., ENSO modes) might be appended into this statistical framework with appropriate physical forward modeling (Yang et al. 2018).

Astute readers may note the estimated climate state and covariance within the EBM-KF are influenced by the choice of reconstructed HadCRUT5 GMST and Zanna et al. (2019) OHCA. With only minor modifications, the EBM-KF method could be used with multiple annual reconstructions at the same time, e.g., GISTEMP GMST (Lenssen et al. 2019) or other OHCA reconstructions (Cheng et al. 2017; Ishii et al. 2017), considering each as only an estimate of the true GMST or OHCA (Willner et al. 1976). Reconstructions of sea level rise could be used from different sources as further constraints on OHCA (Fox-Kemper et al. 2021; Palmer et al. 2021, 2018b).

Here we use pre-selected, constant parameters at their published values in the EBM-KF. However, methods for tuning parameters, including time-dependent parameters, within Kalman filters are much more extensively studied mathematically (Chen et al. 2021, 2018; Zhang and Atia 2020) than the methods thus far applied in climate sciences to diagnose parameter variations within EBMs or ESMs (e.g., the regional effects diagnosed in Armour et al. (2013) and the global effects found by Gregory and Andrews (2016)). Our EBM-KF hybrid presents an opportunity to adopt KF parameter optimization methods for the GMST, OHCA projection optimization problem. In a preliminary experiment with Bayesian parameter search to give better estimates of the coefficients

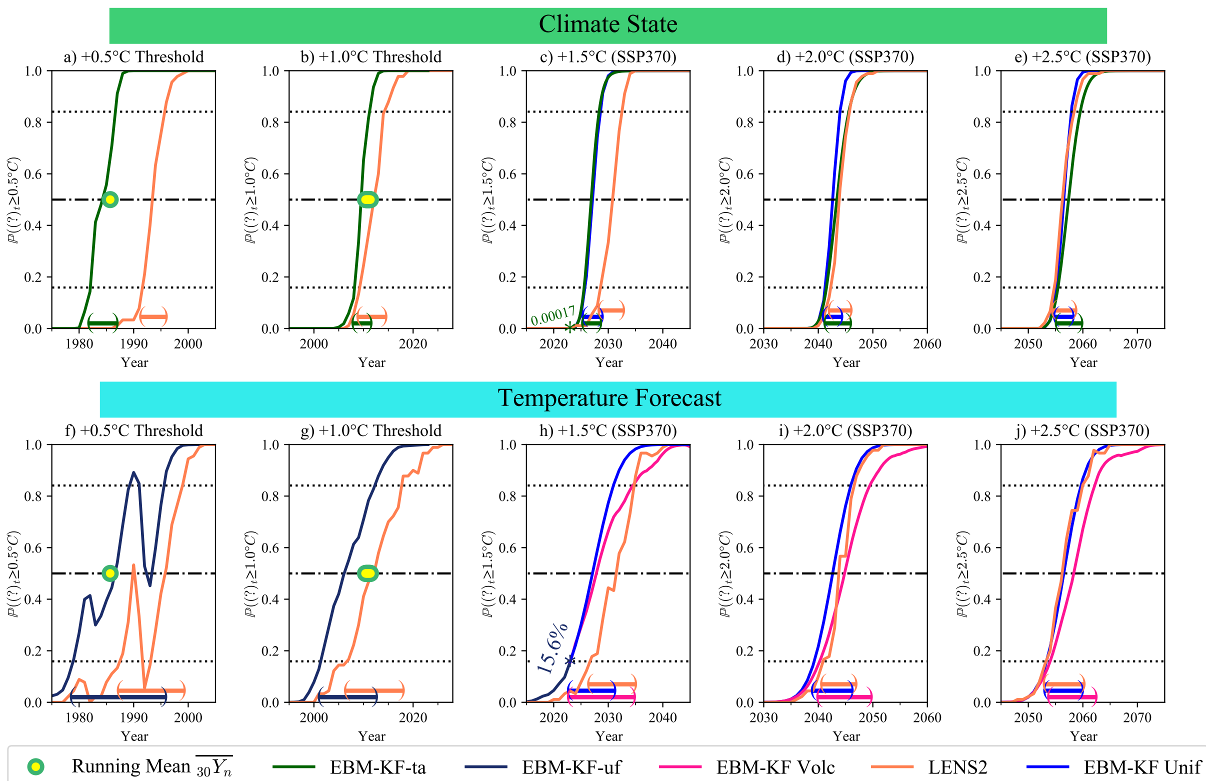


FIG. 12. Comparison of 0.5-2.5K GMST policy threshold crossing probabilities for various relevant preparations of the EBM-KF and CESM2 LENS simulations (orange). The top row of panels a-e compare climate states in the EBM-KF with 21-year averages of the LENS2 simulations. The bottom row f-j compares next-year temperature forecasts from the EBM-KF directly with the LENS2 simulations. Recall from Section 3b that these are the integrated probabilities of the GMST climate states or temperature forecasts below that policy threshold, with policy crossing instants when this probabiltiy is at 0.5. Historical EBM-KF-uf estimates of temperature forecasts are in dark blue in panels f,g (see Fig. 6c). EBM-KF-ta states (climate state thresholds) are shown in green in panels a,b. These EBM-KF-ta state estimates come the closest to matching the instants (yellow-green dots) when the 30-year running average crossed the 0.5°C threshold in 1985 (or very likely from a linear trend will have crossed the 1.0°C threshold in 2010 or 2011). Two versions of future EBM-KF state estimates are shown: an amalgamation of samples in pink (in h,i,j) from the volcanic distribution shown in Fig. 8, and a single run in bright blue (in c,d,e,h,i,j) with uniform $AOD_t = \overline{AOD}_{1850-2024} = 0.0123$ mirroring how LENS2 treats volcanism. In future climate state projections (green in c,d,e), samples of future volcanism are pre-processed according to EMB-KF-ta. Policy threshold crossing windows (thick bracketed lines at bottom) are also shown.

in the blind EBM, the prior distributions of these coefficients (rather than point estimates) were extracted from climate science literature, followed by a Metropolis-Hastings search. Several parameters required further care or tuning to achieve desired constraints (e.g., balanced energy transfer in the preindustrial climate), such as the main longwave radiation coefficient and the temperature exponent. However, identifiability and overfitting are challenges of this approach and deserve more attention than the scope of this paper allows. In this first illustration of the system, opportune imperfections in the point estimates given by literature sources allow demonstration of the course-corrective properties of the EBM-KF (Fig. 4).

### *d. Policy Utility*

Has the climate already passed the 1.5°C policy threshold? Real-time, accurate knowledge of policy threshold crossing will allow for more prudent planning and more comprehensible communication of climate science to the public. For instance, while the "Climate Clock" (`https://climateclock.world`) intends to communicate the urgency of the climate crisis with a countdown to the estimated expenditure of our remaining carbon budget, only a static date informs it. In contrast, an EBM-KF threshold reflects the most recently measured state of the Earth system and up-to-date emissions and present limits on future emissions. As can be seen in Fig. 12h, there was a substantial (15.5%) chance that 2023's GMST measurement could have exceeded the 1.5°C threshold. Indeed, the HadCRUT5 2023 number came close at 1.45°C, and others with slightly different methodologies reported 1.52°C above preindustrial (Burgess 2024). Rather than relying on sponge proxy data to posit that the climate state has exceeded this threshold (McCulloch et al. 2024), or using an overlap window between ESM projections and smoothed observations that is challenging to translate into probability (Hausfather 2024), the EBM-KF-ta can simply give a p-value (subject to our chosen point parameters and their quantifiable uncertainties in Fig. 11). By this method, we have not yet crossed the 1.5°C climate policy threshold: the EBM-KF-ta states (Fig. 12c) that there is p=0.00017 that the climate state exceeded 1.5°C in 2021.

Climate modeling with ESMs is slow, computationally expensive, and typically performed with blind models that do not respond to the latest observations. The relatively simple question, "How did the COVID-19 lockdowns and the 8% reduction in $CO_2$ emissions impact the near-term climate?" required hundreds of ESM simulations to yield a statistically insignificant answer (Jones et al.

2021). That sort of modeling effort, arriving months or years after the question was posed, is an unsatisfactory prize for many aspects of communication and decision making for the annual profit or election term. The EBM-KF can produce the result that an 8% emissions reduction over 2 years cools the climate state by ≈ 0.0017K and pushes back subsequent threshold crossing time by 1.2 months – an insufficient reduction in climate change, but at least precisely and rapidly quantified. The EBM-KF is sufficiently fast that, once fully calibrated, it could be easily embedded as an interactive web tool for such exploration. This demonstrates that, like "attributable anthropogenic warming" the EBM-KF is an "anti-fragile index" and therefore of greater use to planning climate mitigation strategies (Otto et al. 2015).

Additionally, Kalman filters are often used for process control (Lee and Ricker 1994; Myers and Luecke 1991), and in this case an EBM-KF could be used to optimize climate change mitigation or intervention strategies (Filar et al. 1996; Kravitz et al. 2016; MacMartin et al. 2014). For instance, within carbon offset, carbon sequestration, and geoengineering accreditation markets, credits could be assigned based on the projected delay in crossing policy thresholds. Once a space of potential climate solutions has been defined, the EBM-KF can work seamlessly with a variety of optimizers to find the maximum climate benefit at the lowest societal cost.

## 5. Conclusion

The EBM-KF-ta presented in this paper takes the best features from a 30-year running mean of GMST (the historical definition of climate) and state-of-the-art ESM large ensembles such as CESM2 LENS. The EBM-KF-ta GMST climate state, which also tracks the ocean heat content anomaly (OHCA), is constructed to be very close to that of a running 30-year mean but generates this climate state 15 years sooner: it has no lag in reporting after annual observations are collected. This filtered climate state captures the overall shape of the 30-year means of measured GMST ($r^2$ = 0.922) and OHCA ($r^2$ = 0.989). In comparison to the ensemble spread of a hindcast ensemble of an ESM (LENS2), which is the state-of-the-art method for quantifying internal variability and probabilistic futures, the EBM-KF-uf provides a similar Gaussian distribution. Using this distribution, EBM-KF-uf can annually assess the likelihood of whether a policy threshold, e.g., 1.5 or 2°C over preindustrial, has been crossed. The EBM-KF-uf is also accurate at inferring the behavior of an entire climate model large ensemble using only one or a few ensemble members, and can be used to distinguish novel sources of uncertainty in future projections, such as rare but significant future volcanic eruptions.

The EBM-KF approach has transparent, clean physical parameters of the EBM that can be directly measured or taken from estimates in modeling literature, leading to trivial uncertainty quantification by the Kalman filter machinery under fixed parameters. This uncertainty quantification revealed important aspects of GMST and OHCA uncertainty, both in hindcast and future projections contexts, with and without volcanoes. While the EBM-KF does not predict all climate variables of interest, it is a powerful, transparent, and inexpensive tool that may be readily combined with other approaches.

*Acknowledgments.* BFK's contributions were funded by ONR N00014-17-1-2393, NOAA NA19OAR4310366, and NSF OIA 2316271. JMN was funded by a Brown University Fellowship, a Brown 2023 OVPR Seed Award, and the 3CRS Project (NSF OIA 2316271). Conversations with Elizabeth Yankovsky, Anna Lo Piccolo, Joel Feske, Jochem Marotzke, Piers Forster, Lorraine E. Lisiecki, James (Jamie) Pringle, Zebedee Nicholls, Laure Zanna, Larissa Nazarenko, and Jung-Eun Lee helped to deepen and focus this work and locate data and other resources.

*Data availability statement.* This study performed re-analysis of existing datasets openly available at locations provided in Appendix A regarding historical $CO_2$ and $AOD_t$, for SSP projections at `https://greenhousegases.science.unimelb.edu.au/`, and for LENS2 at `https://www.earthsystemgrid.org/dataset/ucar.cgd.cesm2le.atm.proc.monthly_ave.TS.html`. For critical measurements of the climate state, GMST via HadCRUT5 is at `https://www.metoffice.gov.uk/hadobs/hadcrut5/data/current/download.html` and OHCA from Zanna et al. (2019) is at `https://zenodo.org/record/4603700\#.ZDuFNxXMI88`. Further documentation about data processing, copies of the utilized datasets, and EBM-KF Python code is available through Harvard Dataverse at `http://doi.org/10.7910/DVN/XLY8C2`.

# APPENDIX A

## Derivation of the Blind Energy-Balance Model

### *a. Overall Structure of the Model*

In the schematic diagram Fig. 2, one stream of incoming solar shortwave energy $\frac{1}{4}G_{SC}$ is successively fractionated by three reflective layers until a portion warms the ground and surface ocean. Then this surface layer radiates longwave infrared energy back to space ($\sigma_{sf}T^4$), again with greenhouse "reflection" in two layers. The surface ocean warms the deep ocean with fixed thermal insulation between them.

Temperature-dependent feedbacks are shown as cyclical arrows, with positive and negative feedback indicated relative to the overall energy balance. Positive feedbacks increase the energy flowing to the surface at higher surface temperatures $T$ either by decreasing the fraction of shortwave reflection or increasing the greenhouse "reflection". Prescribed forcings are indicated by gear symbols. Unknown coefficients $\beta_0, \beta_1, \beta_2, \beta_3$ exist respectively within the terms: $\tilde{g}(t), f_{H_2O}(T), f_{\alpha A}(T,t), f_{\alpha S}(T)$ in addition to the unknown exponent $\eta$. All these symbols are defined below.

Reiterating the overall structure in the model with discrete difference equations, $T_t$ is the temperature of the surface in calendar year $t$ (e.g. 2000), $\theta_t$ is the Conservative Temperature of the deep ocean in that same year, and $H_t$ is the total ocean heat content combining the heat in the surface ocean and deep ocean. The time step (abbreviated $k$ in Kalman filter literature) is 1 year. Units are omitted in this section for brevity. The overall energy flow into the Earth system and surface are:

$$\Delta\text{energy in total} = \mathcal{F}_{\text{SW}} - \phi_{\text{LW}} \tag{A1}$$

$$\Delta\text{energy at surface} = \mathcal{F}_{\text{SW}} - \phi_{\text{LW}} - Q_{\text{surf}\to\text{deep}} \tag{A2}$$

Equations (1)-(2) within Section 2a are describing the surface and deep ocean layers:

$$(T_{t+1} - T_t) \cdot C_{\text{surf}} = \underbrace{(\frac{1}{4}G_{\text{SC}})_t \cdot \tilde{d}_t \cdot f_{\alpha A}(T_t) \cdot f_{\alpha S}(T_t)}_{\mathcal{F}_{\text{SW}}} - \underbrace{\sigma_{sf} T_t^4 \cdot \tilde{g}_t \cdot f_{H_2O}(T_t)}_{\phi_{\text{LW}}} - \underbrace{\gamma \cdot (T_t - \theta_t - \zeta_0)}_{\text{Q}_{\text{surf}\to\text{deep}}} \tag{A3}$$

$$(\theta_{t+1} - \theta_t) \cdot C_{\text{deepO}} = \gamma \cdot (T_t - \theta_t - \zeta_0) \tag{A4}$$

Equation (3) to calculate OHCA is repeated below, along with its inverse transformation to obtain the deep ocean temperature:

$$H_t = (T_t - T_{1850}) \cdot C_{\text{upperO}} + (\theta_t - \theta_{1850}) \cdot C_{\text{deepO}} \tag{A5}$$

$$\theta_t = \big(H_t - (T_t - T_{1850}) \cdot C_{\text{upperO}}\big) / C_{\text{deepO}} + \theta_{1850} \tag{A6}$$

(A5) also applies to the subsequent time step (substituting $t \to t+1$), and then (A4)-(A6) are substituted:

$$H_{t+1} = (T_{t+1} - T_{1850}) \cdot C_{\text{upperO}} + \gamma \cdot (T_t - \theta_t - \zeta_0) + (\theta_t - \theta_{1850}) \cdot C_{\text{deepO}} \tag{A7}$$

Equation (A5) is again substituted into (A7):

$$H_{t+1} - H_t = (T_{t+1} - T_t) \cdot C_{\mathrm{upperO}} + \gamma \cdot (T_t - \theta_t - \zeta_0) \tag{A8}$$

Derivatives of $\theta_t$ from (A6):

$$\frac{\partial \theta_t}{\partial H_t} = 1/C_{\mathrm{deepO}} \tag{A9a}$$

$$\frac{\partial \theta_t}{\partial T_t} = C_{\mathrm{upperO}}/C_{\mathrm{deepO}} \tag{A9b}$$

On the right side of (A3), both the incoming shortwave radiative flux $\mathcal{F}_{SW}$ and outgoing longwave radiative flux $\phi_{\mathrm{LW}}$ take the same form: ((source $\frac{1}{4}G_{SC}$ or $\sigma_{sf}T^4$) * (prescribed attenuation from forcing: $\tilde{d}(t)$ or $\tilde{g}(t)$ ) * (attenuation functions with feedback: $f_{\alpha A}(T,t) \cdot f_{\alpha S}(T)$ or $f_{H_2O}(T)$). $C_{\mathrm{surf}}$, the heat capacity of the surface (including the atmosphere, thermally active soil, and an 86m upper layer of the ocean), was known least precisely of all coefficients: 17 ± 7 W (year) m$^{-2}$ K$^{-1}$ (Schwartz 2007). The deep ocean layer (technically the zone where most of the ocean warming occurs) was chosen for the purpose of heat capacity estimation to be an additional 1141m within the 71% of area covered by ocean based on previous work of this heat transfer process (Geoffroy et al. 2013b) This gives $C_{\mathrm{deepO}}$= 1141m *0.71 * 1030kg/m$^3$ * 4180Ws/kg/K * 1 yr/ (3.154*10$^7$s) = 155.7 W (year) m$^{-2}$ K$^{-1}$. Constants $\gamma, \zeta_0$ form a linear heat flux $Q_{\mathrm{surf}\rightarrow\mathrm{deep}}$ into the deep ocean, as discussed below.

### *b. Functional Forms of Components*

For brevity, derivations and detailed explanations of each of these components has been moved to the Supplement (A1 & A2). Here the functional form of each component is provided. We begin with the heat flowing from the surface layer into the deep ocean:

$$Q_{surf\rightarrow deep} = \gamma \cdot (\Delta T_t - \Delta\theta_t) = \gamma \cdot \big(T_t - \theta_t - \underbrace{(T_{1850} - \theta_{1850})}_{\zeta_0}\big) \tag{A10}$$

The fraction of shortwave (incoming) light reflected by $AOD_t$ is from Harshvardhan and King (1993)

$$\tilde{d}(t) \approx \frac{9.07}{AOD_t + 9.73} \tag{A11}$$

The fraction of longwave radiation absorbed by greenhouse gases is:

$$\tilde{g}(t) = 1 - \beta_0 \log_{10}([eCO_2]_t) < 1 \tag{A12}$$

Blackbody radiation, source of longwave outgoing radiation is the term $\sigma_{sf} T^4$, and the whole outgoing longwave radiation flux could be alternatively described in two ways:

$$\phi_{\text{LW}}(\text{outgoing}) = \sigma_{sf} T_t^4 - \frac{\phi_{\text{LW(absorbed)}}}{2} = \sigma_{\text{sf}} T_t^4 \cdot \tilde{g}(t) \cdot f_{H_2O}(T_t) \tag{A13}$$

In this paper we use the form of (A13) at right which relates $CO_2$ to a faction absorbed (similarly to albedo). Other authors favor the expression in the center of (A13), as it relates the absorption of a greenhouse gas to a power (in W/m$^2$) rather than an expression.

The expression reported by Forster et al. (2023) for the blocked outgoing longwave radiation follows the center form and is written below in (A14). To be used within our our EBM this expression must be converted into a fraction to solve for $\beta_0$ in (A12).

$$\phi_{\text{LW}}^{CO_2} = 12.74 \log_{10}([eCO_2]_t) - 31.55 \tag{A14}$$

Functions proposed by the authors for the water feedback (on absorbing fraction of longwave radiation), atmospheric albedo feedback, and surface albedo feedback are:

$$f_{H_2O}(T_t) := \beta_1 \left(\frac{1}{T_t}\right)^{\eta} \quad \approx \quad 1 - (1 + \beta_1 (T_t - T_{2002})^{-\eta} - \beta_1 \eta (T_{2002})^{-\eta-1} (T_t - T_{2002})) \tag{A15}$$

$$f_{\alpha A}(T_t, t) := 0.834\,(1 + \beta_2 (T_t - T_{2002})) + \frac{AC_t - AC_{2002}}{(\frac{1}{4} G_{SC})_t \cdot d_{2002}} \tag{A16}$$

$$f_{\alpha S}(T_t) := 0.909\,(1 + \beta_3 (T_t - T_{2002})) \tag{A17}$$

Note that the values of 0.834 and 0.909 came from the CERES satellite in the early 2000s (Loeb et al. 2009; Wielicki et al. 1996). Solving for all the coefficients by differentiating (see Supplement (SA17)- (SA20), we find from feedbacks assessed in ESM (CMIP6 & AR6):

$$\eta = 1.615 \tag{A18a}$$

$$\beta_2 = 0.00136 K^{-1} \tag{A18b}$$

$$\beta_3 = 0.00163 K^{-1} \tag{A18c}$$

By assuming the climate was at equilibrium before 1850 and assimilating the longwave anthropogenic greenhouse gas and anthropogenic aerosol energy fluxes published by Forster (Forster et al. 2023) at `https://github.com/ClimateIndicator/forcing-timeseries/tree/main/output`, we find:

$$\beta_1 = 6592.35 \tag{A19a}$$

$$\beta_0 = 0.046585 \tag{A19b}$$

This yields the following energy fluxes in 2002 displayed in Fig. A1, which are comparable to those obtained by Wild et al. (2015) and Wild et al. (2019).

*c. Differentiating to Find the Jacobian Matrix*

The above derivation yielded a blind energy-balance model with good skill at predicting the GMST (orange dashed line in Fig. 2), $r^2$ = 0.908 blind versus HadCRUT5. Rewriting the overall model with $\beta$ coefficients and ,

$$\begin{aligned} T_{t+1} = T_t + &\frac{(\frac{1}{4}G_{SC})_t \cdot 0.758 \cdot 9.068}{C_{\text{surf}} \cdot (AOD_t + 9.731)} \left( 1 + \beta_2 (T_t - Y_{2002}) + \frac{AC_t - AC_{2002}}{(\frac{1}{4}\overline{G_{SC}}) \cdot \tilde{d}_{2002} \cdot 0.834} \right) \big(1 + \beta_3 (T_t - Y_{2002})\big) \\ &- \frac{\sigma_{sf}\beta_1}{C_{\text{surf}}} (T_t)^{2.385} \big(1 - \beta_0 \log_{10}([eCO_2]_t)\big) - \frac{\gamma}{C_{\text{surf}}} (T_t - \theta_t - \zeta_0) \end{aligned} \tag{A20}$$

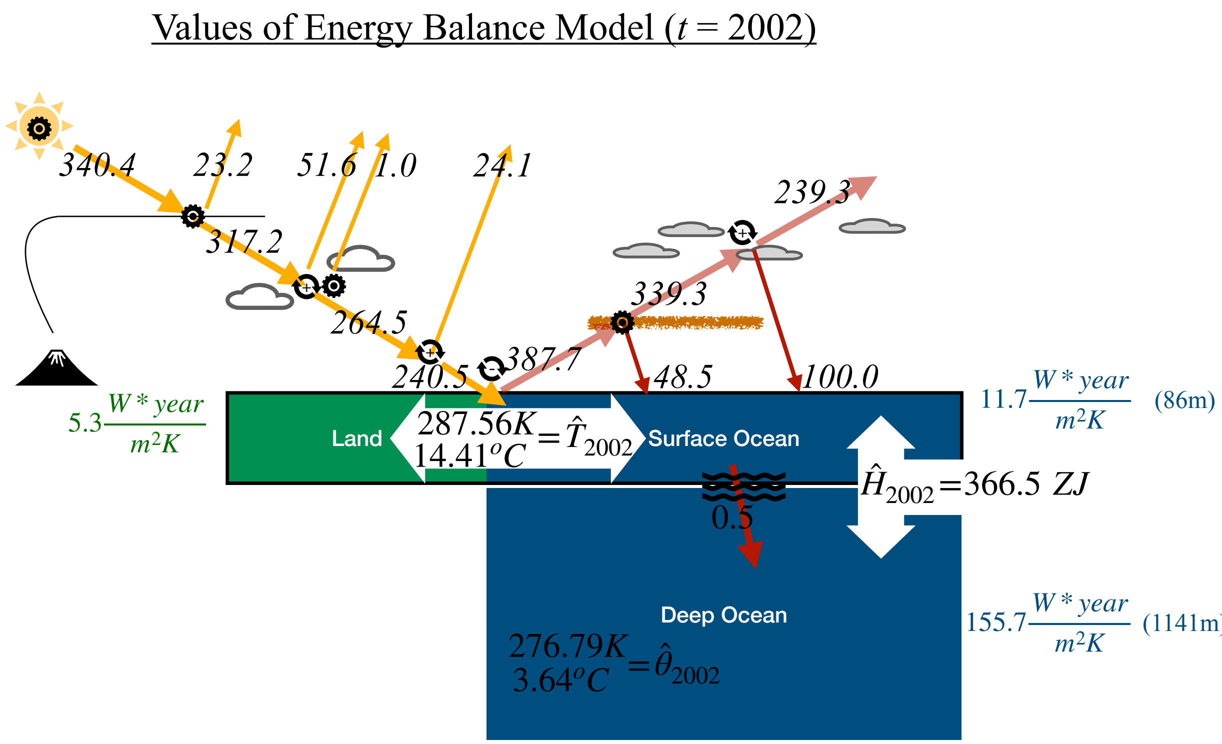


FIG. A1. Diagram with energy fluxes, temperatures, and total ocean heat content for the blind run of energy balance model in 2002 (when many of the reflectivity values were first measured by the CERES satellite). All numbers without units are in W/m$^2$. Rounding to the nearest 0.1 W/m$^2$ was performed after calculations.

Partial derivatives of this update equation are taken below, using the partial derivates of $\theta_t$ written above in (A9), also substituting $(\frac{1}{4}G_{SC})_t \approx (\frac{1}{4}\overline{G_{SC}}) = 340.2$ :

$$\begin{aligned}\frac{\partial T_{t+1}}{\partial T_t} =& 1+\frac{137.6}{(AOD_t+9.731)}\Big(\beta_2+\beta_3+2\beta_2\beta_3(T_t-Y_{2002})+\beta_3\frac{AC_t-AC_{2002}}{(\frac{1}{4}\overline{G_{SC}})\cdot\tilde{d}_{2002}\cdot 0.834}\Big)\\ &-\frac{2.385\sigma_{sf}\beta_1}{C_{\text{surf}}}(T_t)^{1.385}\big(1-\beta_0\log_{10}([eCO_2]_t)\big)-\frac{\gamma}{C_{\text{surf}}}(1-\underbrace{C_{\text{upperO}}/C_{\text{deepO}}}_{\frac{\partial\theta_t}{\partial T_t}})\end{aligned} \tag{A21}$$

$$\frac{\partial T_{t+1}}{\partial H_t} = \frac{\gamma}{C_{\text{surf}}}\cdot\frac{\partial\theta_t}{\partial H_t} = \frac{\gamma}{C_{\text{surf}}C_{\text{deepO}}} \tag{A22}$$

The ocean heat content update equation is written in (A7) with ($r^2$ = 0.910 blind OHCA versus Zanna et al. (2019)) and related partial derivates are:

$$\frac{\partial H_{t+1}}{\partial H_t} = C_{\text{upperO}} \frac{\partial T_{t+1}}{\partial H_t} + \gamma \cdot (0 - \frac{\partial \theta_t}{\partial H_t}) + C_{\text{deepO}} \frac{\partial \theta_t}{\partial H_t} = \frac{\gamma}{C_{\text{deepO}}} (\frac{C_{\text{upperO}}}{C_{\text{surf}}} - 1) + 1 \qquad \text{(A23)}$$

$$\frac{\partial H_{t+1}}{\partial T_t} = C_{\text{upperO}} \frac{\partial T_{t+1}}{\partial H_t} + \gamma \cdot (1 - \frac{C_{\text{upperO}}}{C_{\text{deepO}}}) + C_{\text{upperO}} \qquad \text{(A24)}$$

The Jacobian matrix is thus complete, as $\mathbf{\Phi}_t = \begin{bmatrix} \frac{\partial T_{t+1}}{\partial T_t} & \frac{\partial T_{t+1}}{\partial H_t} \\ \frac{\partial H_{t+1}}{\partial T_t} & \frac{\partial H_{t+1}}{\partial H_t} \end{bmatrix}$.

# APPENDIX B

## Generation of Volcanic Eruption Samples

As can be appreciated in Fig. B1a, long periods of no major volcanic eruptions (for instance 1935–1960) alternated with periods of many eruptions occurring in rapid succession (1883–1914, 1960–1994). This observed pattern prevented one Poisson distribution from describing the data well, but an exponential mixture did much better.

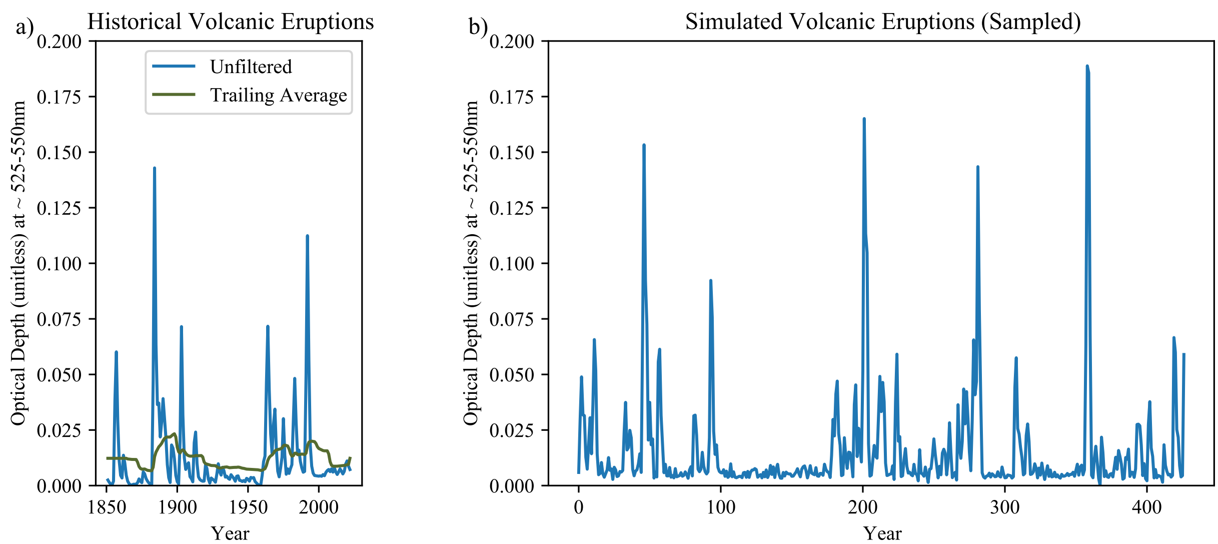


FIG. B1. Comparison of Historical Volcanic Eruptions (B1a) with Simulated Volcanic Eruptions (B1b), generated from a combination of several probability distributions. Observe in panel a that the unfiltered aerosol optical depths $AOD_t$ are plotted in blue, whereas the trailing average filter is plotted in green (it combines 15 years of a trailing average and 15 years of future projections at the mean AOD).

Eruptions that occurred within 3 years were indistinguishable in the historical dataset, so the minimum time interval between simulated volcanic eruptions was 2.6 years plus a sample (Table B1) from the exponential mixture model $i_t$ (Okada et al. 2020). These intervals were rounded to integers. Similarly, the size of each volcanic eruption $h_t$ was approximated using another shifted exponential distribution. The preceding year and two years following the eruption peak were positive fractions of the maximum aerosol optical depth, with Gaussian blur. Similarly, non-volcanic years were positive Gaussian noise (Table B2). Fig. B1b shows a sample from this combined generating function.

TABLE B1. Exponential Parameters of Volcano Generating Function. This generating function starts with a list of zero values for all $AOD_t$, and first samples several of these t years to be major volcanic eruptions. "Interval Between" refers to the interval in years between the peaks of two successive major volcanic eruptions.

| Exponential Distributions | Rand. Var. | Scale (units) | $\mathbb{P}$(used) |
|---|---|---|---|
| Interval Between: $\text{round}(i_{t,0} + 2.6)$ | $i_{t,0}$ ~Exp | 2.263 (years) | 88.9% |
| Interval Between: $\text{round}(i_{t,1} + 2.6)$ | $i_{t,1}$ ~Exp | 24.2 (years) | 11.1% |
| Peak Size: $AOD_t = h_t + 0.0082$ | $h_t$ ~Exp | 0.0339 (m) | only "eruption" years |

TABLE B2. Gaussian Parameters of Volcano Generating Function. These distributions are sampled after the major eruptions have already been filled in by the exponential distributions in Table B1.

| Truncated Gaussian Distributions | Rand. Var. | Mean $\mu$ (units) | Std Dev $\sigma$ (units) |
|---|---|---|---|
| Pre-Peak -1: $AOD_{t-1} = a_{-1} * AOD_t$ | $a_{-1} \sim (\mathcal{N} > 0)$ | 0.51 | 0.25 |
| Post-Peak 1: $AOD_{t+1} = a_1 * AOD_t$ | $a_1 \sim (\mathcal{N} > 0)$ | 0.61 | 0.16 |
| Post-Peak 2: $AOD_{t+2} = a_2 * AOD_t$ | $a_2\ (\mathcal{N} > 0)$ | 0.32 | 0.16 |
| Other Years: $AOD_t = a_0$ | $a_0 \sim (\mathcal{N} > 0)$ | 0.00371 (m) | 0.00286 (m) |

The overall procedure was to first create a series of spaced volcanic eruptions using Table B1, and then infill all the adjacent and non-volcano years using Table B2. It is beyond the scope of this paper to investigated whether this statistical pattern has some relation to magma or tectonic dynamics, or is merely an artifact of phasing.

# APPENDIX C

## Glossary of Mathematical Symbols and Notation

| Symbol | Meaning within **Statistics** | Units |
|---|---|---|
| $p, \mathbb{P}(\text{ event })$ | Probability of observed result for a particular hypothesis test (e.g. slope is positive) | [0-1] |
| r$^2$ | Coefficient of determination: fraction of variance explained by a model | [0-1] |
| $\mu$ | Mean of a set or distribution | any |
| $\sigma$ | Standard deviation ( $\sqrt{\text{variance}}$) | any |
| $\mathcal{N}(\mu, \sigma^2)$ | Gaussian (normal) distribution | any |
| $\mu \pm 2\sigma$ = 95% CI | 95% confidence interval (extremely likely) under Gaussian distribution | any |
| $Cov()$ | Covariance of a random vector (here $\mathbf{y}_t$ has length 2, so its covariance is 2x2) | sq. matrix |
| Symbol | Meaning within **Energy Balance Model** | Units |
| $t, k$ | Time index, time step | year |
| $T_t$ | GMST surface temperature climate state, idealized | K (°C) |
| $\theta_t$ | Deep ocean Conservative temperature state, idealized | K (°C) |
| $H_t$ | Ocean heat content anomaly, idealized | $\frac{W\ yr}{m^2}$(ZJ) |
| $u_t$ | Set of time-varying forcing inputs to the atmosphere (4 items below) | |
| $[eCO_2]_t$ | Amount of total greenhouse gas in the atmosphere, in effective concentration of $CO_2$ | ppm |
| $AOD_t$ | Aerosol optical depth (from top of atmosphere), affected by volcanoes | $\emptyset$ (AOD) |
| $AC_t$ | Cloud radiative forcing due to change in reflectivity by anthropogenic aerosols | $W/m^2$ |
| $(\frac{1}{4}G_{SC})_t$ | Top of atmosphere total solar irradiance | $W/m^2$ |
| $\mathcal{F}_{\text{SW}}, \phi_{\text{LW}}$ | Net radiative fluxes (shortwave, longwave) at the top of the atmosphere | $W/m^2$ |
| $\Delta$energy at surface | Net heat flow into the surface layer | $W/m^2$ |
| $Q_{\text{surf}\to\text{deep}}$ | Heat flow into the deep ocean layer | $W/m^2$ |
| $C_{\text{surf}}, C_{\text{upperO}}, C_{\text{deepO}}$ | Heat capacities of the surface, surface ocean, and deep ocean | $\frac{W\ yr}{m^2 K}$ |
| $\sigma_{sf}T^4$ | Source of outgoing longwave radiation (blackbody or Planck feedback) | $W/m^2$ |
| $\sigma_{sf}$ | Stefan-Boltzman constant = $5.67010^{-8}$ | $\frac{W}{m^2 K^4}$ |
| $\tilde{d}_t, \tilde{g}_t$ | Prescribed, time-varying attenuations from $AOD_t$ and $[eCO2]_t$ respectively | $\emptyset$ |
| $f_{\alpha A}(T,t) \cdot f_{\alpha S}(T)$ | Attenuations of incoming shortwave radiation due to albedo of the atmosphere and land surface respectively (feedback from $T_t$) | $\emptyset$ |
| $f_{H_2O}(T)$ | Attenuation of outgoing longwave radiation by water vapor (feedback from $T_t$) | $\emptyset$ |
| $\zeta_0$ | Equilibrium temperature difference between the surface and deep ocean | K (°C) |
| $HCa_t$ | The HadCRUT5 anomaly record (Morice et al. 2021) | K (°C) |
| $\zeta_1$ | Baseline temperature for HadCRUT5 to achieve the appropriate 1960-1989 climate normal (Jones and Harpham 2013) | K (°C) |
| $\beta_0$ | Solved coefficient on $\log_{10}([eCO_2]_t)$ within a sequential filter atmosphere approx. | $\emptyset$ |
| $\beta_1, \eta$ | Solved coefficient and exponent for the $f_{H_2O}(T)$ water vapor longwave feedback | $\emptyset$ |
| $\beta_2, \beta_3$ | Solved coefficients for $f_{\alpha A}(T,t) \cdot f_{\alpha S}(T)$ atmosphere and surface albedo feedbacks | $\emptyset$ |
| $c_1, c_2, c_3, c_4$ | Simplifications of constants within the EBM for equations (4)-(6) | See Table 1 |
| $[\tilde{T}_{t+1}, \tilde{H}_{t+1}] = \mathbf{F}(\tilde{T}_t, \tilde{H}_t; u_t)$ | Blind energy balance model, deterministic from prior climate state, no data assimilation | $[K, \frac{W\ yr}{m^2}]$ |

| Symbol | Meaning within **(Extended) Kalman Filter** | Units |
|---|---|---|
| $\mathbf{x}_t = [T_t, H_t]$ | Idealized true climate state, with dynamic model noise | $[K, \frac{W\ yr}{m^2}]$ |
| $\mathbf{y}_t = [Y_t, \psi_t]$ | Measurements with noise of the climate state, GMST from HadCRUT5 (Jones and Harpham 2013) and OHCA from Zanna et al. (2019) | $[K, \frac{W\ yr}{m^2}]$ |
| $\mathbf{Q} = Cov(w_t)$ | Assumed dynamic model error and model covariance matrix | $\begin{bmatrix} K^2 & K\frac{W\ yr}{m^2} \\ K\frac{W\ yr}{m^2} & (\frac{W\ yr}{m^2})^2 \end{bmatrix}$ |
| $\mathbf{R} = Cov(v_t)$ | Assumed measurement error and measurement covariance matrix | As $\mathbf{Q}$ above. |
| $\mathbf{R}_t = \mathbf{R}_t^{var} + \mathbf{R}^{const}$ <br> $\mathbf{Q} = \mathbf{R}^{const}/30$ | Actual model and measurement covariance matrices used in the EBM-KF, defined to mimic the statistics of the 30-year running mean | As $\mathbf{Q}$ above. |
| $\hat{\mathbf{x}}_t = [\hat{T}_t, \hat{H}_t]$ | Posterior estimated state (after measurement assimilation) | $[K, \frac{W\ yr}{m^2}]$ |
| $\mathbf{P}_t$ | Posterior estimated state covariance (after measurement assimilation) | As $\mathbf{Q}$ above. |
| $[\hat{p}_t^T, \hat{p}_t^H] = \mathrm{diag}(\mathbf{P}_t)$ | Elements of state variance exclusive to GMST and OHCA | $[K^2, (\frac{W\ yr}{m^2})^2]$ |
| $\mathbf{\Phi}_t = \frac{\partial \mathbf{F}(\mathbf{x};u_t)}{\partial \mathbf{x}}\rvert_{\mathbf{x}=\hat{\mathbf{x}}_{t-1}}$ | Linearized Jacobian tensor derivative of the (blind) EBM model | $\begin{bmatrix} \emptyset & K/\frac{W\ yr}{m^2} \\ \frac{W\ yr}{m^2}/K & \emptyset \end{bmatrix}$ |
| $\hat{\mathbf{x}}_{t\|t-1} = [\hat{T}_{t\|t-1}, \hat{H}_{t\|t-1}]$ | Forecast state projection (before new measurement) | $[K, \frac{W\ yr}{m^2}]$ |
| $\mathbf{P}_{t\|t-1}$ | Forecast covariance projection (before new measurement) | As $\mathbf{Q}$ above. |
| $\mathbf{z}_t = [z_t^T, z_t^H]$ | Innovation residual | $[K, \frac{W\ yr}{m^2}]$ |
| $\mathbf{S}_t$ | Innovation covariance | As $\mathbf{Q}$ above. |
| $[\hat{s}_t^T, \hat{s}_t^H] = \mathrm{diag}(\mathbf{S}_t)$ | Elements of innovation variance exclusive to GMST and OHCA | $[K^2, (\frac{W\ yr}{m^2})^2]$ |
| $\mathbf{K}_t$ | Kalman gain | $\begin{bmatrix} \emptyset & \emptyset \\ \emptyset & \emptyset \end{bmatrix}$ |

| Symbol | Meaning within **ESM Ensembles (LENS2)** | Units |
|---|---|---|
| $(Y_t)_j$ | The $j$th ensemble member's annual mean at time $t$ of near-surface air temperature | $K$ |
| $(\psi_t)_j$ | The $j$th ensemble member's annual mean at time $t$ of total ocean heat content | $\frac{W\ yr}{m^2}$ |
| $\overline{(Y_t)_j}$ | Ensemble average (across all members eg. 90) at year $t$ | $K$ |
| $(\overline{_{21}Y_t})_j$ | The 21-year running mean of ensemble member $j$ | $K$ |
| $\overline{(\overline{_{21}Y_t})_j}$ | The cross-ensemble average of all 21-year running means | $K$ |
| $_{ens}\sigma_t^T$ | The cross-ensemble standard deviation of GMST, see (24) | $K$ |
| $N$ | Number of ensemble members within a subset of the larger ensemble, see (24) | $\emptyset$ |

| Symbol | Meaning within **Volcanic Eruption Distribution** | Units |
|---|---|---|
| $i_{t,0}$ , $i_{t,1}$ | Exponential mixture random vars. to determine intervals between major eruptions | (years) |
| $h_t$ | Exponential random variable to determine size of a particular major eruption | $\emptyset$ (AOD) |
| $a_{-1}, a_1, a_2, a_0$ | Truncated gaussian distributions to determine the atmospheric optical depth in eruption-adjacent and non-eruption years. | $\emptyset$ (AOD) |

| Symbol | Meanings **(Miscellaneous Contexts)** | Units |
|---|---|---|
| $q$ | Location of a climate policy threshold, see (23) | K (°C) |
| $\hat{\hat{\mathbf{x}}}_t, \hat{\hat{\mathbf{P}}}_t, \hat{\hat{\mathbf{K}}}_t$ | Rauch-Tung-Striebel (RTS) smoother re-estimated state estimate, state covariance, and Kalman gain following backward sweep, see Supplement A3 | As above for KF |
| $_{30}\hat{Y}_t$ , $_{30}\hat{\mathbf{y}}_t$ | "Standard climate normal", a 30-year running mean of GMST or [GMST,OHCA] measurements, undefined before 1865 or after 2008 (as of this publication in 2024). | K , $[K, \frac{W\ yr}{m^2}]$ |
| $[a, b]$ | A vector with 2 indices | any |
| $[a — b]$ or $(a — b)$ | A closed or open interval from $a$ to $b$ | any |

## References


Abraham, J. P., and Coauthors, 2013: A review of global ocean temperature observations: Implications for ocean heat content estimates and climate change. *Reviews of Geophysics*, **51 (3)**, 450–483, https://doi.org/10.1002/rog.20022.

Armour, K. C., C. M. Bitz, and G. H. Roe, 2013: Time-varying climate sensitivity from regional feedbacks. *Journal of Climate*, **26 (13)**, 4518–4534, https://doi.org/10.1175/JCLI-D-12-00544.1.

Benhamou, E., 2018: Kalman filter demystified: from intuition to probabilistic graphical model to real case in financial markets. *arXiv e-prints*, **Statistical Finance (q-fin.ST) (arXiv:1811.11618)**, https://doi.org/10.48550/arXiv.1811.11618.

Betts, R., and Coauthors, 2023: Approaching 1.5 °c: how will we know we've reached this crucial warming mark? *Nature*, **624**, 33–35, https://doi.org/10.1038/d41586-023-03775-z.

Bouttier, F., 1996: Application of kalman filtering to numerical weather prediction. *Workshop on non-linear aspects of data assimilation*, ECMWF, URL https://www.ecmwf.int/sites/default/files/elibrary/1996/8347-application-kalman-filtering-numerical-weather-prediction.pdf.

Budyko, M. I., 1969: The effect of solar radiation variations on the climate of the earth. *Tellus*, **21 (5)**, 611–619, https://doi.org/10.3402/tellusa.v21i5.10109.

Buizza, R., M. Milleer, and T. N. Palmer, 1999: Stochastic representation of model uncertainties in the ecmwf ensemble prediction system. *Quarterly Journal of the Royal Meteorological Society*, **125 (560)**, 2887–2908, https://doi.org/10.1002/qj.49712556006.

Burgess, S., 2024: Copernicus: In 2024, the world experienced the warmest january on record. ECMWF, URL https://climate.copernicus.eu/copernicus-2024-world-experienced-warmest-january-record.

Carré, M., J. P. Sachs, J. M. Wallace, and C. Favier, 2012: Exploring errors in paleoclimate proxy reconstructions using monte carlo simulations: paleotemperature from mollusk and coral geochemistry. *Clim. Past*, **8 (2)**, 433–450, https://doi.org/10.5194/cp-8-433-2012.

Ceppi, P., and P. Nowack, 2021: Observational evidence that cloud feedback amplifies global warming. *Proceedings of the National Academy of Sciences*, **118 (30)**, e2026290 118, https://doi.org/10.1073/pnas.2026290118.

Chan, D., and P. Huybers, 2021: Correcting observational biases in sea surface temperature observations removes anomalous warmth during world war ii. *Journal of Climate*, **34 (11)**, 4585–4602, https://doi.org/10.1175/JCLI-D-20-0907.1.

Chen, Z., C. Heckman, S. Julier, and N. Ahmed, 2018: Weak in the nees?: Auto-tuning kalman filters with bayesian optimization. *2018 21st International Conference on Information Fusion (FUSION)*, 1072–1079, https://doi.org/10.23919/ICIF.2018.8454982.

Chen, Z., C. Heckman, S. J. Julier, and N. R. Ahmed, 2021: Time dependence in kalman filter tuning. *2021 IEEE 24th International Conference on Information Fusion (FUSION)*, 1–8.

Cheng, L., K. E. Trenberth, J. Fasullo, T. Boyer, J. Abraham, and J. Zhu, 2017: Improved estimates of ocean heat content from 1960 to 2015. *Science Advances*, **3 (3)**, e1601 545, https://doi.org/10.1126/sciadv.1601545.

Cheng, L., and Coauthors, 2022: Past and future ocean warming. *Nature Reviews Earth & Environment*, **3 (11)**, 776–794, https://doi.org/10.1038/s43017-022-00345-1.

Coddington, O., J. L. Lean, D. Lindholm, P. Pilewskie, M. Snow, and N. C. Program, 2017: Noaa climate data record (cdr) of total solar irradiance (tsi), nrltsi version 2.1. NOAA National Centers for Environmental Information, https://doi.org/10.7289/V56W985W.

Collins, M., and Coauthors, 2013: *Long-term climate change: Projections, commitments and irreversibility*, 1029–1136. Cambridge University Press, Cambridge, UK, https://doi.org/10.1017/CBO9781107415324.024.

Compo, G. P., and Coauthors, 2011: The twentieth century reanalysis project. *Quarterly Journal of the Royal Meteorological Society*, **137 (654)**, 1–28, https://doi.org/10.1002/qj.776.

Duffy, M. L., B. Medeiros, A. Gettelman, and T. Eidhammer, 2023: Perturbing parameters to understand cloud contributions to climate change. *Journal of Climate*, **[Preprint]**.

Edwards, T. L., and Coauthors, 2021: Projected land ice contributions to twenty-first-century sea level rise. *Nature*, **593 (7857)**, 74–82, https://doi.org/10.1038/s41586-021-03302-y.

Emile-Geay, J., and Coauthors, 2017: A global multiproxy database for temperature reconstructions of the common era. *Scientific Data*, **4 (1)**, 170 088, https://doi.org/10.1038/sdata.2017.88.

Feng, R., B. L. Otto-Bliesner, E. C. Brady, and N. Rosenbloom, 2020: Increased climate response and earth system sensitivity from ccsm4 to cesm2 in mid-pliocene simulations. *Journal of Advances in Modeling Earth Systems*, **12 (8)**, e2019MS002 033, https://doi.org/10.1029/2019MS002033.

Filar, J. A., P. S. Gaertner, and M. A. Janssen, 1996: *An Application of Optimization to the Problem of Climate Change*, 475–498. Springer US, Boston, MA, https://doi.org/10.1007/978-1-4613-3437-8_29, URL https://doi.org/10.1007/978-1-4613-3437-8_29.

Forster, P., and Coauthors, 2021: *The Earth's Energy Budget, Climate Feedbacks, and Climate Sensitivity*, book section 7, 923–1054. Cambridge University Press, Cambridge, United Kingdom and New York, NY, USA, https://doi.org/10.1017/9781009157896.009.

Forster, P. M., and Coauthors, 2023: Indicators of global climate change 2022: annual update of large-scale indicators of the state of the climate system and human influence. *Earth Syst. Sci. Data*, **15 (6)**, 2295–2327, https://doi.org/10.5194/essd-15-2295-2023.

Fox-Kemper, B., and Coauthors, 2021: *Ocean, Cryosphere and Sea Level Change*, book section 9, 1211–1362. Cambridge University Press, Cambridge, United Kingdom and New York, NY, USA, https://doi.org/10.1017/9781009157896.011.

Friedrich, T., A. Timmermann, M. Tigchelaar, O. Elison Timm, and A. Ganopolski, 2016: Nonlinear climate sensitivity and its implications for future greenhouse warming. *Science Advances*, **2 (11)**, e1501 923, https://doi.org/10.1126/sciadv.1501923.

Fujimori, S., T. Hasegawa, T. Masui, K. Takahashi, D. S. Herran, H. Dai, Y. Hijioka, and M. Kainuma, 2017: Ssp3: Aim implementation of shared socioeconomic pathways. *Global Environmental Change*, **42**, 268–283, https://doi.org/10.1016/j.gloenvcha.2016.06.009.

García-Pintado, J., and A. Paul, 2018: Evaluation of iterative kalman smoother schemes for multi-decadal past climate analysis with comprehensive earth system models. *Geosci. Model Dev.*, **11 (12)**, 5051–5084, https://doi.org/10.5194/gmd-11-5051-2018.

Geoffroy, O., D. Saint-Martin, G. Bellon, A. Voldoire, D. J. L. Olivié, and S. Tytéca, 2013a: Transient climate response in a two-layer energy-balance model. part ii: Representation of the efficacy of deep-ocean heat uptake and validation for cmip5 aogcms. *Journal of Climate*, **26 (6)**, 1859–1876, https://doi.org/10.1175/JCLI-D-12-00196.1.

Geoffroy, O., D. Saint-Martin, D. J. L. Olivié, A. Voldoire, G. Bellon, and S. Tytéca, 2013b: Transient climate response in a two-layer energy-balance model. part i: Analytical solution and parameter calibration using cmip5 aogcm experiments. *Journal of Climate*, **26 (6)**, 1841–1857, https://doi.org/10.1175/JCLI-D-12-00195.1.

Gerlach, T., 2011: Volcanic versus anthropogenic carbon dioxide. *Eos, Transactions, American Geophysical Union*, **92 (24)**, 201–202, https://doi.org/10.1029/2011EO240001.

Gettelman, A., and Coauthors, 2019: High climate sensitivity in the community earth system model version 2 (cesm2). *Geophysical Research Letters*, **46 (14)**, 8329–8337, https://doi.org/10.1029/2019GL083978.

Gregory, J. M., 2000: Vertical heat transports in the ocean and their effect on time-dependent climate change. *Climate Dynamics*, **16 (7)**, 501–515, https://doi.org/10.1007/s003820000059.

Gregory, J. M., and T. Andrews, 2016: Variation in climate sensitivity and feedback parameters during the historical period. *Geophysical Research Letters*, **43 (8)**, 3911–3920, https://doi.org/10.1002/2016GL068406.

Grewal, M., and A. Andrews, 2001: *Kalman Filtering: Theory and Practice Using MATLAB*. Wiley, URL https://books.google.com/books?id=9UoZAQAAIAAJ.

Gulev, S. K., and Coauthors, 2021: *Changing State of the Climate System*, book section 2, 287–422. Cambridge University Press, Cambridge, United Kingdom and New York, NY, USA, https://doi.org/10.1017/9781009157896.004.

Guttman, N. B., 1989: Statistical descriptors of climate. *Bulletin of the American Meteorological Society*, **70 (6)**, 602–607, https://doi.org/10.1175/1520-0477(1989)070⟨0602:SDOC⟩2.0.CO;2.

Hakim, G. J., J. Emile-Geay, E. J. Steig, D. Noone, D. M. Anderson, R. Tardif, N. Steiger, and W. A. Perkins, 2016: The last millennium climate reanalysis project: Framework and first results. *Journal of Geophysical Research: Atmospheres*, **121 (12)**, 6745–6764, https://doi.org/10.1002/2016JD024751.

Harshvardhan, and M. D. King, 1993: Comparative accuracy of diffuse radiative properties computed using selected multiple scattering approximations. *Journal of the Atmospheric Sciences*, **50 (2)**, 247–259, https://doi.org/10.1175/1520-0469(1993)050⟨0247:caodrp⟩2.0.co;2.

Hasselmann, K., 1997: Multi-pattern fingerprint method for detection and attribution of climate change. *Climate Dynamics*, **13 (9)**, 601–611, https://doi.org/10.1007/s003820050185.

Hausfather, Z., 2024: 02/14/2025. When will the world really pass 1.5c? twitter, URL https://twitter.com/hausfath/status/1757916875806392657?s=20.

Haustein, K., M. R. Allen, P. M. Forster, F. E. L. Otto, D. M. Mitchell, H. D. Matthews, and D. J. Frame, 2017: A real-time global warming index. *Scientific Reports*, **7 (1)**, 15 417, https://doi.org/10.1038/s41598-017-14828-5.

Hawkins, E., and R. Sutton, 2009: The potential to narrow uncertainty in regional climate predictions. *Bulletin of the American Meteorological Society*, **90 (8)**, 1095–1108, https://doi.org/10.1175/2009BAMS2607.1.

Held, I. M., M. Winton, K. Takahashi, T. Delworth, F. Zeng, and G. K. Vallis, 2010: Probing the fast and slow components of global warming by returning abruptly to preindustrial forcing. *Journal of Climate*, **23 (9)**, 2418–2427, https://doi.org/10.1175/2009JCLI3466.1.

Horvat, C., 2021: Marginal ice zone fraction benchmarks sea ice and climate model skill. *Nature Communications*, **12 (1)**, 2221, https://doi.org/10.1038/s41467-021-22004-7.

Houtekamer, P. L., and H. L. Mitchell, 1998: Data assimilation using an ensemble kalman filter technique. *Monthly Weather Review*, **126 (3)**, 796–811, https://doi.org/10.1175/1520-0493(1998)126⟨0796:DAUAEK⟩2.0.CO;2.

Hu, S., and A. V. Fedorov, 2017: The extreme el niÃ±o of 2015-2016 and the end of global warming hiatus. *Geophysical Research Letters*, **44 (8)**, 3816–3824, https://doi.org/10.1002/2017GL072908.

Huguenin, M. F., R. M. Holmes, and M. H. England, 2022: Drivers and distribution of global ocean heat uptake over the last half century. *Nature Communications*, **13 (1)**, 4921, https://doi.org/10.1038/s41467-022-32540-5.

Hummels, R., M. Dengler, and B. BourlÃ¨s, 2013: Seasonal and regional variability of upper ocean diapycnal heat flux in the atlantic cold tongue. *Progress in Oceanography*, **111**, 52–74, https://doi.org/10.1016/j.pocean.2012.11.001.

Illing, S., C. Kadow, H. Pohlmann, and C. Timmreck, 2018: Assessing the impact of a future volcanic eruption on decadal predictions. *Earth Syst. Dynam.*, **9 (2)**, 701–715, https://doi.org/10.5194/esd-9-701-2018.

Ishii, M., Y. Fukuda, S. Hirahara, S. Yasui, T. Suzuki, and K. Sato, 2017: Accuracy of global upper ocean heat content estimation expected from present observational data sets. *SOLA*, **13**, 163–167, https://doi.org/10.2151/sola.2017-030.

Jones, C. D., and Coauthors, 2021: The climate response to emissions reductions due to covid-19: Initial results from covidmip. *Geophysical Research Letters*, **48 (8)**, e2020GL091 883, https://doi.org/10.1029/2020GL091883.

Jones, P. D., and C. Harpham, 2013: Estimation of the absolute surface air temperature of the earth. *Journal of Geophysical Research: Atmospheres*, **118 (8)**, 3213–3217, https://doi.org/10.1002/jgrd.50359.

Jones, P. D., and P. M. Kelly, 1996: The effect of tropical explosive volcanic eruptions on surface air temperature. *The Mount Pinatubo Eruption*, G. Fiocco, D. Fuà, and G. Visconti, Eds., Springer Berlin Heidelberg, Berlin, Heidelberg, 95–111, https://doi.org/10.1007/978-3-642-61173-5_10.

Julier, S. J., and J. K. Uhlmann, 1997: New extension of the kalman filter to nonlinear systems. *Proc.SPIE*, Vol. 3068, 182–193, https://doi.org/10.1117/12.280797.

Kàlmàn, R. E., 1960: A new approach to linear filtering and prediction problems. *Journal of Basic Engineering*, **82 (1)**, 35–45, https://doi.org/10.1115/1.3662552.

Kàlmàn, R. E., and R. S. Bucy, 1961: New results in linear filtering and prediction theory. *Journal of Basic Engineering*, **83 (1)**, 95–108, https://doi.org/10.1115/1.3658902.

Kalnay, E., 2002: *Atmospheric Modeling, Data Assimilation and Predictability*. Cambridge University Press, Cambridge, https://doi.org/10.1017/CBO9780511802270, URL https://www.cambridge.org/core/books/atmospheric-modeling-data-assimilation-and-predictability/C5FD207439132836E85027754CE9BC1A.

Kaufman, D., and Coauthors, 2020: A global database of holocene paleotemperature records. *Scientific Data*, **7 (1)**, https://doi.org/10.1038/s41597-020-0445-3.

Keil, P., H. Schmidt, B. Stevens, and J. Bao, 2021: Variations of tropical lapse rates in climate models and their implications for upper-tropospheric warming. *Journal of Climate*, **34 (24)**, 9747–9761, https://doi.org/10.1175/JCLI-D-21-0196.1.

Kim, Y., and H. Bang, 2018: Introduction to kalman filter and its applications. *Introduction and Implementations of the Kalman Filter*, F. Govaers, Ed., IntechOpen, Rijeka, chap. 2, https://doi.org/10.5772/intechopen.80600.

Kirtman, B., and Coauthors, 2013: *Near-term climate change*, Vol. 9781107057999, 953–1028. Cambridge University Press, https://doi.org/10.1017/CBO9781107415324.023, URL http://www.scopus.com/inward/record.url?scp=84928617872\&partnerID=8YFLogxKhttp://www.scopus.com/inward/citedby.url?scp=84928617872\&partnerID=8YFLogxK, 10.1017/CBO9781107415324.023.

Kravitz, B., D. G. MacMartin, H. Wang, and P. J. Rasch, 2016: Geoengineering as a design problem. *Earth System Dynamics*, **7 (2)**, 469–497, https://doi.org/10.5194/esd-7-469-2016.

Kravitz, B., and Coauthors, 2018: The climate effects of increasing ocean albedo: an idealized representation of solar geoengineering. *Atmos. Chem. Phys.*, **18 (17)**, 13 097–13 113, https://doi.org/10.5194/acp-18-13097-2018.

Lacey, T., 1998: Tutorial: The kalman filter. URL https://www.academia.edu/download/44204714/Kalman_filter.pdf.

Lauritzen, S., and T. Thiele, 2002: *Thiele: Pioneer in Statistics*. Oxford University Press, URL https://books.google.com/books?id=irugmNUwuG4C.

Lauritzen, S. L., 1981: Time series analysis in 1880: A discussion of contributions made by t.n. thiele. *International Statistical Review / Revue Internationale de Statistique*, **49 (3)**, 319–331, https://doi.org/10.2307/1402616.

Lee, J. H., and N. L. Ricker, 1994: Extended kalman filter based nonlinear model predictive control. *Industrial and Engineering Chemistry Research*, **33 (6)**, 1530–1541, https://doi.org/10.1021/ie00030a013.

Lee, J. Y., and Coauthors, 2021: *Future Global Climate: Scenario-Based Projections and Near-Term Information*, book section 4, 553–672. Cambridge University Press, Cambridge, United Kingdom and New York, NY, USA, https://doi.org/10.1017/9781009157896.006.

Lehner, F., C. Deser, N. Maher, J. Marotzke, E. M. Fischer, L. Brunner, R. Knutti, and E. Hawkins, 2020: Partitioning climate projection uncertainty with multiple large ensembles and cmip5/6. *Earth Syst. Dynam.*, **11 (2)**, 491–508, https://doi.org/10.5194/esd-11-491-2020.

Lenssen, N. J. L., G. A. Schmidt, J. E. Hansen, M. J. Menne, A. Persin, R. Ruedy, and D. Zyss, 2019: Improvements in the gistemp uncertainty model. *Journal of Geophysical Research: Atmospheres*, **124 (12)**, 6307–6326, https://doi.org/10.1029/2018JD029522.

Levitus, S., and Coauthors, 2017: Ncei ocean heat content, temperature anomalies, salinity anomalies, thermosteric sea level anomalies, halosteric sea level anomalies, and total steric sea level anomalies from 1955 to present calculated from in situ oceanographic subsurface profile data. NOAA National Oceanic and Atmospheric Administration, https://doi.org/10.7289/v53f4mvp.

Loeb, N. G., B. A. Wielicki, D. R. Doelling, G. L. Smith, D. F. Keyes, S. Kato, N. Manalo-Smith, and T. Wong, 2009: Toward optimal closure of the earth's top-of-atmosphere radiation budget. *Journal of Climate*, **22 (3)**, 748–766, https://doi.org/10.1175/2008jcli2637.1.

MacMartin, D. G., B. Kravitz, and D. W. Keith, 2014: Geoengineering: The world's largest control problem. *2014 American Control Conference*, 2401–2406, https://doi.org/10.1109/ACC.2014.6858658.

Marotzke, J., and P. M. Forster, 2015: Forcing, feedback and internal variability in global temperature trends. *Nature*, **517 (7536)**, 565–570, https://doi.org/10.1038/nature14117.

Marshall, L. R., E. C. Maters, A. Schmidt, C. Timmreck, A. Robock, and M. Toohey, 2022: Volcanic effects on climate: recent advances and future avenues. *Bulletin of Volcanology*, **84 (5)**, 54, https://doi.org/10.1007/s00445-022-01559-3.

McClelland, H. L. O., I. Halevy, D. A. Wolf-Gladrow, D. Evans, and A. S. Bradley, 2021: Statistical uncertainty in paleoclimate proxy reconstructions. *Geophysical Research Letters*, **48 (15)**, e2021GL092 773, https://doi.org//10.1029/2021GL092773.

McCormick, M. P., L. W. Thomason, and C. R. Trepte, 1995: Atmospheric effects of the mt pinatubo eruption. *Nature*, **373 (6513)**, 399–404, https://doi.org/10.1038/373399a0.

McCulloch, M. T., A. Winter, C. E. Sherman, and J. A. Trotter, 2024: 300 years of sclerosponge thermometry shows global warming has exceeded 1.5c. *Nature Climate Change*, **14 (2)**, 171–177, https://doi.org/10.1038/s41558-023-01919-7.

McDougall, T. J., P. M. Barker, R. M. Holmes, R. Pawlowicz, S. M. Griffies, and P. J. Durack, 2021: The interpretation of temperature and salinity variables in numerical ocean model output and the calculation of heat fluxes and heat content. *Geosci. Model Dev.*, **14 (10)**, 6445–6466, https://doi.org/10.5194/gmd-14-6445-2021.

McKinnon, K. A., A. Poppick, E. Dunn-Sigouin, and C. Deser, 2017: An observational large ensemble to compare observed and modeled temperature trend uncertainty due to internal variability. *Journal of Climate*, **30 (19)**, 7585–7598, https://doi.org/10.1175/JCLI-D-16-0905.1.

Meehl, G. A., R. Moss, K. E. Taylor, V. Eyring, R. J. Stouffer, S. Bony, and B. Stevens, 2014: Climate model intercomparisons: Preparing for the next phase. *Eos, Transactions American Geophysical Union*, **95 (9)**, 77–78, https://doi.org/10.1002/2014EO090001.

Meinshausen, M., and Coauthors, 2020: The shared socio-economic pathway (ssp) greenhouse gas concentrations and their extensions to 2500. *Geosci. Model Dev.*, **13 (8)**, 3571–3605, https://doi.org/10.5194/gmd-13-3571-2020.

Merchant, C. J., and Coauthors, 2019: Satellite-based time-series of sea-surface temperature since 1981 for climate applications. *Scientific Data*, **6 (1)**, https://doi.org/10.1038/s41597-019-0236-x.

Miller, R., 1996: Introduction to the kalman filter. *Seminar on Data Assimilation, 2-6 September 1996*, ECMWF, Shinfield Park, Reading, 47–60, URL https://www.ecmwf.int/sites/default/files/elibrary/1996/75692-introduction-kalman-filter_0.pdf.

Miller, R. L., and Coauthors, 2014: Cmip5 historical simulations (1850-2012) with giss modele2. *Journal of Advances in Modeling Earth Systems*, **6 (2)**, 441–478, https://doi.org/10.1002/2013MS000266.

Montgomery, D. C., and G. C. Runger, 2013: *Applied Statistics and Probability for Engineers*. 6th ed., John Wiley & Sons, New York, NY.

Morice, C. P., and Coauthors, 2021: An updated assessment of near-surface temperature change from 1850: The hadcrut5 data set. *Journal of Geophysical Research: Atmospheres*, **126 (3)**, e2019JD032 361, https://doi.org/10.1029/2019JD032361.

Myers, M. A., and R. H. Luecke, 1991: Process control applications of an extended kalman filter algorithm. *Computers & Chemical Engineering*, **15 (12)**, 853–857, https://doi.org/10.1016/0098-1354(91)80030-Y.

NASA/LARC/SD/ASDC, 2018: Global space-based stratospheric aerosol climatology version 2.0. NASA, https://doi.org/10.5067/GLOSSAC-L3-V2.0.

Nazarenko, L. S., and Coauthors, 2022: Future climate change under ssp emission scenarios with giss-e2.1. *Journal of Advances in Modeling Earth Systems*, **14 (7)**, e2021MS002 871, https://doi.org/10.1029/2021MS002871.

Newsom, E., L. Zanna, and J. Gregory, 2023: Background pycnocline depth constrains future ocean heat uptake efficiency. *Geophysical Research Letters*, **50 (22)**, e2023GL105 673, https://doi.org/10.1029/2023GL105673.

Ogorek, B., 2019: Yet another kalman filter explanation article. Towards Data Science, URL https://towardsdatascience.com/yet-another-kalman-filter-explanation-article-be0264d99937.

Okada, M., K. Yamanishi, and N. Masuda, 2020: Long-tailed distributions of inter-event times as mixtures of exponential distributions. *Royal Society Open Science*, **7**, 191 643, https://doi.org/10.1098/rsos.191643.

Otto, F. E. L., D. J. Frame, A. Otto, and M. R. Allen, 2015: Embracing uncertainty in climate change policy. *Nature Climate Change*, **5 (10)**, 917–920, https://doi.org/10.1038/nclimate2716.

Palmer, M., G. Harris, and J. Gregory, 2018a: Extending cmip5 projections of global mean temperature change and sea level rise due to thermal expansion using a physically-based emulator. *Environmental Research Letters*, **13**, https://doi.org/10.1088/1748-9326/aad2e4.

Palmer, M., and Coauthors, 2018b: Ukcp18 marine report. Report, Met Office UK. URL http://nora.nerc.ac.uk/id/eprint/522257/.

Palmer, M. D., C. M. Domingues, A. B. A. Slangen, and F. Boeira Dias, 2021: An ensemble approach to quantify global mean sea-level rise over the 20th century from tide gauge reconstructions. *Environmental Research Letters*, **16 (4)**, 044 043, https://doi.org/10.1088/1748-9326/abdaec.

Papale, P., 2018: Global time-size distribution of volcanic eruptions on earth. *Scientific Reports*, **8 (1)**, 6838, https://doi.org/10.1038/s41598-018-25286-y.

Pielke Jr, R., M. G. Burgess, and J. Ritchie, 2022: Plausible 2005-2050 emissions scenarios project between 2°c and 3°c of warming by 2100. *Environmental Research Letters*, **17 (2)**, 024 027, https://doi.org/10.1088/1748-9326/ac4ebf.

Quevedo, H., and G. Gonzalez, 2017: Non-normal distribution of temperatures in the united states of america during 1895-2016: A challenge to the central limit theorem. *Pinnacle Environmental & Earth Sciences*, **4**, 1182.

Rauch, H. E., F. Tung, and C. T. Striebel, 1965: Maximum likelihood estimates of linear dynamic systems. *AIAA Journal*, **3 (8)**, 1445–1450, https://doi.org/10.2514/3.3166.

Roach, L. A., and Coauthors, 2020: Antarctic sea ice area in cmip6. *Geophysical Research Letters*, **47 (9)**, e2019GL086 729, https://doi.org/10.1029/2019GL086729.

Robinson, A., and H. Stommel, 1959: The oceanic thermocline and the associated thermohaline circulation. *Tellus*, **11**, 295–308, https://doi.org/10.1111/j.2153-3490.1959.tb00035.x.

Rodgers, K. B., and Coauthors, 2021: Ubiquity of human-induced changes in climate variability. *Earth Syst. Dynam.*, **12 (4)**, 1393–1411, https://doi.org/10.5194/esd-12-1393-2021.

Rosenblum, E., and I. Eisenman, 2017: Sea ice trends in climate models only accurate in runs with biased global warming. *Journal of Climate*, **30 (16)**, 6265–6278, https://doi.org/10.1175/JCLI-D-16-0455.1.

Sætrom, J., and H. Omre, 2013: Uncertainty quantification in the ensemble kalman filter. *Scandinavian Journal of Statistics*, **40 (4)**, 868–885, https://doi.org/10.111/sjos.12039.

Särkkä, S., 2013: *Bayesian Filtering and Smoothing*. Cambridge University Press, URL https://users.aalto.fi/~ssarkka/pub/cup_book_online_20131111.pdf.

Sato, M., J. E. Hansen, M. P. McCormick, and J. B. Pollack, 1993: Stratospheric aerosol optical depths, 1850-1990. *J. Geophys. Res.*, **98**, 22 987–22 994, https://doi.org/10.1029/93JD02553.

Schmidt, S. F., 1981: The kalman filter - its recognition and development for aerospace applications. *Journal of Guidance and Control*, **4 (1)**, 4–7, https://doi.org/10.2514/3.19713.

Schwartz, S. E., 2007: Heat capacity, time constant, and sensitivity of earth's climate system. *Journal of Geophysical Research*, **112 (D24)**, D24S05–D24S05, https://doi.org/10.1029/2007JD008746.

Sellers, W. D., 1969: A global climatic model based on the energy balance of the earth-atmosphere system. *Journal of Applied Meteorology (1962-1982)*, **8 (3)**, 392–400, https://doi.org/10.1175/1520-0450(1969)008⟨0392:AGCMBO⟩2.0.CO;2.

Sherwood, S. C., and Coauthors, 2020: An assessment of earth's climate sensitivity using multiple lines of evidence. *Reviews of Geophysics*, **58 (4)**, e2019RG000 678, https://doi.org/10.1029/2019RG000678.

Smith, C., and Coauthors, 2021: Figure and data generation for chapter 7 of the ipcc's sixth assessment report, working group 1 (plus assorted other contributions). Zenodo, https://doi.org/10.5281/zenodo.5211357.

Smith, S. W., 2003: *Chapter 15 - Moving Average Filters*, 277–284. Newnes, Boston, https://doi.org/10.1016/B978-0-7506-7444-7/50052-2.

Soden, B. J., R. T. Wetherald, G. L. Stenchikov, and A. Robock, 2002: Global cooling after the eruption of mount pinatubo: A test of climate feedback by water vapor. *Science*, **296 (5568)**, 727–730, https://doi.org/10.1126/science.296.5568.727.

Stratonovich, R. L., 1959: Optimum nonlinear systems which bring about a separation of a signal with constant parameters from noise. *Radiofizika*, **2 (6)**, 892–901.

Stratonovich, R. L., 1960: Application of the markov processes theory to optimal filtering. *Radio Engineering and Electronic Physics*, **5 (11)**, 1–19, https://doi.org/https://doi.org/10.1016/B978-1-4832-3230-0.50043-2.

Susskind, J., G. A. Schmidt, J. N. Lee, and L. Iredell, 2019: Recent global warming as confirmed by airs. *Environmental Research Letters*, **14 (4)**, 044 030, https://doi.org/10.1088/1748-9326/aafd4e.

Swerling, P., 1959: *First-Order Error Propagation in a Stagewise Smoothing Procedure for Satellite Observations*. RAND Corporation, Santa Monica, CA, URL https://www.rand.org/pubs/research_memoranda/RM2329.html.

Szopa, S., and Coauthors, 2021: *Short-Lived Climate Forcers*, book section 6, 817–922. Cambridge University Press, Cambridge, United Kingdom and New York, NY, USA, https://doi.org/10.1017/9781009157896.008.

Tebaldi, C., and R. Knutti, 2018: Evaluating the accuracy of climate change pattern emulation for low warming targets. *Environmental Research Letters*, **13**, https://doi.org/10.1088/1748-9326/aabef2.

Tebaldi, C., and Coauthors, 2021: Climate model projections from the scenario model intercomparison project (scenariomip) of cmip6. *Earth Syst. Dynam.*, **12 (1)**, 253–293, https://doi.org/10.5194/esd-12-253-2021.

Timmreck, C., and Coauthors, 2018: The interactive stratospheric aerosol model intercomparison project (isa-mip): motivation and experimental design. *Geosci. Model Dev.*, **11 (7)**, 2581–2608, https://doi.org/10.5194/gmd-11-2581-2018.

van Katwyk, P., B. Fox-Kemper, H. Seroussi, S. Nowicki, and K. J. Bergen, 2023: A variational lstm emulator of sea level contribution from the antarctic ice sheet. *Journal of Advances in Modeling Earth Systems*, **Submitted**.

van Vuuren, D. P., M. G. J. den Elzen, P. L. Lucas, B. Eickhout, B. J. Strengers, B. van Ruijven, S. Wonink, and R. van Houdt, 2007: Stabilizing greenhouse gas concentrations at low levels: an assessment of reduction strategies and costs. *Climatic Change*, **81 (2)**, 119–159, https://doi.org/10.1007/s10584-006-9172-9.

van Vuuren, D. P., and Coauthors, 2017: Energy, land-use and greenhouse gas emissions trajectories under a green growth paradigm. *Global Environmental Change*, **42**, 237–250, https://doi.org/10.1016/j.gloenvcha.2016.05.008.

Vernier, J., and Coauthors, 2011: Major influence of tropical volcanic eruptions on the stratospheric aerosol layer during the last decade. *Geophysical Research Letters*, **38**, https://doi.org/10.1029/2011GL047563.

Wan, E., and R. Van Der Merwe, 2000: The unscented kalman filter for nonlinear estimation. *Proceedings of the IEEE 2000 Adaptive Systems for Signal Processing, Communications, and Control Symposium (Cat. No.00EX373)*, 153–158, https://doi.org/10.1109/ASSPCC.2000.882463.

Wielicki, B. A., B. R. Barkstrom, E. F. Harrison, R. B. Lee, G. Louis Smith, and J. E. Cooper, 1996: Clouds and the earth's radiant energy system (ceres): An earth observing system experiment. *Bulletin of the American Meteorological Society*, **77 (5)**, 853–868, https://doi.org/10.1175/1520-0477(1996)077⟨0853:catere⟩2.0.co;2.

Wild, M., M. Z. Hakuba, D. Folini, P. DÃ¶rig-Ott, C. SchÃ¤r, S. Kato, and C. N. Long, 2019: The cloud-free global energy balance and inferred cloud radiative effects: an assessment based on direct observations and climate models. *Climate Dynamics*, **52 (7)**, 4787–4812, https://doi.org/10.1007/s00382-018-4413-y.

Wild, M., and Coauthors, 2015: The energy balance over land and oceans: an assessment based on direct observations and cmip5 climate models. *Climate Dynamics*, **44 (11)**, 3393–3429, https://doi.org/10.1007/s00382-014-2430-z.

Willner, D., C. B. Chang, and K. P. Dunn, 1976: Kalman filter algorithms for a multi-sensor system. *1976 IEEE Conference on Decision and Control including the 15th Symposium on Adaptive Processes*, 570–574, https://doi.org/10.1109/CDC.1976.267794.

Winton, M., K. Takahashi, and I. M. Held, 2010: Importance of ocean heat uptake efficacy to transient climate change. *Journal of Climate*, **23 (9)**, 2333–2344, https://doi.org/10.1175/2009JCLI3139.1.

Wunsch, C., 2020: Is the ocean speeding up? ocean surface energy trends. *Journal of Physical Oceanography*, **50 (11)**, 3205–3217, https://doi.org/10.1175/jpo-d-20-0082.1.

Wunsch, C., and P. Heimbach, 2007: Practical global oceanic state estimation. *Physica D: Nonlinear Phenomena*, **230 (1)**, 197–208, https://doi.org/10.1016/j.physd.2006.09.040.

Yang, S., Z. Li, J.-Y. Yu, X. Hu, W. Dong, and S. He, 2018: El niño-southern oscillation and its impact in the changing climate. *National Science Review*, **5 (6)**, 840–857, https://doi.org/10.1093/nsr/nwy046.

Yeager, S. G., and Coauthors, 2022: The seasonal-to-multiyear large ensemble (smyle) prediction system using the community earth system model version 2. *Geoscientific Model Development*, **15 (16)**, 6451–6493.

Zanchettin, D., and Coauthors, 2016: The model intercomparison project on the climatic response to volcanic forcing (volmip): experimental design and forcing input data for cmip6. *Geosci. Model Dev.*, **9 (8)**, 2701–2719, https://doi.org/10.5194/gmd-9-2701-2016.

Zanna, L., S. Khatiwala, J. M. Gregory, J. Ison, and P. Heimbach, 2019: Global reconstruction of historical ocean heat storage and transport. *Proceedings of the National Academy of Sciences*, **116 (4)**, 1126–1131, https://doi.org/10.1073/pnas.1808838115.

Zelinka, M. D., D. A. Randall, M. J. Webb, and S. A. Klein, 2017: Clearing clouds of uncertainty. *Nature Climate Change*, **7 (10)**, 674–678, https://doi.org/10.1038/nclimate3402.

Zhang, A., and M. M. Atia, 2020: An efficient tuning framework for kalman filter parameter optimization using design of experiments and genetic algorithms. *Navigation: Journal of the Institute of Navigation*, **67 (4)**, 775–793, https://doi.org/10.1002/navi.399.

Zhu, J., and Coauthors, 2022: Lgm paleoclimate constraints inform cloud parameterizations and equilibrium climate sensitivity in cesm2. *Journal of Advances in Modeling Earth Systems*, **14 (4)**, e2021MS002 776, https://doi.org/10.1029/2021MS002776.

SUPPLEMENT TO

# Efficient Estimation of Climate State and Its Uncertainty Using Kalman Filtering with Application to Policy Thresholds and Volcanism

J. Matthew Nicklas,[a] Baylor Fox-Kemper,[a] Charles Lawrence.[a]

[a] *Brown University, Providence, Rhode Island.*

*Corresponding author*: J. Matthew Nicklas, john_nicklas@brown.edu

## *Section A: Derivation of EBM-KF*

### *A1: Individual Functional Parts and Derivation*

$(\frac{1}{4}G_{SC})_t$ is the total solar irradiance (TSI) normalized to the Earth's surface area at ~1360 W/m$^2$ / 4 = 340.2 W/m$^2$ . Estimates of this normalized total solar irradiance indicate that it has varied since 1850 between 340.06 W/m$^2$ and 340.49 W/m$^2$ according to the Naval Research Laboratory 2 solar irradiance model (NRLTSI2_v02r01 (Coddington, Lean et al. 2017)). Within the hindcast EBM-KF model these NRL2 estimates were used, but this had a negligible effect on the model results compared to a constant $\frac{1}{4}\overline{G_{SC}}$ =340.2 W/m$^2$ value.

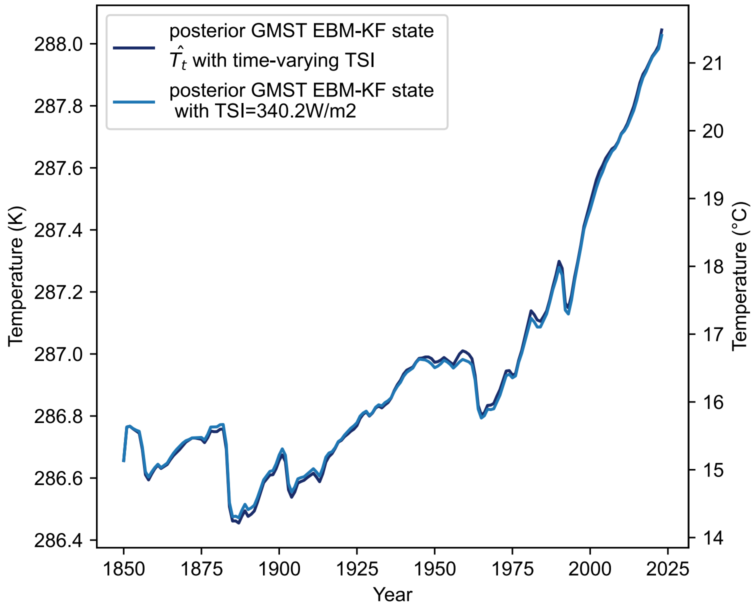


Supp. Fig. 1: Comparisons of the used EBM-Kalman Filtered climate state with time-varying total solar irradiance (navy blue) with an EBM-Kalman Filtered climate state with constant solar irradiance (light blue) set at 340.2 W/m$^2$. These differed by at most 0.028°C in 1960.

$\tilde{d}(t)$ is the prescribed shortwave radiation attenuation due to volcanic dust, the direct radiative effect of anthropogenic aerosols, and non-cloud atmospheric effects. This stochastically varying quantity can be calculated from the (unitless) stratospheric optical depth $AOD_n$ (Sato, Hansen et al. 1993; Vernier, Thomason et al. 2011), according to the formula given by Harshvardan and King (1993; Schwartz, Harshvardhan et al. 2002). (g=0.853 is the middle of the given range). The $AOD_t$ values used are forcings for the GISS climate model from 1850 – 1978 (https://data.giss.nasa.gov/modelforce/strataer/tau.line_2012.12.txt, $AOD_n$ at 550nm) and globally averaged measurements from the GloSSAC_V2.21 satellite measurement product (Nasa/Larc/Sd/Asdc 2018) from 1979 – 2022 (https://asdc.larc.nasa.gov/project/GloSSAC/GloSSAC_2.21, $AOD_t$ at 525nm). These wavelengths are at the shorter end of the 0.25-4 μm range of incoming solar shortwave energy $\mathcal{F}_{SW}$ , allowing satellites to detect dust reflectance. As the CALIPSO satellite mission ended in 2023, the year 2023 was extrapolated from a linear trend of the $AOD_t$ values from 2025-2022.

$$\tilde{d}(t)=\frac{4/3}{AOD_t*(1\text{-}g)+2q'},\quad g\in[0.834 - 0.872],\ q' = 0.715 \tag{SA1}$$

$$\tilde{d}(t)\approx\frac{9.068}{AOD_t+9.73} \tag{SA2}$$

Utilizing the equation above to calculate the dry-atmosphere reflected energy during a relatively aerosol-free period (2000-2005), when the aerosol optical depth was about 0.002m:

$$\mathcal{F}_{SW}{}^{refl\ by\ dryatm}_{clearsky} = \frac{1}{4}\overline{G_{SC}} * (1 - \tilde{d}(2002)) = 340.2\frac{W}{m^2}\left(1-\frac{9.07}{0.002+9.73}\right) = 23.1\frac{W}{m^2} \tag{SA3}$$

This value agrees with the clear-sky reflected energy (53 [52-55] W/m$^2$) minus reflected surface energy (33 [31-34] W/m$^2$), of 20 [18-24] W/m$^2$ reported by Wild, Hakuba et. al. (2019). Furthermore, the measured and inferred aerosol optical depth measurements already include those contributions from the anthropogenic sources.

$f_{\alpha A}(T,t)$ is the additional atmospheric shortwave attenuation due to cloud albedo, while $f_{\alpha S}(T)$ is the surface shortwave attenuation due to ground albedo. A portion of this varying cloud albedo is direct thermal feedback, whereas another portion is due to cloud seeding by anthropogenic aerosols $AC_t$. To contain the EBM model's complexity, the changing ground albedo is assumed to be only thermal feedback: the shortwave aspect of land use changes are neglected. Taken together, these two terms and $\tilde{d}(t)$ yield an overall absorption of 0.707 as measured from March 2000 to February 2005 by the CERES satellite (Wielicki, Barkstrom et al. 1996; Loeb, Wielicki et al. 2009), or equivalently a top-of-atmosphere, all-sky albedo of 0.293. Decomposition of this overall albedo into its clear-sky component (0.153) yields a ground * dry atmosphere absorption fraction of 0.847.

$$0.847 = \widetilde{\mathrm{d}_{2002}} * f_{\alpha S}(\mathrm{T}_{2002}) = 0.932 \ * f_{\alpha S}(\mathrm{T}_{2002}), \quad \text{thus} \quad f_{\alpha S}(\mathrm{T}_{2002})=0.909 \qquad \text{(SA4)}$$

$$0.707=\widetilde{\mathrm{d}_{2002}} * f_{\alpha A}(\mathrm{T}_{2002}, 2002) * f_{\alpha S}(\mathrm{T}_{2002}) = 0.847 * f_{\alpha A}(\mathrm{T}_{2002}, 2002),$$

$$\text{thus,} \quad f_{\alpha A}(\mathrm{T}_{2002}, 2002)=0.834 \qquad \text{(SA5)}$$

Verifying the reflected energies:

$$\mathcal{F}_{\mathrm{SW}}{}_{clearsky}^{refl\ by\ gnd} = \frac{\overline{G_{SC}}}{4} * \tilde{\mathrm{d}}(2002) * \left(1\text{-}f_{\alpha S}(\mathrm{T}_{2002})\right)$$

$$= 340.2\frac{W}{m^2} * 0.932 * 0.091 = 28.8\frac{W}{m^2} \qquad \text{(SA6)}$$

$$\mathcal{F}_{\mathrm{SW}}{}_{allsky}^{refl\ by\ gnd} = \frac{\overline{G_{SC}}}{4} * \tilde{\mathrm{d}}(2002) * f_{\alpha A}(\mathrm{T}_{2002}, 2002) * \left(1 - f_{\alpha S}(\mathrm{T}_{2002})\right) = 24.1\frac{W}{m^2} \ \text{(SA7)}$$

$$\mathcal{F}_{\mathrm{SW}}{}_{allsky}^{refl\ by\ clouds} = \frac{\overline{G_{SC}}}{4} * \tilde{\mathrm{d}}(2002) * \left(1 - f_{\alpha A}(\mathrm{T}_{2002}, 2002)\right) = 52.6\frac{W}{m^2} \ \text{(SA8)}$$

There is a slight discrepancy in the clear-sky ground-reflected energy relative to the literature value (33 [31-34] W/m$^2$), but the all-sky reflected energies are much more closely aligned: the ground reported value is 25 [23-26] W/m$^2$, and the dry atmosphere + cloud reported value is 75 [71-77] W/m$^2$, compared to this inferred value of 52.6 + 24.1 = 76.7 W/m$^2$ (Wild, Folini et al. 2015). Note that this shortwave flux equation does not consider shortwave energy absorbed into the atmosphere, a substantial simplification.

$\mathrm{j}^{\star}(T_t) = \sigma_{\mathrm{sf}} T_t^4$ is the ideal black body radiation or Planck feedback, which derives from quantum mechanics, particularly the Stefan-Boltzmann law (Boltzmann 1884), which gives the Stefan-Boltzman constant $\sigma_{\mathrm{sf}} = 5.670\ 10^{-8}\mathrm{Wm}^{-2}\mathrm{K}^{-4}$ as a coefficient. This symbol $\mathrm{j}^{\star}$ is not used in the main text, only here in Supplement A. For the Earth, because the temperature is in the neighborhood of 287K, this black body radiation is primarily in the infrared spectrum, between 200 and 1200 cm$^{-1}$ (Zhong and Haigh 2013).

$\tilde{\mathrm{g}}(t)$ is the prescribed longwave attenuation due to $CO_2$ and other anthropogenic greenhouse gases ($CH_4$, $NO_2$, $O_3$, halogens), which is half of the fraction of radiative energy absorbed by those gases (because half is re-emitted upwards and half downwards). This absorbed, downwards-emitted fraction increases linearly by a factor of $\beta_0$ with respect to the logarithm of the $CO_2$ concentration measured in ppm (see Figure 6b of (Zhong and Haigh 2013)). $CO_2$ concentrations were taken as the historical concentrations used in the NASA GISS climate model 1850-1979 (https://data.giss.nasa.gov/modelforce/ghgases/Fig1A.ext.txt) and the NOAA global averages from 1980-2021 (https://gml.noaa.gov/webdata/ccgg/trends/co2/co2_annmean_gl.txt).

$$\phi_{\mathrm{LW}}(\mathrm{out}) = \mathrm{j}^\star(T_t) - \frac{\phi_{\mathrm{LW}}(\mathrm{absorbed})}{2} = \mathrm{j}^\star(T_t) * \tilde{g}(t) \ * f_{H2O}(T_t) \quad \text{(SA9)}$$

$$\tilde{g}(t) * f_{H2O}(T_t) = \left(1 - \frac{\phi_{\mathrm{LW}}(\mathrm{CO2\ absorb})}{2\,\mathrm{j}^\star(\mathrm{T_t})}\right) * \left(1 - \frac{\phi_{\mathrm{LW}}(\mathrm{H2O\ absorb})}{2\,\mathrm{j}^\star(\mathrm{T_n})}\right) \approx \left(1 - \frac{\phi_{\mathrm{LW}}(\mathrm{CO2\ absorb}) + \phi_{\mathrm{LW}}(\mathrm{H2O\ absorb})}{2\,\mathrm{j}^\star(\mathrm{T_t})}\right) \quad \text{(SA10)}$$

$$\tilde{g}(t) = 1 - \beta_0 \log_{10}([\mathrm{eCO_2}]_\mathrm{t}) < 1 \quad \text{(SA11)}$$

Equation SA9 refers to a single-layer atmosphere assumed by prior researchers such as Kravitz, Rasch, et. al. (2018). While the technically correct separation of SA9 is shown on the right hand side of SA10, the form for the product of $\tilde{g}(t) * f_{H2O}(T_t)$ was chosen specifically to resemble the previous shortwave energy expressions, essentially representing $CO_2$ in an atmospheric layer above $H_2O$ (sequential filtering in the middle expression of SA10). Relating these two representations demands the simplification that both the longwave radiative fluxes absorbed by $CO_2$ and $H_2O$ are each smaller than twice the total ground-emitted longwave radiative flux, so their product is yet smaller and can be neglected. Indeed, for $CO_2$ this ratio $\frac{\phi_{\mathrm{LW}}(\mathrm{CO2\ absorb})}{2\,\mathrm{j}^\star(\mathrm{T_t})} = \beta_0 \log_{10}([\mathrm{CO_2}]_\mathrm{t})$ is in the range [0.165 - 0.176] and for $H_2O$ the analogous ratio is in the range [0.250 - 0.259] so their product (the difference between the RHS and LHS of A12) is at most 0.045. This difference in energy flux would be large enough to cause significant inaccuracies in the energy balance model (larger than the anthropogenic global warming signal), should parameters from a single-layer atmosphere be used in a sequential filter model. Thus, the critical parameters $\beta_0$ and $\beta_1$ must be calculated within the framework of the chosen model (here a sequential filter – see below), after which this distinction only matters to the higher-order terms of the deviations from the preindustrial energy flux (0.176-0.165) * (0.259-0.250) ≈ 0.0001, a negligible fraction.

More complex functions for $\tilde{g}(t)$ exist involving functions for each individual greenhouse gas (Meinshausen, Nicholls et al. 2020) but for the purposes of simplifying this energy balance model, only one "effective greenhouse" concentration is used. Our "effective greenhouse gas concentration" includes $CH_4$, $N_2O$, $O_3$, contrails, stratospheric water vapor, land use, and black carbon on snow but excluding anthropogenic atmospheric aerosols (Forster, Smith et al. 2023). Formally, land use and black carbon on snow should be included as a prescribed change to the $f_{\alpha S}$ function on the shortwave side but in combination these two amount to within -0.15 W/m$^2$, less in absolute value than all the other aforementioned "combined greenhouse forcing" components aside from contrails and stratospheric water vapor. Similarly, the prescribed contribution of stratospheric water vapor should formally be within the $f_{H2O}(T_t)$ function not lumped with the other greenhouse gases, but as this represents only 0.05 W/m$^2$ at most, this is inconsequential (variations in incoming solar insolation are of a similar magnitude). We determined the "effective CO2 concentration" by first fitting a function relating CO2 concentrations reported above to the CO2 radiative forcings reported by Forster (2023) at https://github.com/ClimateIndicator/forcing-timeseries/tree/main/output.

$$\phi_{LW}^{CO2} = 12.74 \ \log_{10}([eCO_2]_t) - 31.55 \quad \text{(SA12)}$$

Then by summing all "effective greenhouse gas" reported energy fluxes, the above function was inverted to determine the "effective CO2 concentration." These ranged from 278 ppm (or $\log_{10}([\mathrm{eCO_2}]) = 2.444$ when there was no "effective greenhouse gas" energy flux to 558.7ppm or $\log_{10}([\mathrm{eCO_2}]) = 2.747$ in 2022, the last date of this timeseries. Within this timeseries, the datapoint corresponding to the year 2023 was not yet published at the time of this study's publication, but was inferred from a linear projection of the ratio between Mona Loa $CO_2$ concentrations since 2000 (https://gml.noaa.gov/webdata/ccgg/trends/co2/co2_annmean_mlo.txt) and recent eCO2 concentrations (563.4 ppm = $[\mathrm{eCO2}]_{2023} \approx 1.34 * [\mathrm{MLo}\ CO_2]_{2023}$).

$f_{H2O}(T_t)$ is the additional atmospheric longwave attenuation due to water vapor and other gasses, including both lapse rate and relative humidity. The precise functional form of this feedback function is unknown, as is the functional form of the two shortwave feedbacks, partially due to disagreements between paleoclimate inferences and ESMs. We thus introduced the following 3 functions, which incorporate an additional 3 positive $\beta$ coefficients and 1 exponent η. (Note $f_{H2O}(T_t)$ can be either linearized into a form like these other feedbacks or rewritten in the $(1- \frac{\phi_{LW}(\mathrm{H2O\ absorb})}{2\, j^{*}(T_t)})$ form.)

$$f_{H2O}(T_t) \doteq \beta_1 (1/T_t)^{\eta} \approx 1\text{-}\left(1+\beta_1 (T_{2002})^{-\eta} - \beta_1 \eta (T_{2002})^{-\eta\text{-}1} (T_t\text{-}T_{2002})\right) \quad \text{(SA13)}$$

$$f_{\alpha A}(T_t) \doteq 0.834 \left(1+\beta_2 (T_t\text{-}T_{2002})\right) + \frac{AC_n - AC_{2002}}{\frac{G_{SC}}{4}\widetilde{\mathrm{d}_{2002}}} \quad \text{(SA14)}$$

$$f_{\alpha S}(T_t) \doteq 0.909 \left(1+\beta_3 (T_t\text{-}T_{2002})\right) \quad \text{(SA15)}$$

Finally returning to the heat flux between the surface and the deeper layer of the ocean, other researchers have modeled this $Q_{\text{surf-deep}}$ as a simple thermal conductivity $\gamma$ multiplied by the difference in deviation temperatures between the surface ($\Delta T_t - \Delta \theta_t$), with these deviations measured relative to the pre-industrial equilibrium.

$$Q_{surf-deep} = \gamma * (\Delta T_t - \Delta \theta_t) = \gamma * (\mathrm{T_t} - \theta_t - \mathrm{T}_{1850} + \theta_{1850}) \quad \text{(SA16)}$$

If we take $T_{1850}$ = 286.66K = 13.51°C and $\theta_{1850}$ = 276.66K = 3.51°C, then $\zeta_0 = 10\text{K}$. This consistent equilibrium temperature difference exists because the ocean is temperature stratified. We used $\gamma$ from the CMIP5 reported by Geoffroy et al. Part II (2013) to be 0.67±0.15 W/m$^2$/K. Estimates of $\gamma$ from the CMIP6 coupled model comparison project were almost unchanged, 0.64±0.14 W/m$^2$/K (Hall and Fox-Kemper 2023). The deep ocean heat content record was extended back from 1850-1869 by prepending zero values. Since this is an equilibrium value, the deviation from the equilibrium deep ocean temperature $\theta_{1850}$ = 276.66K is given by the deviation from this baseline heat content.

The ocean heat content anomaly is obtained from Zanna (Zanna, Khatiwala et al. 2019) from 1870-2018. Before 1870, the OHCA was set to 0, with a standard deviation taken to be the 1870-1889 average: 50.2 ZJ. After 2018, the standard deviation was continued as the 2009-2018 average of 25.2ZJ. The additional increase in OHCA after 2018 was provided from a separate NCEI dataset (Levitus, Antonov et al. 2017). This NCEI dataset disagrees with the Zanna, Khatiwala et al. (2019) dataset regarding the change in OHCA from 2005-2018 by a factor of 1.71. NCEI reports 134.2ZJ compared to Zanna (Zanna, Khatiwala et al. 2019) reporting 78.5ZJ. However, the NCEI dataset is more directly derived from observations, especially the Argo array of autonomous floats, and thus is preferred when that array has been fully available.

### *A2: Solving for unknown β coefficients:*

Following the definition of climate feedback of w as ∂*N*/∂w * dw/dT, where *N* is the TOA radiative flux (the entire EBM model), we equated the climate feedbacks of each of the three *f?* feedback functions and the Planck response $j^{\star}$, with the values (in $W/m^2/K$) reported in Table 7.10 and Figure 7.10 of AR6 (Forster, Storelvmo et al. 2021).

$$\frac{\partial N}{\partial j^{\star}} * \frac{d\,j^{\star}}{dT_t} = -\tilde{g}(t) * f_{H2O}(T_t) * 4\sigma_{sf}(T_t)^3 = -3.22 \quad \text{(SA17)}$$

$$\frac{\partial N}{\partial f_{H2O}(T_t)} * \frac{d f_{H2O}(t)}{dT_t} = -j^{\star}(T_t) * \tilde{g}(t) * -\beta_1 \eta (T_t)^{-\eta-1} = 1.30 \quad \text{(SA18)}$$

$$\frac{\partial N}{\partial f_{\alpha A}(T_t)} * \frac{d f_{\alpha A}(T_t)}{dT_t} = 340.2 * \tilde{d}(t) * f_{\alpha S}(T_t) * 0.834\,\beta_2 = 0.35 \quad \text{(SA19)}$$

$$\frac{\partial N}{\partial f_{\alpha S}(T_t)} * \frac{d f_{\alpha S}(T_t)}{dT_t} = 340.2 * \tilde{d}(t) * f_{\alpha A}(T_t) * 0.909\,\beta_3 = 0.42 \quad \text{(SA20)}$$

Solving for the exponent by taking the ratio of the first two equations yielded η =1.615. Furthermore, based on the CERES measurements from 2000-2005, everything to the left of both $\beta_2$ (SA19) and $\beta_3$ (SA20) is the overall absorbed SW irradiance of 340.2*0.707=240.5 $W/m^2$, so $\beta_2 = 0.00136\ K^{-1}$ and $\beta_3 = 0.00163\ K^{-1}$.

Figure 3.3 from Zhong and Haigh (2013) shows that per log10 order of magnitude of [CO2] increase, an additional 15.45 $W/m^2$ is absorbed. However, in Forster (2023), the "greenhouse gas" absorption increases by 12.74 $W/m^2$ per log10 order of magnitude of effective [CO2] increase (eq. SA12). This measurement approximating a partial derivative was presumably made recently, so we used the more recent 2002 temperature of ~287.5K (14.4°C), but this choice is relatively inconsequential: $\beta_0\beta_1$ would be only 0.66% larger if the pre-industrial temperature was used instead. In the pre-industrial climate, we assumed a steady-state equilibrium with a constant black body temperature of 286.66K (13.6°C) and a log10([effective CO2]) ≈ 2.444. This allows us to solve for $\beta_0$ and $\beta_1$ as follows:

$$12.74 = \frac{\partial N}{\partial \tilde{g}_n} * \frac{d\,\tilde{g}_n}{d\,\log_{10}([eCO_2]_n)} = -\sigma_{sf}(T_n)^4 \beta_1 (T_n)^{-1.615}(-\beta_0) \quad \text{(SA21)}$$

$$307.11 = \beta_1\beta_0 \quad \text{using} \quad T_{2002} = 287.55 \quad \text{(SA22)}$$

$$0 = 340.2 * \widetilde{d_{1850}} * f_{\alpha A}(T_{1850}) * f_{\alpha S}(T_{1850}) - \sigma_{sf}(T_{1850})^4 \beta_1 (T_{1850})^{-1.615}\left(1 - \beta_0(2.444)\right) \quad \text{(SA23)}$$

$$240.53 = \sigma_{sf}(286.66)^{2.385}(\beta_1)\left(1 - \beta_0(2.444)\right) \quad \text{(SA24)}$$

$$5841.77 = (\beta_1)\left(1 - \beta_0(2.444)\right) \quad \text{(SA25)}$$

$$6592.345 \approx \beta_1 \quad \text{and} \quad 0.046585 \approx \beta_0 \quad \text{(SA26)}$$

Checking that Planck partial derivative is accurate, we obtained a value for climate sensitivity of $j^{\star}$ to be -3.34 $W/m^2/K$ at current conditions and the sensitivity of $f_{H2O}$ to be 1.35 $W/m^2/K$, within the likely range of AR6. With an instantaneous doubling or quadrupling of $CO_2$ the sensitivity of $j^{\star}$ becomes -3.30 $W/m^2/K$ or -3.22 $W/m^2/K$ respectively, matching the reported value. Because they were defined to have proportional climate sensitivities, $f_{H2O}$ exactly matches AR6 in a $4xCO_2$ scenario, with 1.30 $W/m^2/K$.

***Section A3: RTS Smoother***

$$\hat{\hat{\mathbf{K}}}_t = \mathbf{P}_t \mathbf{\Phi}_t (\mathbf{P}_{t|t-1})^{-1} \quad \text{back-updated Kalman gain} \quad \text{(SA26)}$$

$$\hat{\hat{\mathbf{x}}}_t = \hat{\mathbf{x}}_t + \hat{\hat{\mathbf{K}}}_t \left(\hat{\hat{\mathbf{x}}}_t - \mathbf{F}(\hat{\mathbf{x}}_t; u_{t+1})\right) \quad \text{back-updated state estimate} \quad \text{(SA27)}$$

$$\hat{\hat{\mathbf{P}}}_t = \mathbf{P}_t + \hat{\hat{\mathbf{K}}}_t (\hat{\hat{\mathbf{P}}}_{t+1} - \mathbf{P}_{t|t-1})\, \hat{\hat{\mathbf{K}}}_t^{\mathrm{T}} \quad \text{back-updated state covariance} \quad \text{(SA28)}$$

This RTS has a theoretical advantage of blending abrupt changes in the model state over greater time periods, while also slightly reducing the state covariance. For instance, if the measurements suddenly and persistently diverged from the blind, forward EBM (unrelated to a known volcanic eruption), an EBM-Kalman Filter model state would only react as these measurements diverge, whereas an EBM-RTS would slightly foreshadow this jump because it can see future as well as past measurements. This occurred in 1900: even though the EBM-KF estimated state is trending up, the EBM-RTS state moves cooler to reflect the colder GMST measurements from 1902-1907, colder than the EBM predicted from the Santa Marina volcanic eruption alone (see Supp. Fig. 2). Generally, the EBM-RTS just provides a second "nudge" toward measurements. However, for the purposes of this paper, these distinctions make little difference between $\hat{\hat{\mathbf{x}}}_t$ and $\hat{\mathbf{x}}_t$, as is demonstrated in Supp. Fig. 1 below.

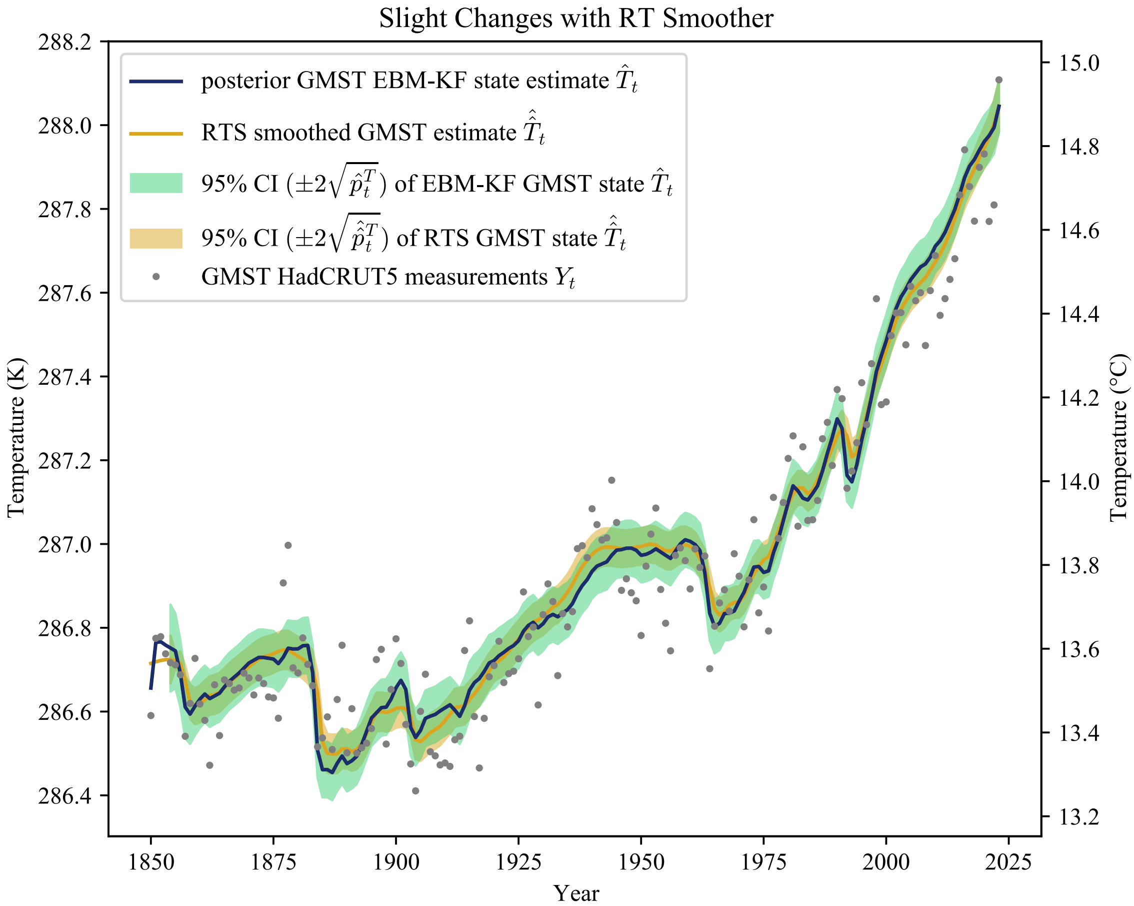


Supp. Fig. 2: Comparisons of the original EBM-Kalman Filtered climate state (navy blue line with green 95% uncertainty window) with an EBM-RTS climate state (orange line with orange 95% uncertainty window). Note that the temperatures on y-axis are zoomed in relative to all other figures to demonstrate these minute differences. From 1905-1930 and 2000-2020 when there are repeated cooler GMST temperature measurements than the EBM-KF state prediction, the EBM-RTS climate state doubly takes these annual temperature measurements into account, so it has a greater cooling deflection in these periods. Other years are warmer in the EBM-RTS than the EBM-KF climate state, although even these differences are slight - at most 0.1K during years of volcanic activity. However, there is greater certainty in the state estimate with the EBM-RTS: $\hat{\hat{\mathbf{P}}}_t$ shrinks relative to $\mathbf{P}_t$ (see Supp. Fig. 10) by factors of 2.25 and 2.84 for the GMST ($\hat{p}_t^T$) and OHCA ($\hat{p}_t^H$) components respectively (everywhere except at the start and tail end of the timeseries). The off-diagonal heat-transfer uncertainty component of $\hat{\hat{\mathbf{P}}}_t$ is negative and 29 times smaller than those of $\mathbf{P}_t$.

237 ***Section B: Alternative Definitions of the Climate State***

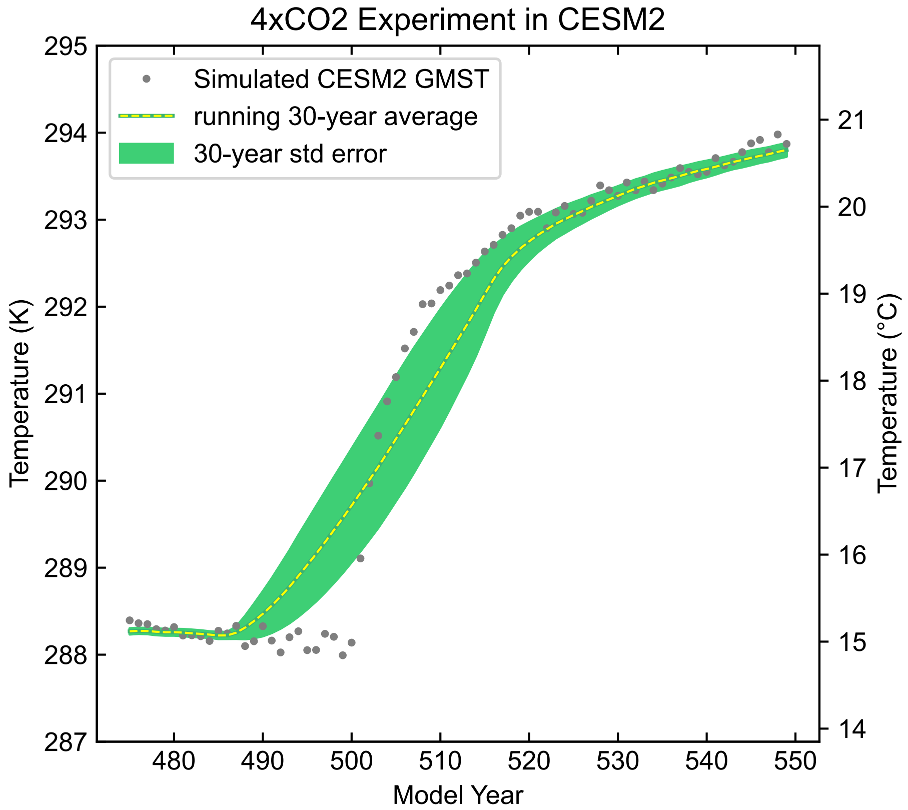


238
239 Supp. Fig. 3: In this modeling experiment conducted within CESM2, the CO2 concentration
240 was instantaneously quadrupled at year 500. The resulting modeled GMST values are plotted
241 in grey, along with their 30-year running mean (yellow dashed), and the standard error of this
242 mean (green window). The 30-year running average anticipates the jump for 15 years before
243 CO2 even began to increase, so that the 30-year average "climate" is several °C away from
244 the simulation year 500 temperatures. Then, it fails to increase at the appropriate rate, such
245 that a period of 6 years (505-511) is hotter than the 30-year running average's 95%
246 confidence interval. Only by simulation year 520 does the 30-year running average appear
247 visually to catch up and visually correspond with the simulated temperatures.

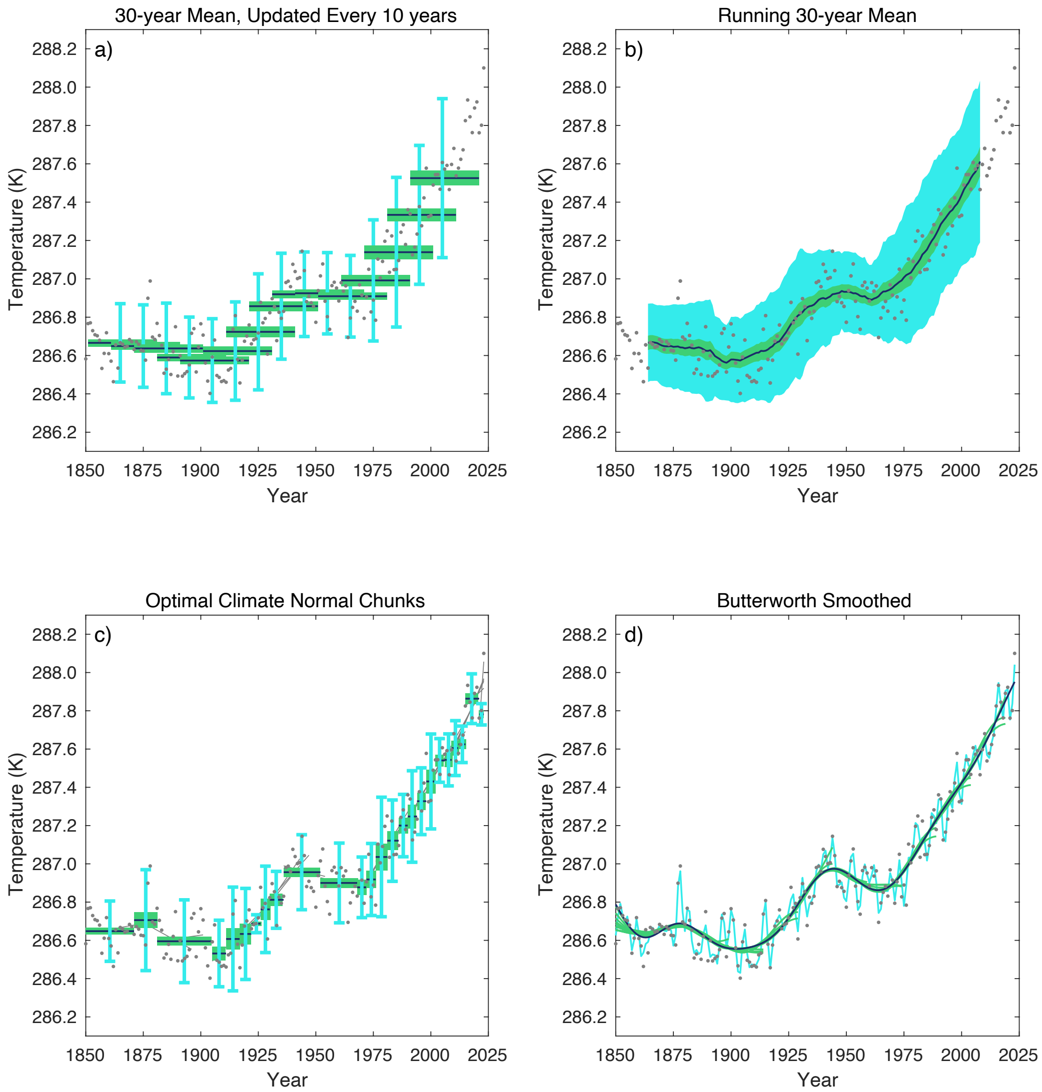


Supp. Fig. 4: Comparison of Prior Methods for Filtering or Smoothing the Climate as applied to the HadCRUT5 temperature dataset. (Morice, Kennedy et al. 2021) All metrics analogous to standard deviation are plotted at the 2σ level in light blue, and all metrics analogous to the standard error are plotted at the 1σ level in light green. a) The 30-year climate normals, updated every 10 years as per the World Meteorological Association in 1935. b) A running 30-year average. c) Adaptive periods of multiyear averages, known as the optimal climate normal (OCN). (Livezey, Vinnikov et al. 2007). Chunks became smaller as the rate of climate change increased in recent decades. d) The Butterworth Smoother applied to this temperature dataset. (Mann 2008) For the “standard error” highly smoothed lines, the lowpass adaptive, lowpass mean padded, and lowpass methods were applied to chunks of the timeseries data ranging from 50 to 170 years in increments of 15 years with a cutoff frequency of 1/30years. The black “best” line a lowpass adaptive curve extended to 2021. The blue “standard deviation” line is a lowpass mean padded filter with a cutoff frequency of 1/5years.

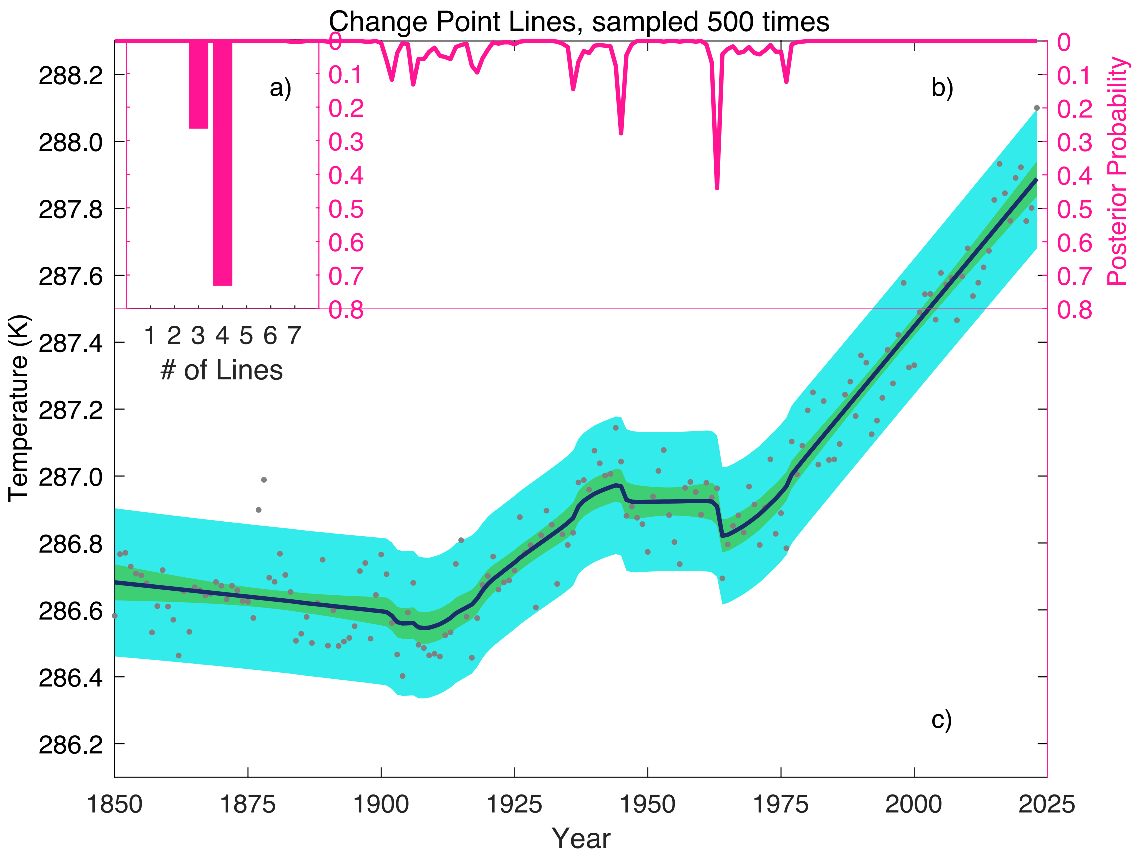


Supp. Fig. 5: Utilization of Bayesian Change Point on the HadCRUT5 data. (Ruggieri and Antonellis 2016) a) There are likely 4 trendlines with 72% of the posterior probability, and the remaining posterior probability on 3 trendlines. b) The posterior probability plot of where trendlines are most likely to occur: 51.2% of all samplings have a change point occur in 1963, and 26.4% of samplings have a change point occur in 1945. c) The posterior distribution of the trendlines in GMST, again with blue shading to indicate 2σ confidence interval of the data and green shading to indicate 2σ confidence interval of the mean trendline. These trend lines do not have to be continuous (note the dip at 1963), but over many samplings the average trend is smoothed.

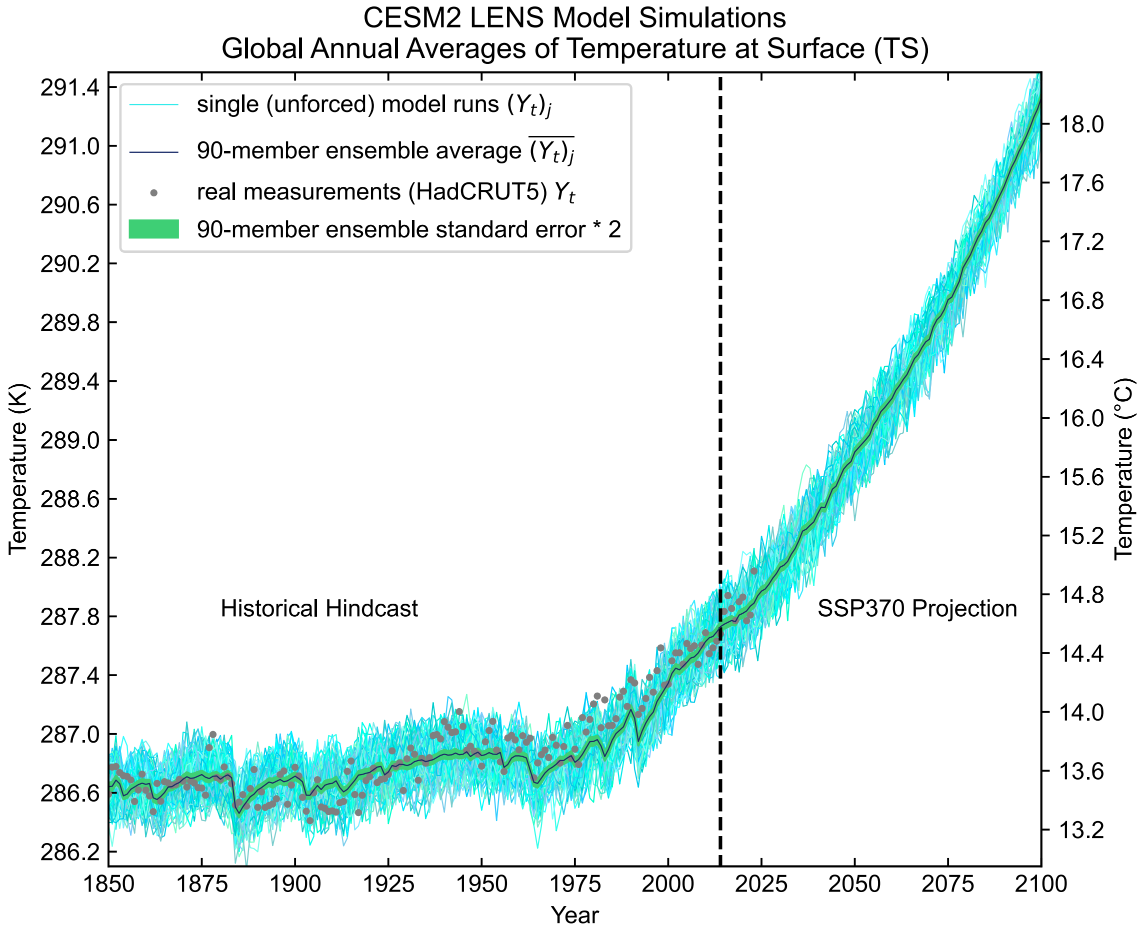


Supp. Fig. 6: Comparison of the CESM2 Large Ensemble (LENS2) GSAT (Rodgers, Lee et al. 2021) with HadCRUT5 GMST measurements. The various shades of thin light blue and turquoise lines represent each individual simulation $(Y_t)_j$ of the 90-member ensemble. The ensemble mean is plotted in a navy-blue line, and the ensemble mean standard error is plotted around this line in green. This standard error is twice the standard deviation divided by the square root of the number of ensemble members at that moment and shows the 2σ uncertainty in the yearly simulated climate is roughly 0.026K. The ensemble mean has $r^2 = 0.83$ relative to the HadCRUT5 measurements, lower than for the blind EBM ($r^2$=0.88). The dashed vertical line represents when LENS transitions from historical to future forcing (SSP3-7.0).

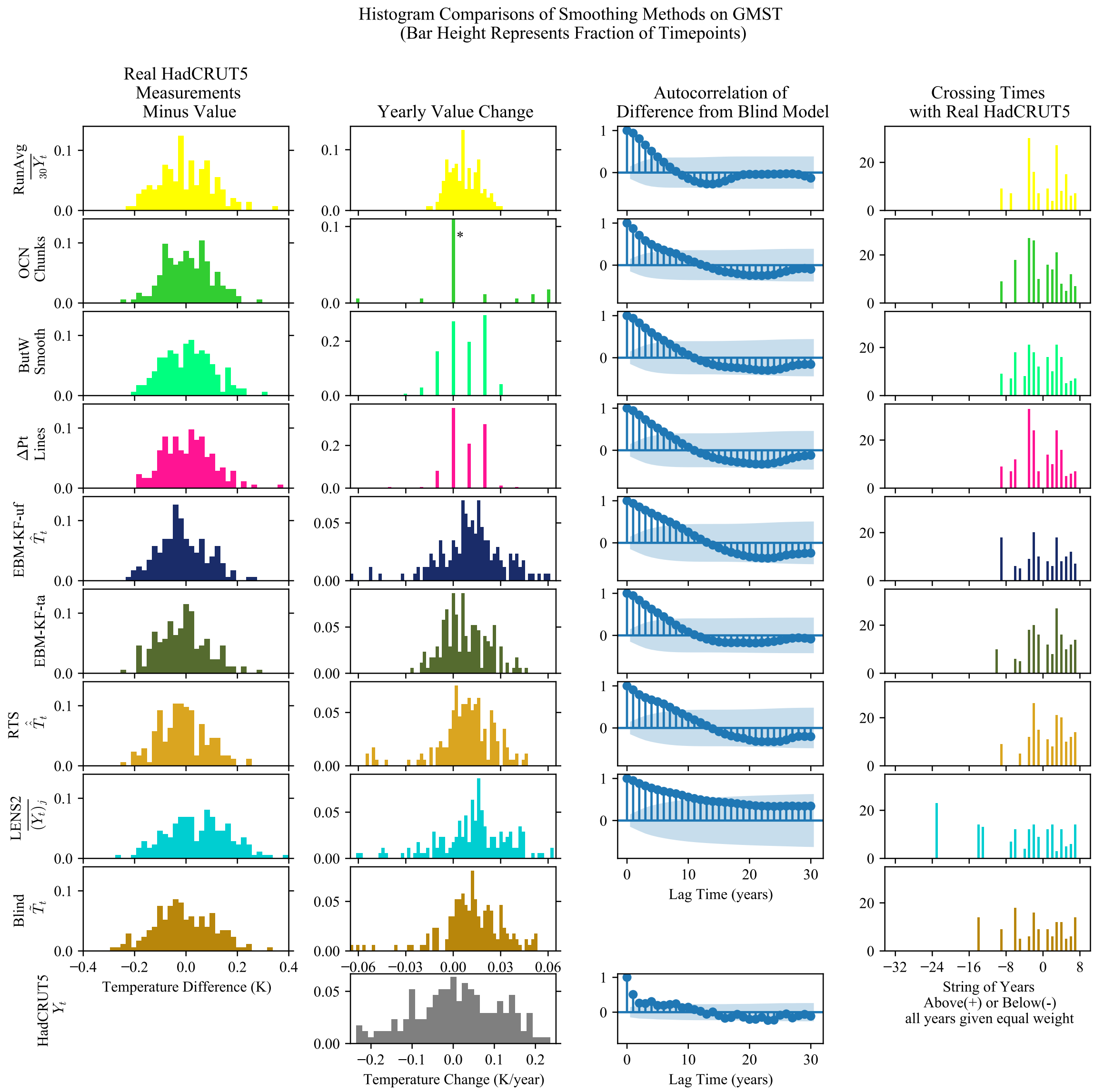


Supp. Fig. 7: Histogram comparisons of several aspects of many of the smoothing methods for generating a climate timeseries. The far-left column represents the absolute differences between the HadCRUT5 measurements and all the other models. All look similar in this respect. The center-left column shows the annual changes in the temperatures reported by each model. In this respect, the real HadCRUT5 measurements are the most spread out, because the stochastic change each year is large, whereas in most years the OCN Chunks do not change. The center-right column shows an autocorrelation plot, which demonstrates that every other model aside from HadCRUT5 (and to a lesser extent the running average) are autocorrelated with the blind energy-balance model to similar degrees. The far-right column shows how many continuous years are spent above or below HadCRUT5: both the LENS2 ensemble average and the blind energy-balance model had >20 year spans for which they were colder than the “real” HadCRUT5 data, illustrating the benefit of data assimilation.

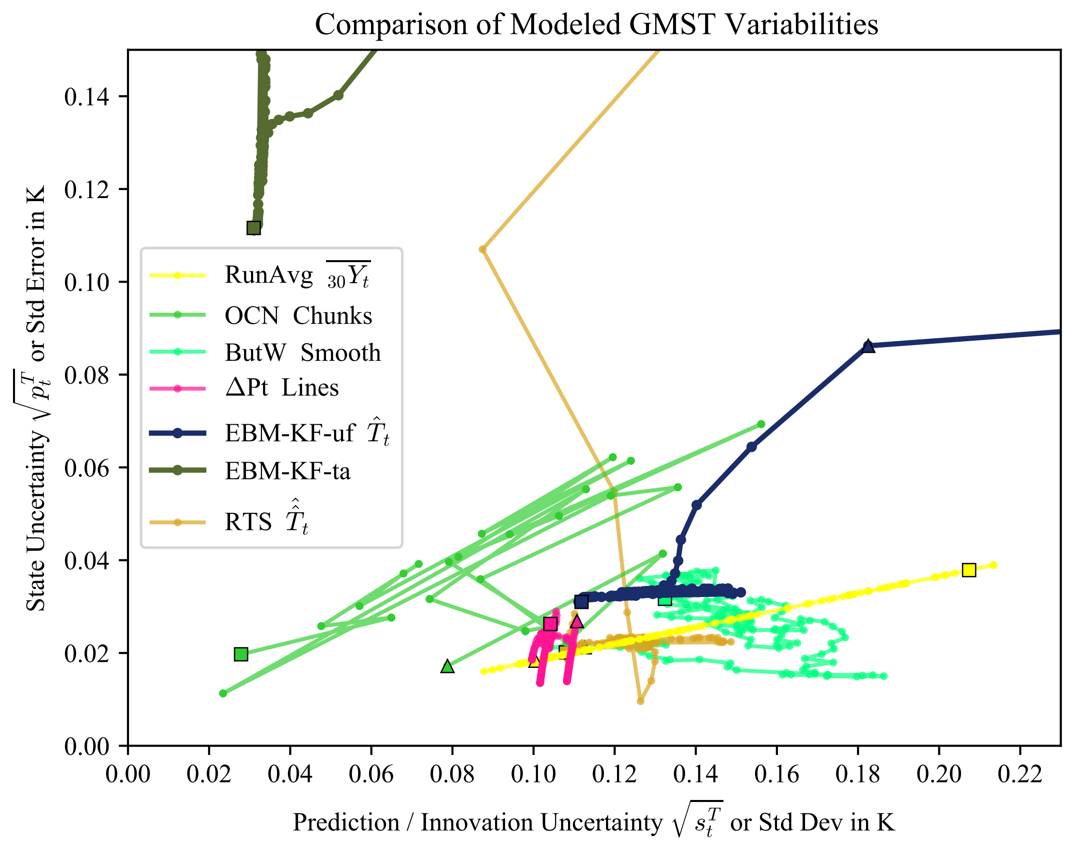


Supp. Fig. 8: Comparisons of the state and prediction (or equivalent) uncertainties of the smoothing methods for generating a climate timeseries. The x-axis represents the state uncertainty (colored light green in all other figures), and the y-axis represents the prediction uncertainty (colored light blue and doubled in all other figures). As these quantities change over time, all points in these smoothing timeseries are traced with colored lines, with the triangle △ representing the value of these quantities in 1850 or the first point that they entered the frame limits of this graph, and the square □ representing the value of these quantities in 2021 or the last point that they were within the frame limits. For instance, the running average draws a straight line because standard deviation and standard error are linearly correlated by a favor of 1/√30, and latter points have larger quantities for each variability due to the changing climate. The Butterworth Smoother traces a curve roughly in this region, with both the standard deviations and standard errors being twice the 15-year running average of the maximum of the absolute value of differences between colored and black curves. The EBM-KF-uf and RTS (uf) methods rapidly converge to an innovation uncertainty of 0.11-0.15K and state uncertainties of 0.034K and 0.023K respectively. The Change Point Regression variance also fluctuate the same region as the RTS, although change point method's standard error twice drops to 0.014K, and the prediction uncertainty is slightly smaller, 0.10-0.11K. Both the OCN and the LENS2 climates have standard errors that are above the other methods at most times. For LENS2, the standard deviation within the CESM2 ensemble generally remains between 0.11K and 0.14K, whereas the state uncertainty is taken to be the standard deviation of the 20 ensembles comprising CMIP6 in October 2021. (Meehl, Moss et al. 2014) These metrics are unrelated to Figure 10 in the main text. Within CMIP6, the 20 ensembles are closest to agreement in 1939, when the state uncertainty dipped down to only 0.029K between ensemble means, but this uncertainty was much greater at earlier and later time points, reaching 0.183K by 2014. The EBM-KF-ta trades prediction uncertainty (down to 0.031K) for larger state uncertainty (0.111K) relative to the EBM-KF-ta.

## ***Section C: Miscellaneous Additional Figures***

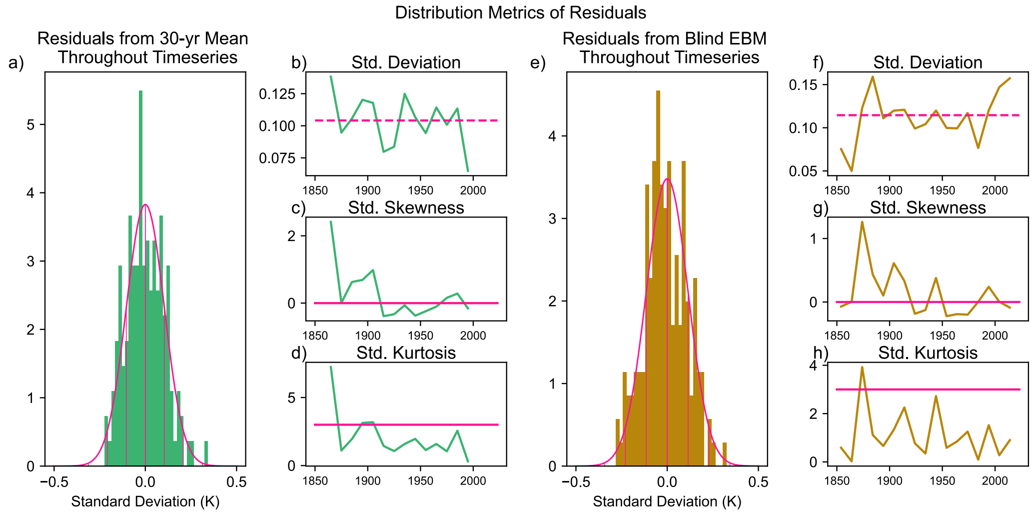


Supp. Fig. 9: Left panels show statistical features of the residuals between the HadCRUT5 measurements with respect to their 30-year running mean, which have a bias of -0.00339K. Pink lines in the histogram in (a) depict an ideal Gaussian distribution with standard deviation of 0.105K, and vertical lines drawn for each of these standard deviations. The dashed pink line (b) indicates the overall standard deviation. Solid pink lines for the skewness = 0.147 (c) and kurtosis = 1.904 (d) indicate the ideal values for a Gaussian distribution.
Right panels show statistical features of the differences between the HadCRUT5 measurements with respect to the blind EBM, which have a bias of -0.00104K. Pink lines in the histogram in (e) depict an ideal Gaussian distribution with standard deviation of 0.115K, and vertical lines drawn for each of these standard deviations. The dashed pink line (f) indicates the overall standard deviation. The skewness = 0.123 (g) and kurtosis = 1.208 (h) differ from the ideal values for a Gaussian distribution indicated by solid pink lines.

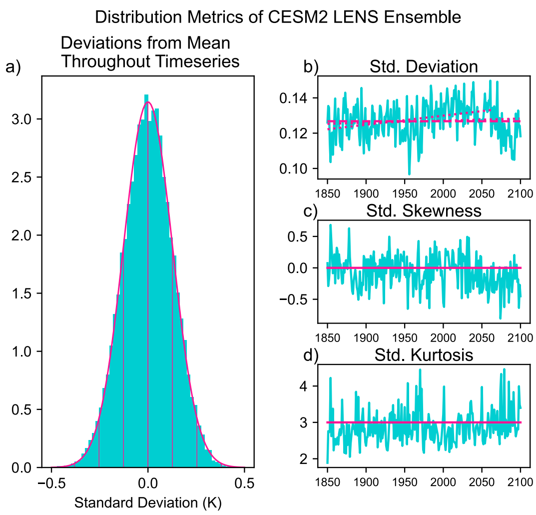


Supp. Fig. 10: Statistical Features of the CESM2 Large Ensemble. (Rodgers, Lee et al. 2021). Pink lines in the histogram in (a) depict an ideal Gaussian distribution with standard deviation of 0.127K, and vertical lines drawn for each of these standard deviations. The observed trend (b) up until 2065 ($p<0.001$) and overall ($p=0.168$) in the standard deviation over time is plotted in a dotted pink, while the dashed line indicates the overall standard deviation of 0.127K. The skewness = -0.069 (c) and kurtosis = 2.87 (d) differ from the ideal values for a Gaussian distribution indicated by solid pink lines.

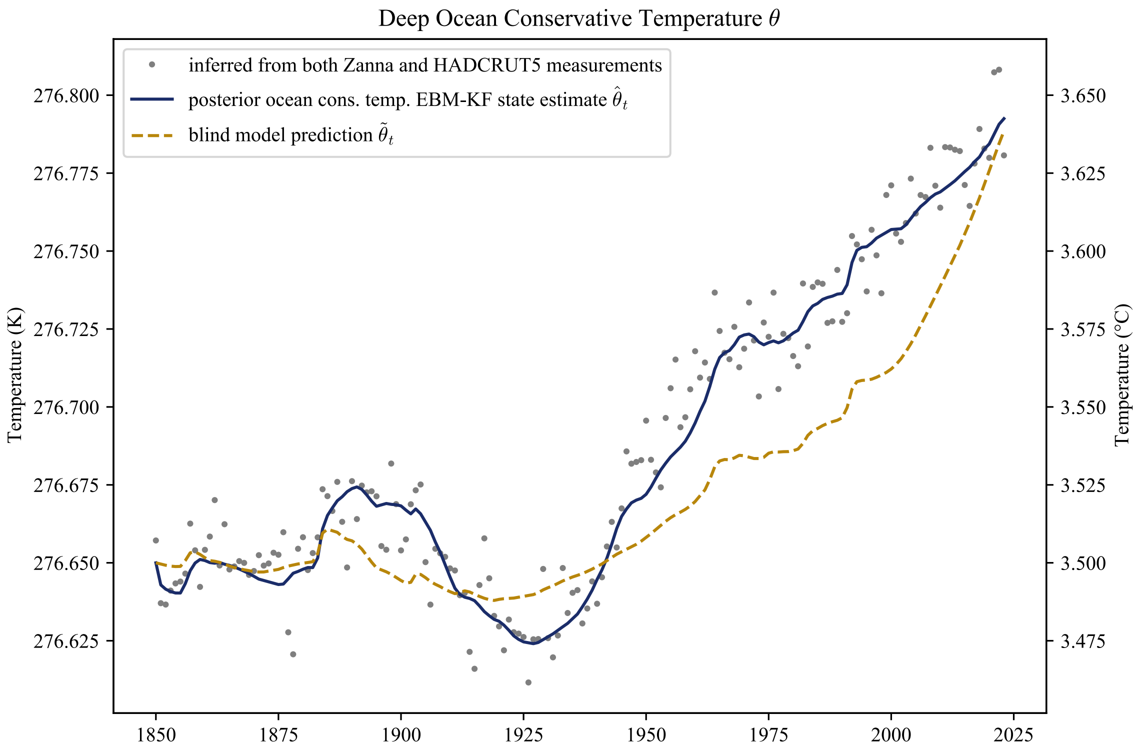


Supp. Fig. 11: As in Fig. 2, but regarding the deep ocean potential temperature. A comparison of the blind model EBM, the posterior Extended Kalman Filter state estimate, and the inferred deep ocean potential by combining the Zanna (2019) and HadCRUT5 measurements with the surface and deep ocean heat capacities specified in Section 2a and Appendix A.

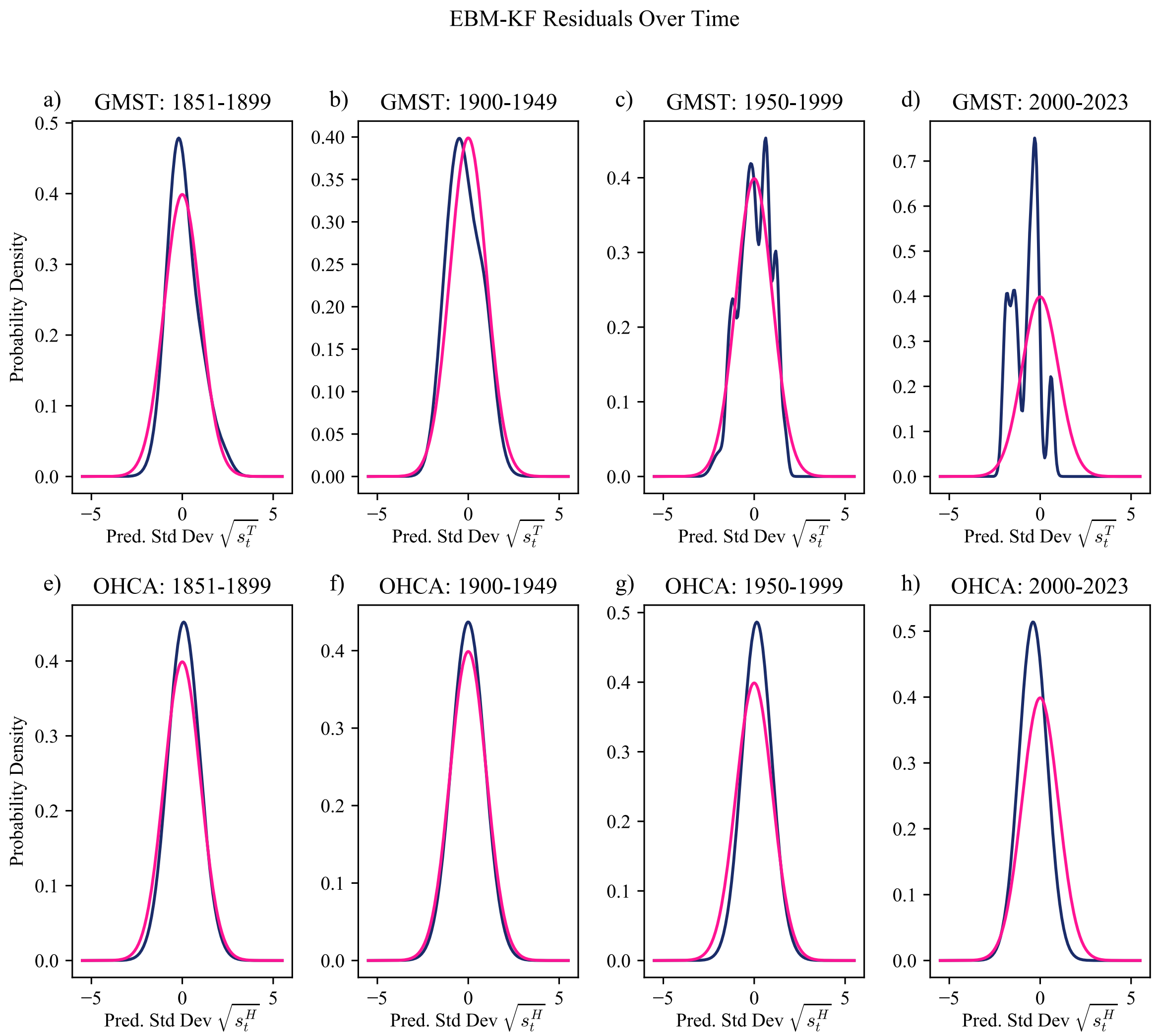


Supp. Fig. 12: Deviation between the projected climate state (pink) and empirical PDFs of the Gaussian mixture of measurements with associated uncertainty (purple), plotted relative to the ideal distribution given by the innovation covariance. Each column indicates a different time window of the EBM-KF model's run length. The top row displays the empirical PDFs of the GMST HadCRUT5 measurements relative to the model's estimate of GMST state, whereas the bottom row displays empirical PDFs of the OHCA Zanna 2019 measurements relative to the model's estimate of OHCA state. Note the initial period begins at 1851 (and the 1850 measurement is excluded from main text Fig. 3 and 4) because this has comparison involves $\mathbf{P}_{1850}$, which was intentionally over-estimated (resulting in relatively too-narrow measurement kernel). Also note that the last period is less than half the time of the others, so the GMST empirical distribution is much choppier. The observations from this most recent period 2000-2023 are also shifted slightly colder than the EBM-KF predictions, possibly indicating that some of the parameters could be better tuned than the original literature values.

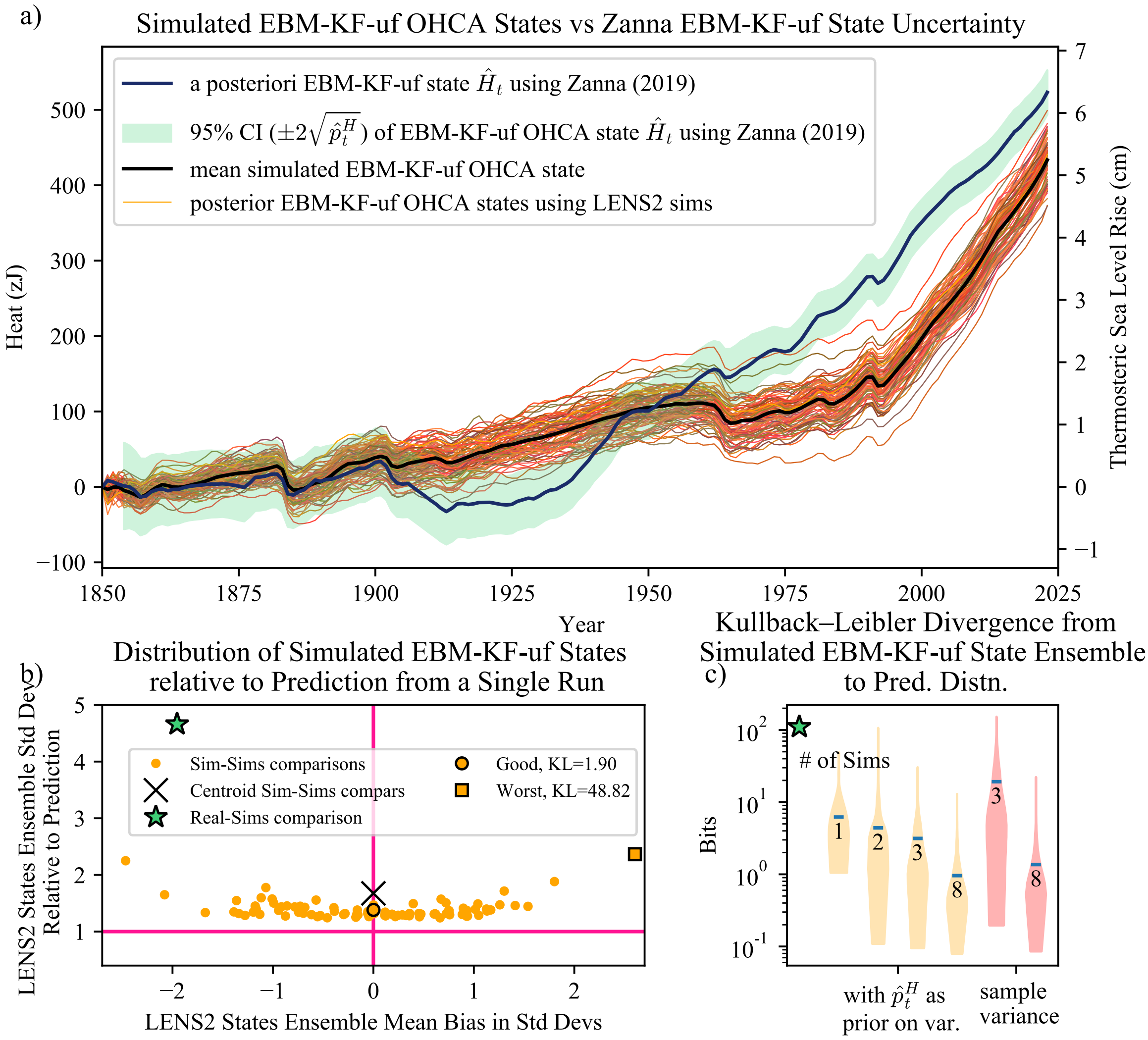


Supp. Fig. 13: As in Fig. 7, but focusing on the OHCA component rather than GMST. a) The EBM-KF posterior state estimate (thick blue) assimilating data from Zanna (2019) and its 95% confidence interval (light green), along with EBM-KF state estimates for each individual CESM2 ensemble member (orange lines) and their mean (thick black line). b) The differences between the "real" measurement based Zanna (2019) climate state and all LENS2 climate states, scaled by the state standard deviation and plotted against the ideal normal distribution. This is a particularly ill-fitting distribution because the LENS timeseries of OHCA differ substantially from the Zanna (2019) observation. The expected difference across an entire simulation run between any one $(\widehat{H}_t)_j$ and the group average $\overline{(\widehat{H}_t)}_j$ is $\pm 0.721(\sqrt{p_t^H})_j$ with range (-2.439 – 2.574), or 12.72 ZJ with range (-40.47 - 42.85)ZJ. c) As in Fig 7c, violin plots compare the Kullback-Leibler divergence (on a log scale, smaller indicates a better match) for a variety of methods of predicting the LENS2-time-Filtered ensemble spread. Taking a single EBM-KF-uf LENS2 run with $\hat{p}_t^H$ approximates the time-Filtered LENS2 ensemble with better accuracy than taking the time-varying sample variance of 3 time-Filtered ensemble members, but is less accurate than 8 time-Filtered ensemble members.

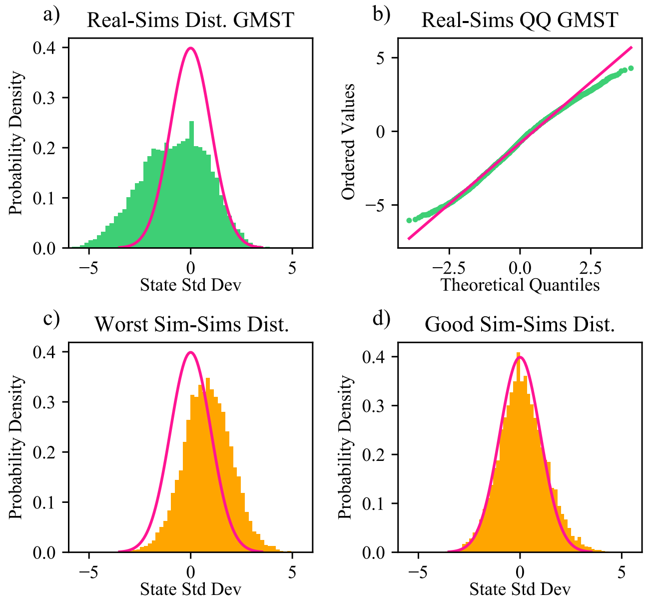


Supp. Fig. 14 (a) The differences between the "real" measurement based HadCRUT5 climate state and all LENS2 climate states, scaled by the state standard deviation and plotted against the ideal normal distribution. b) In the quantile-quantile plot, these differences between the "real" measurement based HadCRUT5 climate state and all LENS2 climate states distributions agree. c) The "worst" (by Kullback-Leibler divergence) correspondence between the predicted GMST ensemble distribution (pink) and the actual LENS2 ensemble (orange), indicated by the point outlined with a square within the Fig. 7b scatterplot. d) An example a "good" ($25^{th}$ percentile by Kullback-Leibler divergence) correspondence between the predicted ensemble distribution (pink) and the actual LENS2 ensemble (orange), indicated by the point circled in black within the Fig. 7b scatterplot.

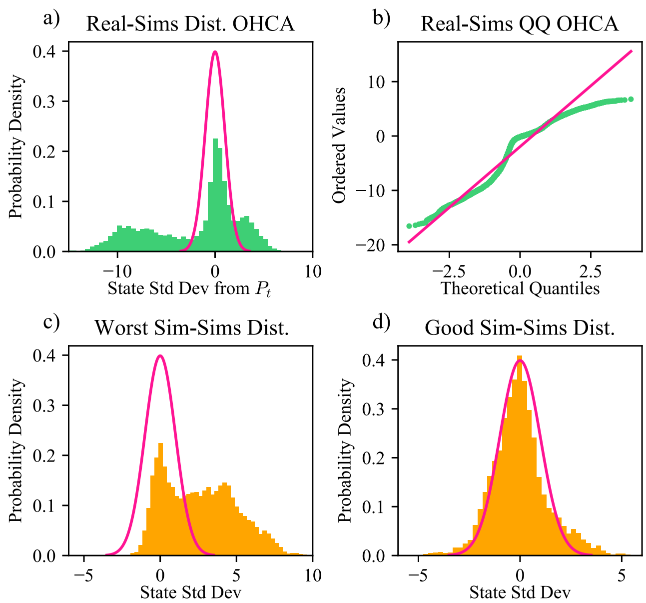


Supp. Fig. 15: As for Supp. Fig. 14, but regarding OHCA instead of GMST.

***Section D: Justification that the Extended Kalman Filter is sufficient for nonlinearity, will not diverge***

The issue of nonlinearity arises not in the computation of $\hat{\boldsymbol{x}}_{t|t-1}=\mathbf{F}(\hat{\boldsymbol{x}}_{n-1})$ but rather the covariance distribution $P_t$ of points (infinitesimal probability masses) neighboring $\hat{\boldsymbol{x}}_{t-1}$, which are assumed to scale linearly around this transformation to maintain a normal distribution. The OHCA part of the model is linear, producing 2nd-order derivatives which are 0 (SC3, SC10). Nonlinear distortion may pile more probability density onto a state other than the transformed original projection $\mathbf{F}(\hat{\boldsymbol{x}}_{t-1})$, necessitating a new computation of $\hat{\boldsymbol{x}}_{t|t-1}$ as the mean of this distorted PDF. Thus, for an arbitrary point that is $z$ standard deviations away from $\hat{\boldsymbol{x}}_{t-1}$, tracing out an ellipse that is symbolized as $\mathbf{z}\sqrt{\mathbf{P}_t}$ the remainder error $R_1$ (Lagrange mean-value form) induced in a single cycle is:

$$\mathbf{F}\left(\hat{\boldsymbol{x}}_{t-1}+\mathbf{z}\sqrt{\mathbf{P}_t};u_t\right) - \mathbf{F}\left(\hat{\boldsymbol{x}}_{t-1}\right) - \frac{\partial \mathbf{F}(x;u_t)}{\partial T}\left(\mathbf{z}\sqrt{\mathbf{P}_t}\right)|_T - \frac{\partial \mathbf{F}(x;u_t)}{\partial H}\left(\mathbf{z}\sqrt{\mathbf{P}_t}\right)|_H = R_1\left(\hat{\boldsymbol{x}}_{t-1}+\mathbf{z}\sqrt{\mathbf{P}_t}\right) \tag{SC1}$$

This is a vector equation with two components, $T_{t+1}$ and $H_{t+1}$ Splitting this remainder term into its two components, starting with $T_{t+1}$:

$$R_{1,T_{t+1}}\left(\hat{\boldsymbol{x}}_{t-1}+\mathbf{z}\sqrt{\mathbf{P}_t};u_t\right)=\frac{\partial^2 F_T(\xi_{T1},\xi_{H1};u_n)}{\partial T\,\partial T}\frac{\left(\xi_{T1}-T_{t-1}\right)^2}{2}$$
$$+\frac{\partial^2 F_T(\xi_{T1},\xi_{H1};u_n)}{\partial T\,\partial H}\left(\xi_{T1}-T_{t-1}\right)\left(\xi_{H1}-H_{t-1}\right)+\frac{\partial^2 F_T(\xi_{T1},\xi_{H1};u_n)}{\partial H\,\partial H}\frac{\left(\xi_{H1}-H_{t-1}\right)^2}{2}$$
$$\text{for } [\xi_{T1},\xi_{H1}] = \hat{\boldsymbol{x}}_{t-1}+\mathbf{z}_{\xi 1}\sqrt{\mathbf{P}_t} \quad \text{, where } 0 \le |z_{\xi 1}| \le z \tag{SC2}$$

$$\frac{\partial T_{t+1}}{\partial \boldsymbol{H}_t} = \frac{\gamma}{C_{surf}\,C_{deep}}, so\ \frac{\partial^2 F_T}{\partial T\,\partial H} = \frac{\partial^2 F_T}{\partial H\,\partial H} = 0 \tag{SC3}$$

$$\frac{\partial^2 F_T}{\partial T\,\partial T} = \frac{137.6*2\beta_2\beta_3}{AOD_t+9.73} - \frac{1.39*2.39\,\sigma_{sf}\beta_1}{C_{surf}}(T_t)^{0.39}\left(1-\beta_0\log_{10}([eCO_2]_t)\right) \tag{SC4}$$

$$R_{1,T_{t+1}}\left(\hat{\boldsymbol{x}}_{t-1}+\mathbf{z}\sqrt{\mathbf{P}_t};u_t\right) = \frac{\left(z\sqrt{\hat{p}_{t-1}^T}\right)^2}{2} * \left(\frac{0.00061}{AOD_t+9.73} - 7.26\text{ E}-5\,(T_t)^{0.39}\left(1-\beta_0\log_{10}([eCO_2]_t)\right)\right) \tag{SC5}$$

$$\left|R_{1,T_{t+1}}\left(\hat{\boldsymbol{x}}_{t-1}+\mathbf{z}\sqrt{\mathbf{P}_t};u_t\right)\right| \le \frac{z^2\hat{p}_{t-1}^T}{2}\left|6.15\text{ E}-5 - 5.685\text{ E}-4\right| \le \frac{z^2\hat{p}_{t-1}^T}{2} * 0.0005 \tag{SC6}$$

$$\hat{p}_{t-1}^T \le 0.003 \text{ after t} = 1855 \tag{SC7}$$

$$\left|R_{1,T_{t+1}}\left(\hat{\boldsymbol{x}}_{t-1}+\mathbf{z}\sqrt{\mathbf{P}_t};u_t\right)\right| \le 10^{-7}\,z^2 * 7.5 \tag{SC8}$$

This means that all probability masses that are within $|z|< 4$ standard deviations regarding the $T$ component will have a one-step error of <0.000012K. Even if the error accumulates in the same direction in each cycle of the Extended Kalman Filter, over the 174 year timeseries, the error will be within 0.002K compared to a particle method such as the Unscented Kalman Filter. (Julier and Uhlmann 1997; Wan and Van Der Merwe 2000)

Splitting this remainder term into its second component, $H_{t+1}$:

$$\mathbf{R}_{\mathbf{1},\boldsymbol{H_{t+1}}}\left(\hat{\boldsymbol{x}}_{\boldsymbol{t-1}}+\mathbf{z}\sqrt{\mathbf{P}_t};\boldsymbol{u_t}\right)=\frac{\partial^2 \boldsymbol{F_H}(\xi_{T2},\xi_{H1};u_n)}{\partial T\,\partial T}\frac{(\xi_{T1}-\boldsymbol{T_{t-1}})^2}{2}+$$

$$\frac{\partial^2 \boldsymbol{F_H}(\xi_{T1},\xi_{H1};u_n)}{\partial T\,\partial H}(\xi_{T1}-\boldsymbol{T_{t-1}})(\xi_{H1}-\boldsymbol{H_{t-1}})+\frac{\partial^2 \boldsymbol{F_H}(\xi_{T1},\xi_{H1};u_n)}{\partial H\,\partial H}\frac{(\xi_{H1}-\boldsymbol{H_{t-1}})^2}{2}$$

$$\text{for } [\xi_{T2},\xi_{H2}]=\hat{\boldsymbol{x}}_{\boldsymbol{t-1}}+\mathbf{z}_{\xi 2}\sqrt{\mathbf{P}_t}\quad\text{, where } 0\le|z_{\xi 2}|\le z \tag{SC9}$$

$$\frac{\partial H_{t+1}}{\partial \boldsymbol{H}_t}=\frac{\boldsymbol{\gamma}}{C_{deep}}*\left(\frac{C_{upper0}}{C_{surf}}-1\right)+1,\ so\ \frac{\partial^2 F_H}{\partial T\,\partial H}=\frac{\partial^2 F_H}{\partial H\,\partial H}=0 \tag{SC10}$$

$$\frac{\partial^2 F_H}{\partial T\,\partial T}=C_{upper0}*\frac{\partial T_{t+1}}{\partial T \partial T} \tag{SC11}$$

$$R_{1,H_{t+1}}\left(\hat{\boldsymbol{x}}_{\boldsymbol{t-1}}+\mathbf{z}\sqrt{\mathbf{P}_t};u_t\right)=\frac{\left(z\sqrt{\hat{p}^T_{t-1}}\right)^2}{2}*C_{upper0}*R_{1,T_{t+1}}\left(\hat{\boldsymbol{x}}_{\boldsymbol{t-1}}+\mathbf{z}\sqrt{\mathbf{P}_t};u_t\right) \tag{SC12}$$

Repeating the logic above, this means that all probability masses that are within $|z|< 4$ standard deviations will have a one-step error of <0.0016 ZJ. Even if the error accumulates in the same direction in each cycle of the Extended Kalman Filter, over the 174 year timeseries, the error will be within 0.28ZJ compared to a particle method such as the Unscented Kalman Filter. (Julier and Uhlmann 1997; Wan and Van Der Merwe 2000)

## *Section E: References*


Boltzmann, L. (1884). "Ableitung des Stefan'schen Gesetzes, betreffend die Abhängigkeit der Wärmestrahlung von der Temperatur aus der electromagnetischen Lichttheorie." Annalen der Physik **258**(6): 291-294 DOI: https://doi.org/10.1002/andp.18842580616.

Coddington, O., J. L. Lean, D. Lindholm, P. Pilewskie, M. Snow and N. C. Program (2017). NOAA Climate Data Record (CDR) of Total Solar Irradiance (TSI), NRLTSI Version 2.1. N. N. C. f. E. Information DOI: https://doi.org/10.7289/V56W985W.

Forster, P., T. Storelvmo, K. Armour, W. Collins, J. L. Dufresne, D. Frame, D. J. Lunt, T. Mauritsen, M. D. Palmer, M. Watanabe, M. Wild and H. Zhang (2021). The Earth's Energy Budget, Climate Feedbacks, and Climate Sensitivity. Climate Change 2021: The Physical Science Basis. Contribution of Working Group I to the Sixth Assessment Report of the Intergovernmental Panel on Climate Change. V. Masson-Delmotte, P. Zhai, A. Pirani et al. Cambridge, United Kingdom and New York, NY, USA, Cambridge University Press**:** 923–1054 DOI: 10.1017/9781009157896.009.

Forster, P. M., C. J. Smith, T. Walsh, W. F. Lamb, R. Lamboll, M. Hauser, A. Ribes, D. Rosen, N. Gillett, M. D. Palmer, J. Rogelj, K. von Schuckmann, S. I. Seneviratne, B. Trewin, X. Zhang, M. Allen, R. Andrew, A. Birt, A. Borger, T. Boyer, J. A. Broersma, L. Cheng, F. Dentener, P. Friedlingstein, J. M. Gutiérrez, J. Gütschow, B. Hall, M. Ishii, S. Jenkins, X. Lan, J. Y. Lee, C. Morice, C. Kadow, J. Kennedy, R. Killick, J. C. Minx, V. Naik, G. P. Peters, A. Pirani, J. Pongratz, C. F. Schleussner, S. Szopa, P. Thorne, R. Rohde, M. Rojas Corradi, D. Schumacher, R. Vose, K. Zickfeld, V. Masson-Delmotte and P. Zhai (2023). "Indicators of Global Climate Change 2022: annual update of large-scale indicators of the state of the climate system and human influence." Earth Syst. Sci. Data **15**(6): 2295-2327 DOI: 10.5194/essd-15-2295-2023.

Geoffroy, O., D. Saint-Martin, G. Bellon, A. Voldoire, D. J. L. Olivié and S. Tytéca (2013). "Transient Climate Response in a Two-Layer Energy-Balance Model. Part II: Representation of the Efficacy of Deep-Ocean Heat Uptake and Validation for CMIP5 AOGCMs." Journal of Climate **26**(6): 1859-1876 DOI: https://doi.org/10.1175/JCLI-D-12-00196.1.

Hall, G. and B. Fox-Kemper (2023). "Regional mixed layer depth as a climate diagnostic and emergent constraint." Geophysical Research Letters **[Preprint, personal communication]**.

Harshvardhan and M. D. King (1993). "Comparative Accuracy of Diffuse Radiative Properties Computed Using Selected Multiple Scattering Approximations." Journal of the Atmospheric Sciences **50**(2): 247-259 DOI: 10.1175/1520-0469(1993)050<0247:caodrp>2.0.co;2.

Julier, S. J. and J. K. Uhlmann (1997). New extension of the Kalman filter to nonlinear systems. Proc.SPIE DOI: 10.1117/12.280797.

Kravitz, B., P. J. Rasch, H. Wang, A. Robock, C. Gabriel, O. Boucher, J. N. S. Cole, J. Haywood, D. Ji, A. Jones, A. Lenton, J. C. Moore, H. Muri, U. Niemeier, S. Phipps, H. Schmidt, S. Watanabe, S. Yang and J. H. Yoon (2018). "The climate effects of increasing ocean albedo: an idealized representation of solar geoengineering." Atmos. Chem. Phys. **18**(17): 13097-13113 DOI: 10.5194/acp-18-13097-2018.

Levitus, S., J. I. Antonov, T. P. Boyer, O. K. Baranova, H. E. García, R. A. Locarnini, A. V. Mishonov, J. R. Reagan, D. Seidov, E. Yarosh and M. M. Zweng (2017). NCEI ocean heat content, temperature anomalies, salinity anomalies, thermosteric sea level anomalies, halosteric sea level anomalies, and total steric sea level anomalies from 1955 to present calculated from in situ oceanographic subsurface profile data. NOAA National Centers for Environmental Information DOI: https://doi.org/10.7289/v53f4mvp.

Livezey, R. E., K. Y. Vinnikov, M. M. Timofeyeva, R. Tinker and H. M. van den Dool (2007). "Estimation and Extrapolation of Climate Normals and Climatic Trends." Journal of Applied Meteorology and Climatology **46**(11): 1759-1776 DOI: 10.1175/2007JAMC1666.1.

Loeb, N. G., B. A. Wielicki, D. R. Doelling, G. L. Smith, D. F. Keyes, S. Kato, N. Manalo-Smith and T. Wong (2009). "Toward Optimal Closure of the Earth's Top-of-Atmosphere Radiation Budget." Journal of Climate **22**(3): 748-766 DOI: 10.1175/2008jcli2637.1.

Mann, M. E. (2008). "Smoothing of climate time series revisited." Geophysical Research Letters **35**(16) DOI: https://doi.org/10.1029/2008GL034716.

Meehl, G. A., R. Moss, K. E. Taylor, V. Eyring, R. J. Stouffer, S. Bony and B. Stevens (2014). "Climate Model Intercomparisons: Preparing for the Next Phase." Eos, Transactions American Geophysical Union **95**(9): 77-78 DOI: https://doi.org/10.1002/2014EO090001.

Meinshausen, M., Z. R. J. Nicholls, J. Lewis, M. J. Gidden, E. Vogel, M. Freund, U. Beyerle, C. Gessner, A. Nauels, N. Bauer, J. G. Canadell, J. S. Daniel, A. John, P. B. Krummel, G. Luderer, N. Meinshausen, S. A. Montzka, P. J. Rayner, S. Reimann, S. J. Smith, M. van den Berg, G. J. M. Velders, M. K. Vollmer and R. H. J. Wang (2020). "The shared socio-economic pathway (SSP) greenhouse gas concentrations and their extensions to 2500." Geosci. Model Dev. **13**(8): 3571-3605 DOI: 10.5194/gmd-13-3571-2020.

Morice, C. P., J. J. Kennedy, N. A. Rayner, J. P. Winn, E. Hogan, R. E. Killick, R. J. H. Dunn, T. J. Osborn, P. D. Jones and I. R. Simpson (2021). "An Updated Assessment of Near-Surface Temperature Change From 1850: The HadCRUT5 Data Set." Journal of Geophysical Research: Atmospheres **126**(3): e2019JD032361 DOI: https://doi.org/10.1029/2019JD032361.

Nasa/Larc/Sd/Asdc (2018). Global Space-based Stratospheric Aerosol Climatology Version 2.0.

Rodgers, K. B., S. S. Lee, N. Rosenbloom, A. Timmermann, G. Danabasoglu, C. Deser, J. Edwards, J. E. Kim, I. R. Simpson, K. Stein, M. F. Stuecker, R. Yamaguchi, T. Bódai, E. S. Chung, L. Huang, W. M. Kim, J. F. Lamarque, D. L. Lombardozzi, W. R. Wieder and S. G. Yeager (2021). "Ubiquity of human-induced changes in climate variability." Earth Syst. Dynam. **12**(4): 1393-1411 DOI: 10.5194/esd-12-1393-2021.

Ruggieri, E. and M. Antonellis (2016). "An exact approach to Bayesian sequential change point detection." Computational Statistics & Data Analysis **97**: 71-86 DOI: https://doi.org/10.1016/j.csda.2015.11.010.

Sato, M., J. E. Hansen, M. P. McCormick and J. B. Pollack (1993). "Stratospheric aerosol optical depths, 1850-1990." J. Geophys. Res. **98**: 22987-22994 DOI: 10.1029/93JD02553.

Schwartz, S. E., n. Harshvardhan and C. M. Benkovitz (2002). "Influence of anthropogenic aerosol on cloud optical depth and albedo shown by satellite measurements and chemical transport modeling." Proceedings of the National Academy of Sciences **99**(4): 1784-1789 DOI: 10.1073/pnas.261712099.

Vernier, J., L. Thomason, J. P. Pommereau, A. Bourassa, J. Pelon, A. Garnier, A. Hauchecorne, L. Blanot, C. Trepte, D. Degenstein and F. Vargas (2011). "Major influence of tropical volcanic eruptions on the stratospheric aerosol layer during the last decade." GEOPHYSICAL RESEARCH LETTERS **38** DOI: 10.1029/2011GL047563.

Wan, E. A. and R. Van Der Merwe (2000). The unscented Kalman filter for nonlinear estimation, Institute of Electrical and Electronics Engineers Inc. DOI: 10.1109/ASSPCC.2000.882463.

Wielicki, B. A., B. R. Barkstrom, E. F. Harrison, R. B. Lee, G. Louis Smith and J. E. Cooper (1996). "Clouds and the Earth's Radiant Energy System (CERES): An Earth Observing System Experiment." Bulletin of the American Meteorological Society **77**(5): 853-868 DOI: 10.1175/1520-0477(1996)077<0853:catere>2.0.co;2.

Wild, M., D. Folini, M. Z. Hakuba, C. Schär, S. I. Seneviratne, S. Kato, D. Rutan, C. Ammann, E. F. Wood and G. König-Langlo (2015). "The energy balance over land and oceans: an assessment based on direct observations and CMIP5 climate models." Climate Dynamics **44**(11): 3393-3429 DOI: 10.1007/s00382-014-2430-z.

Wild, M., M. Z. Hakuba, D. Folini, P. Dörig-Ott, C. Schär, S. Kato and C. N. Long (2019). "The cloud-free global energy balance and inferred cloud radiative effects: an assessment based on direct observations and climate models." Climate Dynamics **52**(7): 4787-4812 DOI: 10.1007/s00382-018-4413-y.

Zanna, L., S. Khatiwala, J. M. Gregory, J. Ison and P. Heimbach (2019). "Global reconstruction of historical ocean heat storage and transport." Proceedings of the National Academy of Sciences **116**(4): 1126-1131 DOI: 10.1073/pnas.1808838115.

Zhong, W. and J. Haigh (2013). "The greenhouse effect and carbon dioxide." Weather **68**: 100-105 DOI: 10.1002/wea.2072.